UNIVERSITÀ DEGLI STUDI DI PADOVA
SCUOLA DI SCIENZE

Dipartimento di Geoscienze
Direttore Prof. Cristina Stefani
TESI DI LAUREA MAGISTRALE
IN
GEOLOGIA E GEOLOGIA TECNICA

Deformation Partitioning and Fluid-Rock Interaction in the Southwestern Tauern Window

Relatore: Prof. Giorgio Pennacchioni
Correlatori: Prof. Claudio Mazzoli
Dr.ssa AnnaMaria Fioretti

Laureando: Alberto Ceccato

ANNO ACCADEMICO 2013/ 2014

Abstract

The study of my master thesis had manifold goals with the aim of learning different research approaches, techniques and expertises at this stage of my career. The studied area is the southwestern portion of the Tauern Window of the Eastern Alps exposing the metagranitoids and the derived mylonites forming the core of the Penninic basement nappe exposed beneath the Austroalpine unit. The study of the area has addressed different topics ranging from the regional tectonics of this part of the Eastern Alps to more process-oriented issues such as the nucleation of ductile shear zones and the processes of fluid-rock interaction during deformation. The thesis has involved 2 campaigns of field work addressed to the structural analysis in several selected areas and the characterization of samples in the lab by different methods.

The Tauern Window is a major tectonic feature of Eastern Alps where the Alpine Pennidic tectonic unit (nappe) is exposed beneath the Austroalpine nappe. The sequence of Alpine deformation events should be recorded in the field by a series of overprinting fabrics including mylonites and faults with a different kinematics: (i) thrusting associated with the stage of nappe stacking; (ii) strike-slip associated with the component of lateral escape, and (iii) normal "faulting" associated with the unroofing of the exhuming nappe pile and with the activity of the Brenner Fault system (*Goldny et al.*, 2008). The structural field work was mainly addressed to identify and map the structures associated with the different tectonic components described above in the southwestern border of the Tauern Window.

The structural study followed the reference scheme given by previous works of *Mancktelow and Pennacchioni* (2005) and *Pennacchioni and Mancktelow* (2007) for the Neves area was extended during my master thesis (i) N-S to cover a complete traverse across the tectonic unit (from the Neves area to the Zillertal Valley) and (ii) E-W over a distance of ca. 8 km (from the Moosboden glacial cirque to the Hochfeiler area). The structural sequence includes a phase of ductile deformation, syn-kinematic to amphibolite facies conditions, and a later overprint

by cataclastic faults. The ductile deformation is heterogeneously distributed and this partitioning is scale-independent. Within the low strain domain the ductile deformation is localized at the outcrop scale to a network of discrete (of as much as a few meters thick) shear zones. This structural evolution indicates a NNW-SSE to almost N-S shortening during the Alpine deformation from the syn-metamorphic (amphibolite facies: 550–600°C, 0.4-0.7 GPa) mylonites to the brittle faulting during exhumation, respectively. Both the mylonites and the faults of the Neves area have a strike-slip kinematics. Both the ductile and the brittle deformation occurred under hydrous conditions as witnessed by the common occurrence of veins associated with deformation structures. An episode of fluid-rock interaction postdated the main phase of faulting and is associated with the local development of episyenites.

Structures linked to thrust and exhumation tectonics are missing from our are. Thrust structures are likely to have been overprinted by the following strike-slip lateral escape tectonics. Exhumation structures instead seems to be confined to a narrow deformation zone along the Brenner Line.

The western zone have a homogeneous distribution of the strain, and the comparison between homogeneous deformation structures and partitioned structures has allowed us to define the zone as a purely constrictional transpression zone (*Fossen & Tikoff,* 1998). However, the partitioning in strain intensity over the region is not associated with a partitioning of components of thrusting, lateral escape and detachment in no stage of deformation, as is instead observed in other geological contexts (*Fossen et al.*, 1994).

The study area provides an ideal natural laboratory for the study of the process of ductile shear zone nucleation. It provides spectacular glacier-polished outcrops within metagranitoids that preserve all stages of incremental development of structures in a relatively simple and “isotropic” material. The field observations indicates:

In contrast with numerical and rock-analogue models (e.g. *Mancktelow*, 2002; *Mancktelow and Pennacchioni*, 2014) shear zone nucleation never occurred

within homogeneous metagranodiorites

Almost any structural or compositional (rheological) surface heterogeneity (e.g. fractures, dykes, veins and lithological contacts) was capable of been exploited by localized shear deformation.

The type of exploited precursor determined the type of shear zone and geometrical characters: (i) weak precursors compared to the host metagranodiorites ("unfilled" fractures; quartz veins; biotite-rich basic dykes) localized strain: shear zones have commonly a rather homogeneous strain distribution and a sharp boundary to almost undeformed host rock; (ii) strong layers (aplite dykes; alteration haloes surrounding veins) localized the deformation at their boundaries forming paired shear zoned at their selvages mainly developed within the metagranodiorite.

Reactivation of original ductile shear zones can explain the controversial sense of shear of some paired shear zones exploiting the alteration halos surrounding epidote-filled veins. This contrasting sense of shears is interpreted as due to Alpine reactivation of original ductile shear zones developed in the pre-Alpine granitoid protolith as result of the original evolution during pluton cooling similar to what is described for some intrusions elsewhere (e.g. *Pennacchioni*, 2005; *Pennacchioni and Zucchi*, 2013).

The latest episode of fluid-rock interaction, which has not been previously described, is responsible for the formation of local episyenites which postdated the main episode of brittle faulting. Episyenites are quartz-depleted, alkali-metasomatized granitoids (*Cathelineau*, 1986), strictly connected to either brittle or ductile shear zones (*Rossi et al.* 2005), and characterized by a conspiquous porosity. The field study has indicated that episyenites are associated to cataclastic faults but do not pervasively exploited the fault structure; fluid flow and alteration were not influenced by compositional and/or textural anisotropies of the host rock; no clear relation between fault slip and episyenite volume was observed.

The composition of the host rock influence the spatial development, indeed quartz-poor lithologies commonly limit the diffusion of the fluid and of the alteration; in a similar way ductile textures of the host rock may limit or restrain the fluid diffusion. Mass-balance calculation from XRF bulk chemistry, aided with μ-CT volume evaluation, suggest that episyenites are due to a Na-metasomatism of parent rock and that have a particular paragnesis including: Plagioclase (Plg2:Ab_{99} that overgrows Plg1:Ab_{85}) + Vermicular Chlorite + Adularia + Calcite ± Anatase ± Hematite ± Apatite. Albitization and dequarzification are the two main mineralogical changes (Feldspar increase of ca 35 wt%, Quartz decrease by a 25%).

SEM BSE and μ-CT images shows that porosity develops also at the grain scale as the result of Albitization process of the parent Plagioclase (Oligoclase), but most of the macro-porosity is due to Quartz dissolution. Stable Isotope ($\delta^{18}O$ and $\delta^{13}C$) analysis on calcite precipitated in episyenite indicate a possible contribution of a meteoric fluid to the episyenitization process.

Index

Introduction – Aims of this work

The study of my master thesis had manifold goals with the aim of learning different research approaches, techniques and expertises at this stage of my career. The thesis has led me up to deals with different topics ranging from the regional tectonics to more process-oriented issues such as the nucleation of ductile shear zones and the processes of fluid-rock interaction during deformation. The thesis has involved 2 campaigns of field work addressed to the structural analysis of several selected areas and the characterization of samples in the lab by different methods which have included: (i) optical microscopy; (ii) SEM backscattered imaging; (iii) geochemical XRF analysis; (iv) mineralogical characterization by Raman microspectroscopy; (v) EMP analysis; (vi) XRPD analysis with Rietveld Refinement; (vii) micro Computized Tomography (μ-CT) analysis; (viii) Zircon U-Th/He thermocronometry; (ix) Stable Isotopes analysis; (x) Fluid inclusions microthermometry on Quartz. Data acquisition and interpretation for many of these techniques has been carried out with the valuable support and guidance of a few experienced researchers. Doing so, I have learned to work in a multidisciplinary group of research. Two main issues have been addressed during this master thesis:

– Relationship between the deformation structures mapped in the study area of the southwestern Tauern Window and the large scale tectonics of the Eastern Alps, with particular attention to processes of deformation partitioning and shear zone nucleation;

– Fluid-rock interaction and the role of pre-existing structures on fluid flow and formation of episyenites.

Deformation and strain partitioning

Deformation is the change in position, shape and size of a body under applied

stresses. Rheology instead look at the way in which this body flow, deform according to the environmental physical and chemical conditions. From the mathematical point of view, deformation can be described as a linear transformation of a vector of initial defined length, direction and versus, as it could be a vector **a** between two material point of a body. The final vector **b** is given by a linear transformation of **a** dictated by the deformation component (*Kennet et al., 2008*):

$$b = a + a \cdot \nabla u$$

where **u** is the displacement vector, that is the vector defined by the initial and final position of a material point of the former vector **a**. As we can see, the linear transformation is given by an identity part (**b**=**a**) that correspond to a translation of the initial vector into another position, and by a function of the **Displacement Gradient**. In a three-dimensional space it is given by a jacobian matrix, i.e. a second-rank tensor:

$$\nabla u = \frac{\partial u}{\partial x} + \frac{\partial u}{\partial y} + \frac{\partial u}{\partial z}$$

This term represent the deformation *sensu strictio*, i. e. Strain and Rotation components of the total deformation. In fact the deformation gradient matrix could be decomposed into a symmetric and antisymmetric part, respectively *Strain* ε and *Rotation* ω. In vectorial form they are written as follow:

$$\varepsilon_{ij} = \left(\frac{\partial u_{ij}}{\partial j} + \frac{\partial u_{ij}}{\partial i} \right) \quad \omega_{ij} = \left(\frac{\partial u_{ij}}{\partial j} - \frac{\partial u_{ij}}{\partial i} \right)$$

$$\nabla u = \varepsilon_{ij} + \omega_{ij}$$

In rheology, structural geology we often refers to *Strain rate ε'* and *Vorticity* ω' as the time derivative of the above-mentioned deformation component. Strain rate and Vorticity are then the symmetric and antisymmetric components in which the **Velocity gradient tensor**

$$\nabla v = \nabla \frac{D\vec{u}}{Dt}$$

This relation imply that deformation takes place when there is a velocity gradient between adjacent part of the body. This definition comes from continuum mechanics in which the deformation of a body is seen as a *flow.*

Spin is another quantity that is usually found in structural geology measuring the amount of rotation. The difference between *Spin* and *Vorticity* of the deformation is the reference system: Spin is the average angular velocity of the flow passing through a fixed point; Vorticity instead measures the amount of rotation in respect to an external reference system. From the mathematical point of view Vorticity is a vector given by the three independent component of the Spin tensor (*Twiss and Moore, 2007*).

Strain is *homogeneous* when the changes in shape and size for each small part of the body are geometrically similar to those for the whole body (*Twiss and Moore, 2007*). Heterogeneous strain might be always reduced to a set of small homogeneously strained domains. *Pure* and *simple shear* strains usually cooperate in the formation of homogeneous strain geometries. *Pure* strain is a general class of deformation at which belong several particular deformation geometries, such as *pure* shear, contraction, dilation and flattening (usually what we can found in a Flinn's diagram in Fig. I). Characteristic of this class is that the principal strain axis orientation is constant in respect to the external reference frame during the flow. This means that any rotation component is involved, or at least the net rotation is null. Instead, in *simple shear* geometries, the vorticity component is near to its maximum value: the normalized value of vorticity in respect to the strain rate, named kinematic vorticity number W_k after *Passchier & Trouw, 2007*, is near 1. Because of their rotation during progressive deformation, the instantaneous strain axis are not parallel to the finite strain axis. Therefore, *pure* strains are termed also *coaxial/irrotational strain*, instead *simple shear* strains are *non-coaxial/rotational*.

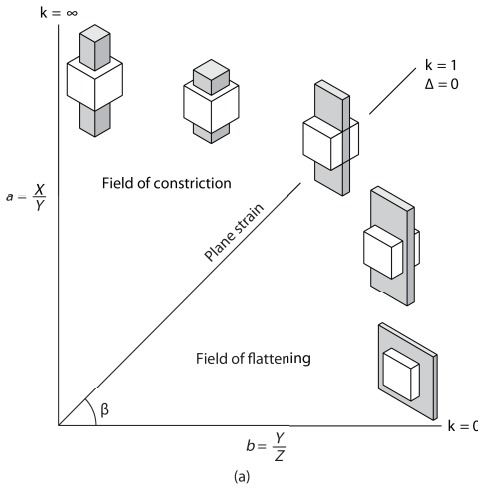

Fig. I: Flinn diagram (from Twiss and Moore, 2007)

In a deforming continuum, the velocity field around any material point can be partitioned into its fundamental components, that are translation, rotation and strain. What we can most appreciate in the analysis of geological structures and deformation geometries in general is the partitioning of Spin and Vorticity components (*Lister et al., 1983*). Therefore, the most straightforward result in strain analysis is the distinction between pure and simple shear strain geometries. Deformation partitioning results especially from the existence of *material anisotropies* and of *boundary constrains* on the flow (*Lister et al. 1983*). *Simple shear*, *non-coaxial* flows are preferentially partitioned onto the boundary between striff and weak materials. Competent layers in a simple-shear flow usually maximizes the Spin component at the expense of the total vorticity in order to minimize the degree of non-coaxiality. The degree of coupling between flowing body and the enveloping material will define the coaxiality of the flow. Coaxial flows take place where there are no or weakly constrained boundaries. These different behaviours between simple and pure shear might be due to different mechanical response of the rock to the deformation: simple shear may lead to a strain softening evolution, whereas pure shear may lead to strain hardening (*Solar et al.,* 2001).

Localization and shear zone nucleation in homogeneous continua.

A striking feature resulting from strain partitioning are *shear zones*, i.e. tabular volumes of rock which are relatively more deformed than the bounding host rock. Shear zones may develop also from either/both isochoric deformation or heterogeneous non-constant-volume deformation (*Ramsay, 1980*).

With regards to shear zone nucleation and development in granitoid rocks I have considered the works of *Mancktelow & Pennacchioni, (2005)* and *Pennacchioni & Mancktelow (2007)* as a reference frame and starting point to develop my Master thesis. These works focused on the analysis of the shear zone network developed during Amphibolite facies deformation in the Zentralgreise unit of the Neves Area (SW Tauern Window), just in the middle of the surveyed region by myself.The fundamental conclusions of these two papers are:

i. Strain localization and shear zone nucleation under high grade metamorphic conditions are controlled by the pre-existing magmatic structures of the granitoid, which include both structural and compositional heterogeneities, and by newly formed fractures and veins cyclically developed during the dominant ductile deformation ;

ii. Brittle and brittle-ductile shear zones developed from effectively intact rock in the metagranitoids;

iii. The viscosity contrast between lithologies controls the type and geometry of the shear zone: (a) strong layers concentrated strain at their boundaries developing heterogeneous shear zones; and (b)weak layers localized a rather homogeneous deformation

iv. Conjugate and differently oriented ductile shear zones can have been active at the same time; the bulk strain compatibility is maintained by development of foliated domains in the host rock especially at contractional domains or by fracturing filled with veins;

v. Increasing deformation is accommodated by broadening of shear zones,

i.e. strain spreaded rather than localize with progressive deformation

Strain compatibility problems in conjugate brittle and brittle-ductile shear zones are often accommodated by the sequential slip on the different structures (*Ramsay, 1980*). Furthermore, progressive deformation in a brittle environment is usually accommodated by subsequent localization on single surfaces, even though cataclasis involve a bigger volume of rock. From these simple observations we can understand the important role of rheology and physical conditions of deformation in controlling strain partitioning.

According to the theoretical principles at the base of this process, flow partitioning should be scale-invariant, as we can see in numerical and analogue models (*Bell*, 1989; *Mancktelow,* 2002*)*. However, field observations have demonstrated that this is not always true (*Mancktelow,* 2013).

Deformation partitioning in Transpressive Orogens

Relative motion between tectonic plates may be oblique(traspressive margins) implying that the slip vector includes one component parallel to the plate margin and one component perpendicular to the plate boundary. As a consequence, at these margins the contractional tectonics is accompanied by strike-slip tectonics (*Dewey et al.,* 1998). which can be partitioned in space and time. According to *Fossen & Tikoff* (1998), transpressive zones are "*steep strike-slip influenced deformation zones that deviate from simple shear by a component of shortening […] across the zone*". In transpressive zones deformation can be homogeneously distributed across the zone, or partitioned into a homogeneous simple shear and homogeneous pure shear components (*Jones & Tanner*, 1995). This partitioning was mathematically modelled by *Sanders & Marchini* (1984) for the first time. Different authors have later modified this original model by the changing boundary conditions in order to adapt the model to more realistic geologic conditions (*Fossen et al.,* 1994; *Jones & Tanner*, 1995). The strain architecture where two simple shear domains bound a pure shear domain can be described

mathematically by the tensor (Fig. II):

$$D=\begin{pmatrix}1&\gamma&0\\0&1&0\\0&0&1\end{pmatrix}\cdot\begin{pmatrix}1&0&0\\0&\alpha^{-1}&0\\0&0&\alpha\end{pmatrix}=\begin{pmatrix}1&\alpha^{-1}\cdot\gamma&0\\0&\alpha^{-1}&0\\0&0&\alpha\end{pmatrix}$$

where: D is the deformation matrix, α^{-1} is the ratio between the deformed and the original width of the deformation zone, and γ is the bulk shear strain parallel to the zone (*Jones & Tanner*, 1995; from *Sanders & Marchini,* 1984). Transpressive strain partitioning is more effective in presence of preexisting anisotropies and zones of weakness where simple shear preferentially localize (*Jones & Tanner*, 1995). Domains of homogeneous pure shear could be affected by homogeneous thickening or widening (depending on the boundary conditions).

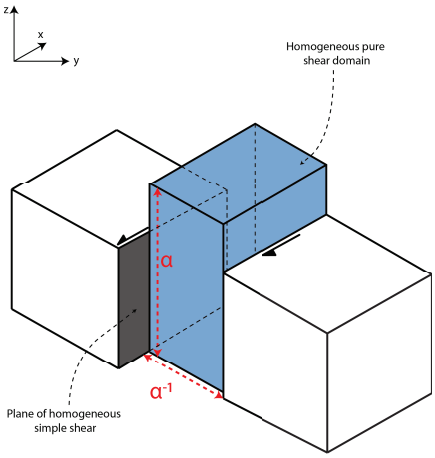

Figure II: Block diagram showing a transpression zone with a thickening central domains characterized by pure shear, bounded by two simple shear zones. (From Jones & Tanner, 1995)

Transpressive strain partitioning is recorded by the occurrence of separated purely strike-slip tectonics domains and thrust-slip zones, as it has been observed in subduction-arc settings (*Fitch,* 1972; *McCaffrey,* 1996, 2000) and oblique continental collision zones (San Andreas fault, *Teyssier et al.,* 1998; Northern Appalacchian, *Solar et al.,* 2001; Norwegian caledonidies, *Northtrup et al.*, 1996). Homogeneous pure shear domains is recorded by the occurrence of thrust faults and folds with axis perpendicular to the maximum shortening direction. Simple shear domains correspond to the strike-slip lineaments.

Fluid-rock interaction and episyenites

The occurrence of syntectonic veins, alteration halos around shear zones and cataclasites highlight the continuous interplay between fluid and deformation during the whole tectonic history of the study area. The process of fluid-rock interaction can result in a dramatic modification of mechanical and rheological properties, such as permeability and porosity and is therefore of paramount importance in understanding the deformation behaviour of the rocks as well as the fluids transport across the rock volume. Metamorphic mineral reactions could enhance, trigger or damp down deformation or control the evolution of strain partitioning (*Steffen et al*, 2001) and strain geometries (*Mancktelow & Pennacchioni,* 2005).

Therefore, fluid-rock interaction can actively influence the development of deformation geometries (such as in hydrofracturing and in the formation of rheologically stronger alteration halos) or it could be simply an effect of the pre-existence of deformation structure. In this case, faults, joints and veins act as flow-channels along which fluid-rock interaction occurs triggered by the activity of the structure itself (*Sibson,* 1994). In many ore-forming processes, fluids act as passive elements being transported, modified in composition and physical properties according to the activity of brittle and ductile structures through the establishment of pressure and/or temperature gradient, sudden variations in environmental condition that can trigger fluid saturation and mineral deposition. Fluids are governed and transported passively by deformation mainly in the hydrothermal environment. In this environment many economic ores found their location and genesis (e.g. Cu-Sn-W-Au porphyry deposits and low-sulphidation gold deposits). Being of economic importance, this type of ore deposits have been studied and characterized very well during many years of focused research. However, ore-deposits of minor importance and barren ones form the majority of the mineralization in the hydrothermal environment. Among the others, episyenites are little-known ore-deposits that are gaining more and more importance for different field of the ore geology and environmental engineering.

Episyenites are quartz-depleted, alkali-metasomatized granitoids (*Cathelineau, 1986*), associated with to either brittle or ductile shear zones (*Rossi et al. 2005*), and characterized by a pervasive porosity. The occurrence of episyenites has been reported in several works from different parts of the world: e.g., in european Variscan granitoids (*Cathelineau, 1986; Rossi et al. 2005; Recio et al. 1997)*, Fennoscandian shield (*Petersson et al. 2012*) and Amazonian Craton (*Borges et al. 2009; Costi et al. 2002*). In the Eastern Alps a episyenite has been reported within the Tauern Window in association with mineralized veins (*Melcher et al., 1996*). Most of the research on episyenite addressed their geochemistry and the process of fluid-rock interaction in order to understand the relationship between episyenites and the related economic mineralizations (U: *Leroy, 1984*; Au: *Lopéz-Moro et al., 2013;* Sn: *Costi et al. 2002*). A unique model for episyenite formation

is still not defined, given the slightly different hydrothermal conditions, fluid provenance and compositions that are reported in literature. However, in general quartz leaching and alkali-metasomatism is caused by low salinity fluids interacting with granitoid at shallow crustal levels in the temperature range between 450°C and 150°C. The importance of episyentites, as porous rocks within granitoids, is also related to the potential use of f granitoid plutons as sites for nuclear waste repository (*Petersson et al. 2012*; *Nishimoto et al., 2014*).

In almost all of the published papers on episyenites, the field description is missing or scarce, mainlydue to the poor exposure of these highly porous rocks as a consequence of weathering. Many published work on was conducted on drill core samples and therefore the study yield limited information on the geometry of the episyentite alteration. The few exceptions are the works of *Rossi et al. (2005)* on mylonite-related episyenite in the Mont Blanc Massif and *Gonzales-Casado et al. (1996)* on the episyenitic alteration of the Sierra del Guadarrama granitoids. The "Moosboden Episyenites" (the episyenites studied in the current thesis) offer a unique opportunity to carefully map a relatively large episyenite outcrop due to the exposure on a recently de-glaciated area. This can yield information on the relationships between the extent and localization of mineralization associated with episyenite and the geometry of the overprinted/exploited pre-existing structure. This understanding has implication in any attempt at predicting the extent and localization of mineralizations in any other poorly exposed context.

–

This thesis is subdivided into the following sections: **Geological Settings** deals with the general geologic features of the Southwestern Tauern Window; **Chapter 1** describes the results of the structural fieldwork that are later analysed at the light of deformation partitioning process at different scale, interpreted and discussed following the existent theories on orogenic processes; **Chapter 2** reports the field and lab data on Episyenite, aimed at the understanding the structural constraints on fluid flow in granitoid rocks; in **Chapter 3** is reported the result of microthermometry on fluid inclusion in quartz from a dilatant vein linked to a

fault; **Chapter 4** describe the results of U-Th/He thermochronometric analysis on Zircons from episyenites.

In **Appendix A** are recluded the tables with compositional data of episyenites. **Appendix B** describes the analytical techniques used in the study.

Geological settings

The work edited in this master thesis has been developed on selected outcrops of the Zillertal Alps, a subsection of the Central Eastern Alps (Western Tauern Alps). This region is located along the border between Italy and Austria (South Tyrol), spreading from Weißenbach (Riobianco – Luttago, It), westward to St. Jakob in Pfitsch (San Giacomo in Val di Vizze, It) and northward to Ginzling (Aus). Most of the studied localities are situated above 2500 m a.s.l., at the base of retreating glacial tongues. The negative trend of glacial growth of the last few decades has bring to the sunlight a huge quantity of perfectly polished outcrops with exceptional exposure. This is the main reason for which we have chosen to study the selected outcrops.

– Eastern Alps –

Eastern Alps differs from the rest of the orogen, being the result of two independent collisional events both of Alpine age (*Neubauer et al.*, 2000), as consequence of the different paleogeography between eastern and western Europe-Adria collision zone (Fig. 3). The tectonic evolution of the Eastern Alps started in Early Permian with a rifting event between Laurussia and Gondwana, promoting subsidence of the future Southalpine basement and the following westward transgression of the Paleotethys ocean. In the Middle Triassic subsidence started also in the future Austroalpine terranes, that at this time are completely separated from the Southalpine basement by the Hallstatt-Meliata ocean, a small oceanic branch of the Paleotethys. This short-lived basin started to close in the Jurassic and ended-up during the opening of Pennidic (Piedmont-Liguria) Ocean and the Valais trough. This subduction event of Cretaceous times (95-90 Ma; *Neubauer et al.*, 1999) led to the formation of the Austroalpine *s.l.* nappe pile. From the Late Cretaceous to the Early Eocene takes place the closure of the Piedmont-Liguria ocean between the Austroalpine nappe stack and the outermost european margin (Helvetic-Briançonnais terranes; *Schmid et al.*, 2013).

In the Early Eocene, the complete closure of the Piedmont Ocean led to the subduction of the distal european continental crust (Pennidic units) and to high pressure metamorphism of the downgoing oceanic slab. During this first phase of accretion, exhumation of high pressure units started as a consequence of indentation of the Adriatic plate into the Austroalpine-Pennidic nappe pile (*Neubauer et al.*, 1999; *Schmid et al.*, 2013). Soon after continental collision occurred, the entire nappe pile has been interested by a Barrovian regional metamorphism, and by diffuse plutonis (Oligocenic magmatism, 32-28 Ma; *Rosenberg*, 2004). The processes at the base of this thermal event are still under debate (*Blackenburg et al.*, 1995). From the Oligocene – Early Miocene onward, Eastern Alps have been subdivided into three different domains: the region of (i) retro- and (ii) pro-wedge characterized by frontal thrusting and propagation of deformation perpendicular to the orogen strike; (iii) the inner zone, the core of the Eastern Alps characterized by orogen-parallel lateral escape and exhumation tectonics.

The current regional tectonic framework of the Eastern Alps is defined by a set of strike-slip lineaments, of which the most important is the Periadriatic Fault, that also demarcates the general boundary between Alps *s.s.* affected by the Cenozoic metamorphism and the Southern Alps (*Dal Piaz et al.,* 2001). Westward the Periadriatic lineament is defined by the NW-SE Giudicarie transpressive sinistral faults system and eastward by the WNW-ESE Pustertal-Gailtal dextral fault. Just north of the junction point between these two systems, from the Oligocene onward a wide region of marked exhumation and surface uplift has come to establish: the Tauern Window.

Tauern is one of the three major tectonic window of the Eastern Alps (the other two are Engadine and Reichnitz windows in Switzerland and Austria) inside which the Pennidic nappe pile are exposed beneath the Austroalpine terranes. It has formed from the Oligocene onward during the exhumation and lateral extrusion of the Alpine nappe pile (*Lammerer et al.,* 1998) as a consequence of continental collision and indentation of the Adriatic plate. These two orogenic

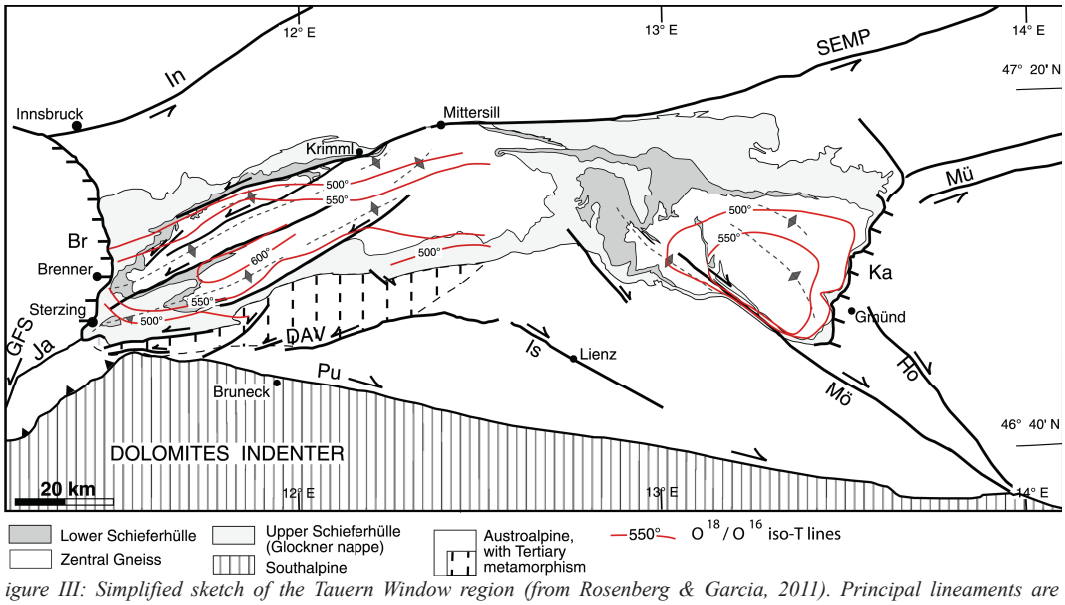

igure III: Simplified sketch of the Tauern Window region (from Rosenberg & Garcia, 2011). Principal lineaments are depicted as follow:Br: Brenner; Ka: Katschberg; Pu:Pustertal; SEMP: Salzach-Ennstal-Mariazell-Puchberg; DAV: Defereggen-Antholz-Valls; Mölltal; GFS: Giudicarie Fault System; Ja: Jaufen; In:Inntal

processes resulted form the simultaneous activity of a set of strike-slip and low angle normal faults bounding the Tauenr Window (*Goldny et al.*, 2008; Figure 3). Brenner and Katschberg normal faults define respectively the western and eastern border of the window: their activity accommodated the effective lateral spreading and suèerficial escape tectonics that developed due to N-S convergence (*Fügenschuh et al*. 1998; *Kurz et al.,* 1993). In the western Taeurn Window the Brenner fault is supposed to have accomplished for a vertical displacement of 15-25 km (*Axen et al.*, 1995) with a horizontal throw in the order of tens of kilometers (10 to 70 km, *Rosenberg & Garcia*, 2011).

At the southern and northern side two strike-slip lineaments border the Tauern Window: the Salzach-Ennstal-Mariazell-Puchberg and the Mölltal faults (*Rosenberg et al.* 2008; *Goldny et al.* 2008). The estimated displacement along the sinistral SEMP line is 60-70 km (*Rosenberg et al.*, 2008).

Another two important regional lineaments south of the Tauern Window are the Defereggen-Antholz-Valls line ant the already mentioned Periadriatic system. The DAV line is a wide zone of diffuse heterogeneous deformation (*Mancktelow et al*, 2001) that defines the effective southern border of the Alpine metamorphism in the Austroalpine nappe and, at the same time, the southern limit of the region of

Oligocenic rapid exhumation around the current Tauern Window (*Steenken et al.,* 2002). Its activity were important before the indentation of the Adria plate: the regional sinistral kinematic was dominated and defined by this lineament. After the indentation, the main role has been played by the dextral Periadriatic lineament (*Mancktelow et al.* 2001).

The SEMP line has also an important role in defining the internal setting of the western Tauern Window. In fact, inside the window are exposed in several ductile faults represent, according to *Rosenberg et al.* (2008), the roots of the brittle lineament that extend from Mittersill to the Styrian basin. Ahörn, Olperer, Greiner and Ahrntal shear zones are four main sinistral lineaments arranged in an en-echelon pattern that resemble a horse-tail splay of the SEMP fault. Actually, all these shear zones were active simultaneously till the uppermost Miocene (*Rosenberg et al.,* 2008; 13-7 Ma according to *Schneider et al.,*2013).
Internal shear zones are placed along major synforms of the folded Pennidic nappe pile (*Goldny et al.,* 2008). During the convergence and orogen-perpendicular shortening, the former duplex structure were folded in a series of large-scale upright antiforms separeted by very narrow synforms (*Vesela et al.* 2008). The contemporaneous activity of folding, normal and strike-slip faulting is documented by mutual overprint of the deformation fabric belonging to each tectonic component (*Fügenschuh et al.,* 1997, *Axen et al.* 1995, *Rosenberg et al.* 2008).

Along the western margin of the Tauern Window crops out a series of Pennidic units, namely (according to *Schmid et al.,* 2013):

1. Venediger Nappe System, that includes: (i) The european basement made of para- and ortho-gneisses, schists and migmatites of pre-Variscan age with a metamorphic grade ranging from greenschists to amphibolite facies (*Schmid et al.,* 2013). (ii) The Calcalkaline I-type Zentralgneise intrusives formed during a subduction-related magmatism between 310 and 295 Ma (*Cesare et al.,* 2002), followed to a Late Carboniferous – Permian rifting

stage (*Eichhorn et al.,*2000; *Veselá et al.,* 2011). The Zentralgneise granitoid compositions spread from tonalite to granite, but locally are also preserved gabbroic and ultramafic cumulates (*Cesare et al.,* 2002). The Ahörn, Tuxer and Zillertal Gneiss Core are the result of the deformation of the Zentralgneise intrusives during the alpine metamorphism.(iii) The post-Variscan cover (also named Untere Schieferhülle in the older literature) encompasses terrigeneous, carbonatic and volcanoclastic sediments of Permian-Cretaceous age (*Veselá et al.,* 2011).

2. Rote Wand – Modereck nappe is made of basement gneisses thin slices and para-autoctonous covers (quarzites, calcitic and dolomitic marbles, calcareous michaschists and prasinites) that previously formed the distal european margin next to the oceanic transition (*Kurz et al.,*1998). This series formed during Triassic-Cretaceous time.
3. Glockner Nappe encompasses amphibolites and prasinites, meta-pelites and calcareous micaschists of Cretaceous age deposited on the former Glockner oceanic basin (ophiolite-bearing unit, *Kurz et al.*, 1998).

The Alpine metmorphism and deformation recorded in these units can be summarized in the following points (according to *Schmid et al.,* 2013):

(i) phase of accretion of the distal european margin during which Glockner Nappe joined to the Austroalpine nappe pile reaching the active subduction margin of the Piedmont-Liguria Ocean (D1 at ca. 90 Ma);

(ii) subduction of Piedmont-Ligurian and Valais oceanic crust along with the Glockner nappe and part of the Modereck system; high – pressure metamorphism at 2,5 GPa and 580-650°C took place at this time (*Goldny et al*. 2008; *Luth & Willigshofer*, 2008; D2, 45-35 Ma);

(iii) accretion of continental crust and exhumation of HP units and isoclinal folding of Glockner and Modereck cover nappes upon the subducting distal european margin (i.e. the Venediger Complex; D3, 38-32 Ma);

(iv) Venediger Duplex Nappe formation and complete accretion of european crust into the Austroalpine nappe pile and formation of the Venediger Duplex

nappe system; Barrovian regional metamorphism at 550-600°C and 0.4-0.7 GPa (Tauern "Kristallisation", D4, 32-28 Ma);

(v) Folding and doming, lateral escape and exhumation of the Venediger Duplex as a consequence of the indentation of Adriatic Plate . Actually, strike-slip faulting started earlier in the northern side of the future window (Ahorn shear zone, 32 Ma). Activity along the Brenner fault started about 20 Ma (D5, 23-17 Ma). The period between 29 and 21 Ma is characterized by shortening in the outer Alpine chain and by an incipient stage of uplift, exhumation and erosion in the Tauern Window region.

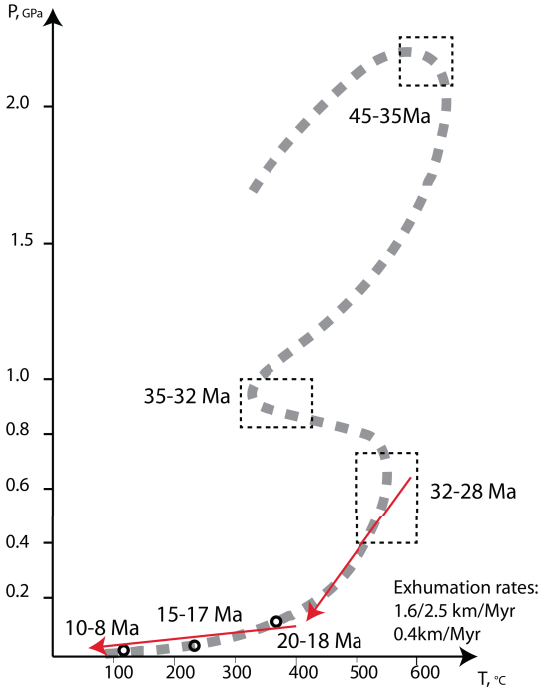

Figure IV: General P-T-t path for the Tauern Window. Dots in the terminal portion of the retrograde path represents dates for the Mesule area, from Selverstone (1985); Luth & Willingshofer (2008)

In Fig. IV is reported ta general P-T-t path for the Pennidic units exposed in the Tauern Window. The timing of the retrograde path, from Barrovian metamorphic peak (at ~30 Ma) toward surface conditions, varies from place to place inside the Tauern Window. In fact, as it is shown in cooling maps of *Luth &Willigshofer* (2008), thermochronologic ages defines two "younging" trends parallel and

perpendicular to the tectonic window strike, reflecting the gradual westward unroofing and the internal folding of the Pennidic units. Indeed, cooling ages are get younger from the interior westward to the Brenner line, and from the southern and northern border toward the inner portions. This dome-shaped thermal anomaly arose as a consequence of heat advection related to uplift of Pennidic units (between 30 and 23 Ma, *Luth &Willigshofer,* 2008). In this period, high uplift rates are accompanied to low cooling rates. Instead, high cooling rates are obtained for the period of time characterized by the climax of lateral escape tectonics between 22 and 12 Ma (*Goldny et al.,* 2008; *Kuhlemann et al.,* 2001; *Luth &Willigshofer,* 2008), during which the 20% of exhumation of the entire window has performed by erosion (*Kuhlemann et al.,* 2001). Therefore, most of the exhumation should have been carried out through tectonic activity. Hence, the westward younging should be accompanied by ductile and brittle exhumation structures which comparison and activity started earlier inside the window and then proceed toward the western border.

Chapter 1.

Structure of the SW Tauern Window

The structural field work was aimed to identify and map the structures associated with the different tectonic components that Pennidic units of the southwestern Tauern Window should have ideally experienced, i.e.: (i) thrusting associated with the stage of nappe stacking; (ii) strike-slip associated with the component of lateral escape, and (iii) normal faulting associated with the unroofing of the exhuming nappe pile which is commonly referred to the activity of the Brenner Fault system.We have investigated the south-western part of the Tauern Pennidic Unit along two transects (Fig. 1): (A) N-S-trending transect across the Zillertal Gneiss Core from the Neves area to the Zemmbach Valley, and (B) E-W transect of ca. 8 km from the Moosboden glacial cirque to the Hochfeiler area. In the following sections each transect is described area per area.

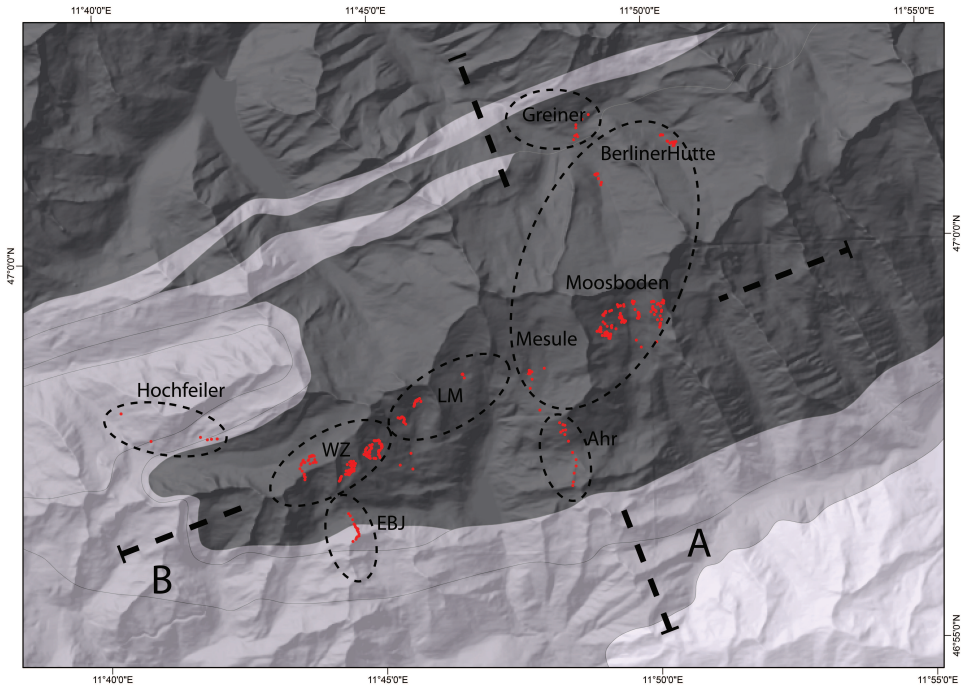

Figure 1: Geological sketch and distribution of the studied areas with the trace of two perpendicular transects A and B. Ahr: Ahrntal shear zone; LM: Laghetti-Muttenockkar; WZ: Weisszint; EBJ: Eisbruggjoch.

1.1 Results of structural survey

1.1.1 Mesule – Moosboden – Berlinerhutte areas

These three areas are grouped together as they show almost identical structural features. The characteristic feature of these areas is the occurrence of meter- to hundreds of meter- wide low-strain domains which largely preserve the pristine magmatic structure though pervasively overprinted by amphibolite facies metamorphism. T

The Zillertal Gneiss core is mainly composed by (meta-) granodiorites and tonalites, with subordinate bodies of ultramafic cumulates and gabbroic-dioritic masses (Moosboden area). Along the northern border of the area the metamorphic complex intruded by the Zentralgneis batolith is exposed.The excellent preservation and exposure of the magmatic structures has allowed the sequence of intrusive events to to be defined. This sequence includes, from the oldest to the youngest event:: (i) gabbros and granodiorites; (ii) mafic dikes with magma – mingling relationships with the granitoids; (iii) aplite and pegmatite dikes; (iv) lamprophyre dikes. The pre-Alpine structures also include pervasive sets of joints and epidote-garnet-filled veins surrounded by alteration halos locally of as much as metric thickness. Mafic microgranular enclaves (MME) and dikes with magma-mingling, along with the occurrence of orbicular diorites record the coexistence of basic and granitoid melts. Often, MME and biotite trails define a well preserved magmatic foliation. (For further information see *Ceccato, 2012*).

Low-strain domains are bounded by heterogeneous shear zones and mylonitic belts which range in thickness from centimetres to tens of meters, forming a complex and often anastomotic network. Each “planar” lithological contact and structural discontinuity (such as joints and veins) were exploited by ductile shear The basement gneisses of Zentralgneis host rock are also reactivated in a ductile manner. The orientation of magmatic contacts and structural discontinuities span all over 360° and are commonly steeply dipping. Ductile shear zones exploited any pre-existing structure independently of their orientation and therefore the

shear zone span the entire range of 360° orientations (Fig. 1.1.4). Ductile deformation occurred under amphibolite facies conditions and garnet, biotite where stable along the foliations.

A steeply dipping foliation, delineated in the field by isooriented biotite, is common within the low-strain domains overprinting the former magmatic structures; the average orientation of the foliation is N157E/87 (S-bulk; Fig. 1.1.5). Ductile deformation is accompanied by cyclic generation of veins filled with quartz, biotite, calcite and plagioclase (Fig. 1.1.2c; *Cesare et al.* 2002). These veins were involved in the subsequent ductile deformation in many cases. Veins formed as Mode-I (extensional) fractures or as hybrid fractures. The former have an average orientation of N070E/82. The latter commonly show asymmetric geometries indicative of the sense of shear during opening, such as wing cracks or pull aparts, and displace crosscut markers. These hybrid veins show a ductile shear overprint with the same sense of shear as the opening sense. Locally metasomatic halos are present along vein selvages. An alteration halo, locally a few meters wide, is also present around some shear zones and precursor joints. These haloes are commonly characterized by the extensive growth of amphibole crystals ("Garbenschiefer" of *Steffen et al.,* 2001). The Garbenschiefer are typical and pervasively developed along the major shear zone (Greiner Shear Zone: *Steffen et al.*, 2001) bounding the north the study area. Cataclastic brittle structures crosscut the ductile structures without exploiting the pre-existing fabrics. They occur as conjugate set of en-echelon cataclastic strike-slip faults and shear fractures, and as quartz-chlorite-epidote-filled extensional veins (Fig. 1.1.3a). Cataclastic faults accommodated offsests of as much as a few tens of meters (but commonly on the order of cm or dm); they are segmented into en-echelon structures from the millimetre to the meter scale. The faults include both dextral and sinistral structures conjugate around a shorthening direction of N-S, defined by the bisection of the acute angle between dextral and sinistral faults.

En-echelon tension gashes define conjugate planes with orientation and kinematic similar to that of shear fractures and faults. Sometimes, sigmoidal tension gashes are observed (Fig. 1.1.3b). On exposed, fault surfaces there is a well defined

lineation usually defined by oxides and/or chlorite grooves. Lineation strikes N157E and plunges with variable angle (from 15° to 56°) both toward NW and SE without any regard to fault kinematics. Commonly, segmented dextral faults show a sinistral stepping, and sinistral faults show the opposite stepping(*Pennacchioni & Mancktelow,* 2013). As a consequence the stepover domain is contractional and characteristically shows the development of a set of small antithetic faults that accommodates the large displacement gradient between fault central portion and their tips (Fig. 1.1.3c). Antithetic planes to dextral and sinistral fault have different orientation: (i) Antithetic to Dx faults – N305E/60; (ii) Antithetic to Sx faults – N250E/65. Fault slip was in the order of tens of centimetre to tens of meters. The largest slip was observed in the Mesule fault (*Pennacchioni & Mancktelow,* 2013). Quartz-chlorite-epidote-filledveins have an average orientation of N258E/63 and are typically surrounded by a cm- to dm- wide alteration halo ("Alpine-type vein halo").

Chl-qtz veins are often observed to overprint the previous qtz – bt ductile veins. In the Mesule area joints and small faults are decorated with epidote-chlorite-zeolite mineralizations; instead in other areas joint and faults are preferentially decorated with chlorite-zeolite-oxides.

The episyenites described in detail later in the thesis, come from this area. The best examples are from the Mossboden area, but small outcrops have been found in front of the Mesule glacier; loose blocks of episyenites are frequently observed in moraine deposits.

1.1.2 Greiner shear zone

The northern part of the Mesule – Moosboden – Berlinerhutte zones is characterized by a kilometre wide mylonitic belt known as Greiner Shear Zone marking the contact between the old european basement (host rock of the Zentralgneise unit) and the cover sequences represented in this area by marbles, calcschist, quartzite and serpentinites.. This zone is reported in the literature as a sinistral strike-slip shear zone. The data collected in the area during this thesis however indicate a least locally a dextral kinematics. Average orientation of the

foliation is N315E/70.

1.1.3 Ahrntal shear zone

The southern border of the Mesule – Moosboden area is also marked by a kilometre wide shear zone as the Greiner Zone. The rocks have a well-developed S-L to locally, L-type fabric. This mylonitic belt forms the northern limit of the Ahrntal shear zone. It is located at the southern contact between the Zentralgneise unit and its autochthonous cover (Hochsten marbles) and the Rote Wand-Modereck nappe. The orientation of the main foliation is N339E/48, with a stretching lineation plunging 10° toward N260E. Kinematic indicators are both dextral (e.g. sigma and delta clasts in Fig. 1.1.2e), and sinistral (e.g. C' – planes with mean orientation of N296/46). The southern limit of the investigated area presents a weak subvertical foliation that strikes N080E with a well defined stretching lineation (N255/10).

Aplitic dikes, mafic bodies and quartz vein are completely transposed in the main foliation. Faults and quartz–chloriteveins crosscut at a high angle the foliation (Veins: N071/89).

1.1.4 Laghetti – Muttenockkar area

The “Laghetti”-Muttenockkar area extends on the west of the Mesule-Moosboden area. and show some peculiar characteristics. Ductile structures include thick mylonitic horizons (1 – 5 m wide) bounding low – strain domains that include minor shear zones nucleated on different structural and compositional planar discontinuities. Poles to shear zone planes are less dispersed than in the Mesule-Moosboden area, forming an open cluster at circa N120E/30.

Along with domains with a heterogeneous strain distribution, there are domains where the deformation is homogeneous, and characterized by L-type tectonites (gneisses). The stretching lineation of the localized shear zones is identical to the lineation of the L-type gneisses and is oriented N260-280E/15. The gneisses show a weak subvertical foliation (Fig. 1.1.2b).

Major shear zones exploited lamprophyres, which could be several hundred meter long structures. The main kinematics of shear zones after lamprophires is dextral. Within the lineated gneisses, lamprophyres are sheared and buckled forming asymmetric Z–shaped folds looking to the west. The fold axis is parallel to the lineation.

The brittle structures of the area consist of a series of intersecting strike-slip faults and by extensional mode-I fractures and veins. As described above for the Mesule-Mossboden area, faults did not exploit pre-existing structures.
In the Laghetti area an outcrop exposing a network of faults has been mapped in detail (Fig. 1.1.1). This outcrop show the rare occurrence of an extensional linkage between fault segments (reported in Fig. 1.1.3d). The observed offset are locally controversial and can be related to the cut effect of the outcrop in addition to the partial dip-slip component of those faults.
The characteristic feature of many fault is the presence of a coating of the fault surfaces by small (mm-cm) quartz crystals grown in an open space. This feature is similar to the quartz cemented breccia along the Mesule fault (*Pennacchioni & Mancktelow*, 2013) with the quartz deposition postdating the main slip event along the fault. This mineralization is potentially related to the episyentite event.

1.1.5 Weisszint–Gliederferner area

Further west, between the Weisszint peak and the glacial tongue of the Gliederferner, the rocks are characterized by a pervasive ductile L-fabric, with an average orientation of lineation of N265E/15. A subvertical weak foliation (mean orientation N175E/85) is also present, and coincides with axial plane foliation of buckled lamprophyric and aplitic dikes. Heterogeneous shear zones with sigmoidal foliation (up to 10 cm thick) and mylonite horizons are also present. Structural and compositional discontinuities are exploited by localized shear zones. There is a gradual transition between L and major SL domains on the scale of cm to meter. Mylonitic horizons and shear zone exploiting compositional heterogeneities are folded and transposed within the main foliation (e.g. sheared

and buckled lamprophyric dikes, Fig. 1.1.2f) but their kinematics is still commonly recognizable. In some cases joints and small heterogeneous shear zone crosscut discordantly the L-fabric (Fig. 1.1.2d). These shear zones are usually oriented N340E and dip northward. North-dipping shear zones are widespread in the Nieder Weisszint peak area. Folds have an asymmetric "S" type geometry looking to east. Major shear zone (a few meters thick) are dextral.

Brittle deformation commonly overprint the ductile fabric. As in the other areas, cataclastic faults are arranged in en-echelon arrays and are segmented: dextral faults show a sinistral stepping; –sinistral faults show dextral stepping. The switch in slip sense between dextral and sinistral faults occurs at an orientation of N265E. Lineation strikes N170E with a variable plunge both toward SE and NW. Cataclasite are commonly associated with large volumes of massive quartz locally present as euhedral microcrystals. Episyenites are common. Sigmoidal tension gashes are observed.

1.1.6 Hochfeiler and Eissbruggjoch cover sequences

The Weisszint area is bounded along the southern and northern border by the cover sequences of the Modereck and Glockner nappes along the Eisbruggjoch and Hochfeiler zones.

Hochfeiler area. The cover sequence includes (from bottom to top): marbles, quartzites, garnet micaschists and calcschists. Further north, ophiolites (prasinities and calcschists-marbles) of the Glockner nappe crops out. The rocks have a well defined foliation dipping to the NW, with a stretching lineation that plunges more and more steeply moving away from the Zentralgneis (from N264E/34 inside quartzites near the contact, to N294E/65 in the marble of the Glockner nappe). A crenulation lineation is present (calcschists, N060E/19; N248E/10) and is parallel to the fold axes of parasitic Z-shaped folds (looking to the east). A zone of intense (mylonitic) deformation separates quartzites from garnet micaschists, with an orientation of N324/58, a stretching lineation of N289/49 and a top-to-the-NW kinematics.

Cataclasites have been found in loose blocks, but no faults have been observed in outcrop.

Eisbruggjoch area. The area is located at thecontact between the Zentralgneis unit, the autochthonous cover sequence (Hochstegen marble) and the ophiolitic micashists and calcschists of the Kaserer series (Rote Wand-Modereck nappe). Gneisses outcropping around the Eisbruggjoch hütte show a pervasive lineation oriented ENE-WSW with variable plunging (N076E/24; N260E/04). The subvertical foliation strikes N85E. A pervasive foliation, with variable orientation characterizes the metasediment sequences. Crenulation lineation and fold axis strike around N85E and dip variably eastward and westward. The axial planes of parasitic folds verge towards north (average orientation is N160E/80). The scattering of foliation orientation may be due to folding around E-W fold axes.

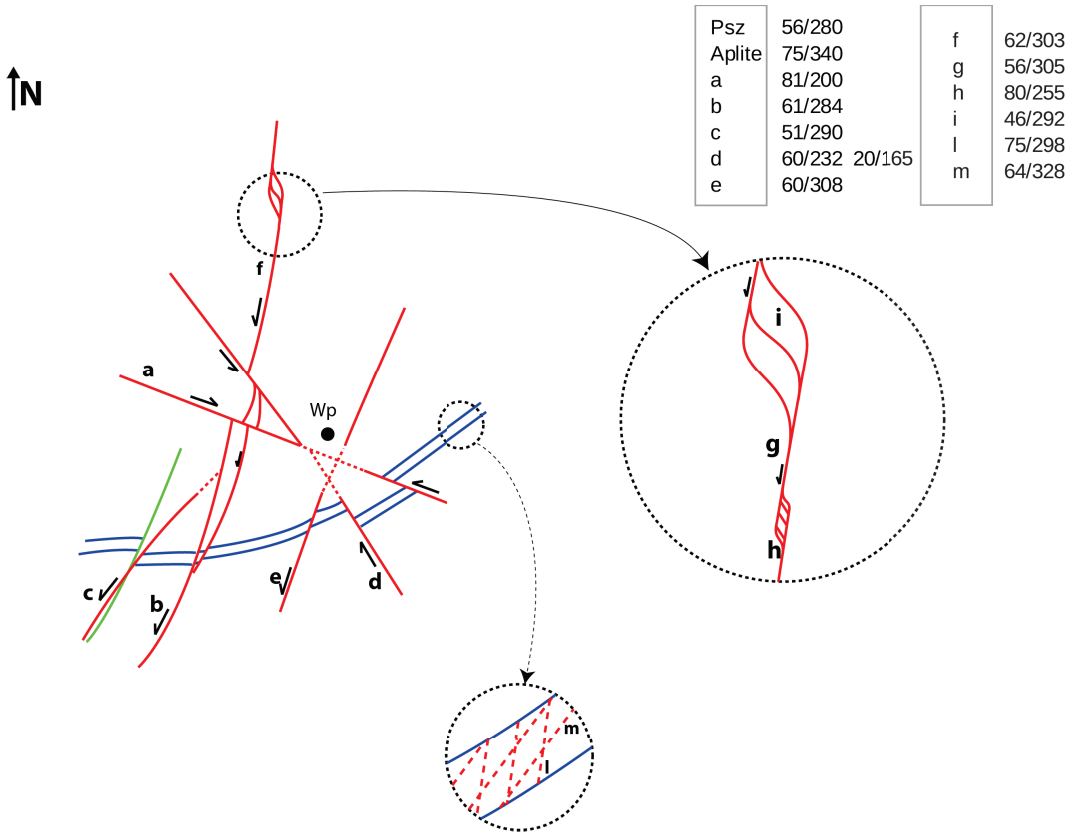

Figure 2: sketch of the Laghetti fault outcrop cited in the text.

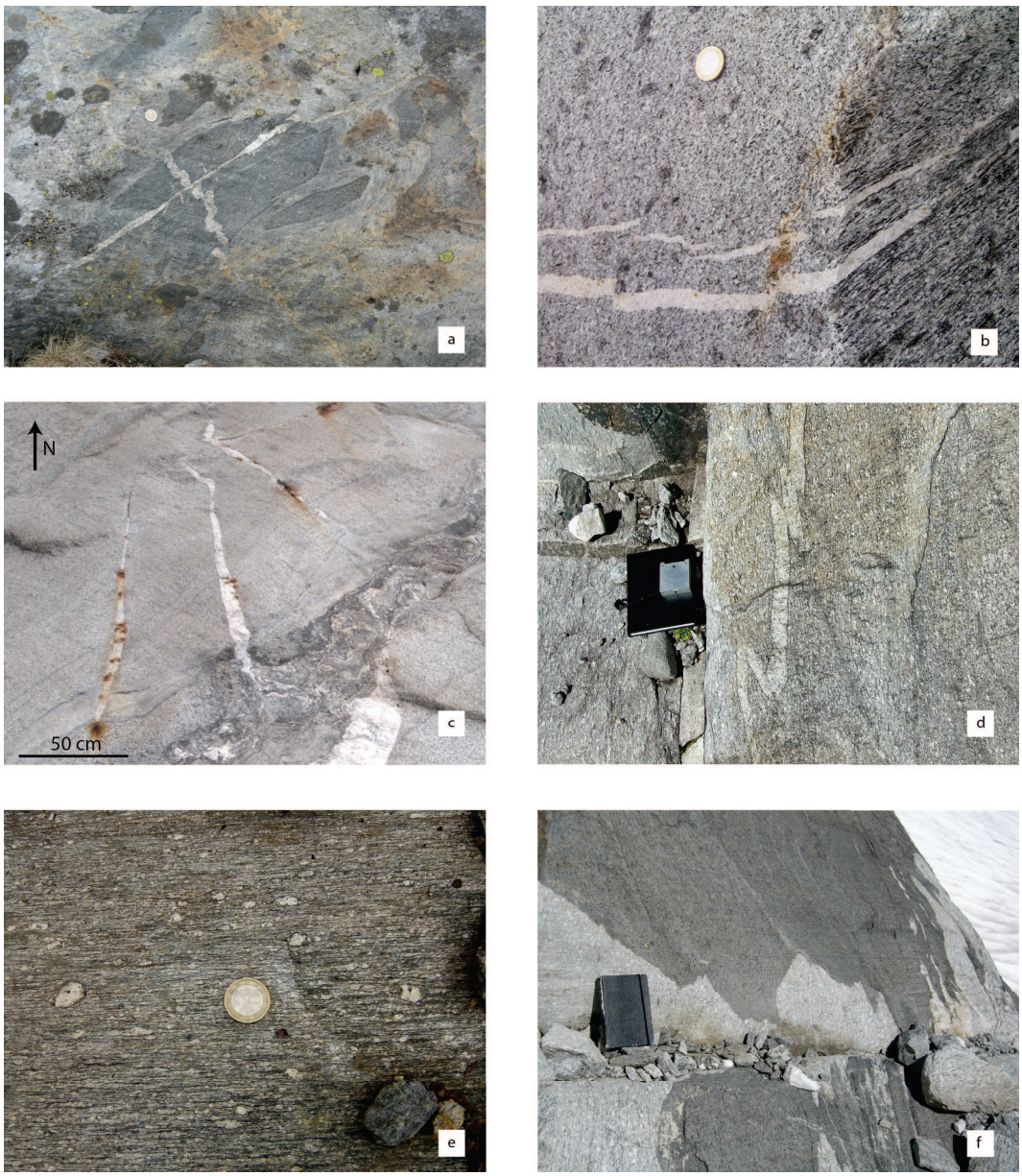

Figure 3: ***(a)*** *Boudinage and buckling in the Zentralgneis host rock oriente respectively, perpendicular and parallel to the inferred shortening direction (N345E); looking down, North upward;* ***(b)*** *Pervasive lineation and buckling in the L-gneisses of the Weisszint zone. Aplitic dikes develops lobes-and-cusps folds perpendicularly to the stretching lineation.* ***(c)*** *Qtz-cc-bt-pl veins showing three differentkinematics (left: no shear; central: sinistral shear; right: dextral shear).Their kinematics is coherent with the inferred shortening direction (Moosboden area).* ***(d)*** *High-temperature joint croscut folded aplitic dkes transposed into the main L-fabric of the Weisszint area.* ***(e)*** *Mylonitic fabric of the Ahrntal shear zone showing dextral sigma- and delta-clasts.* ***(f)*** *folded contact between gneisses and lamprophyre showing different geometries of parasitic folds (Wiesszint area).*

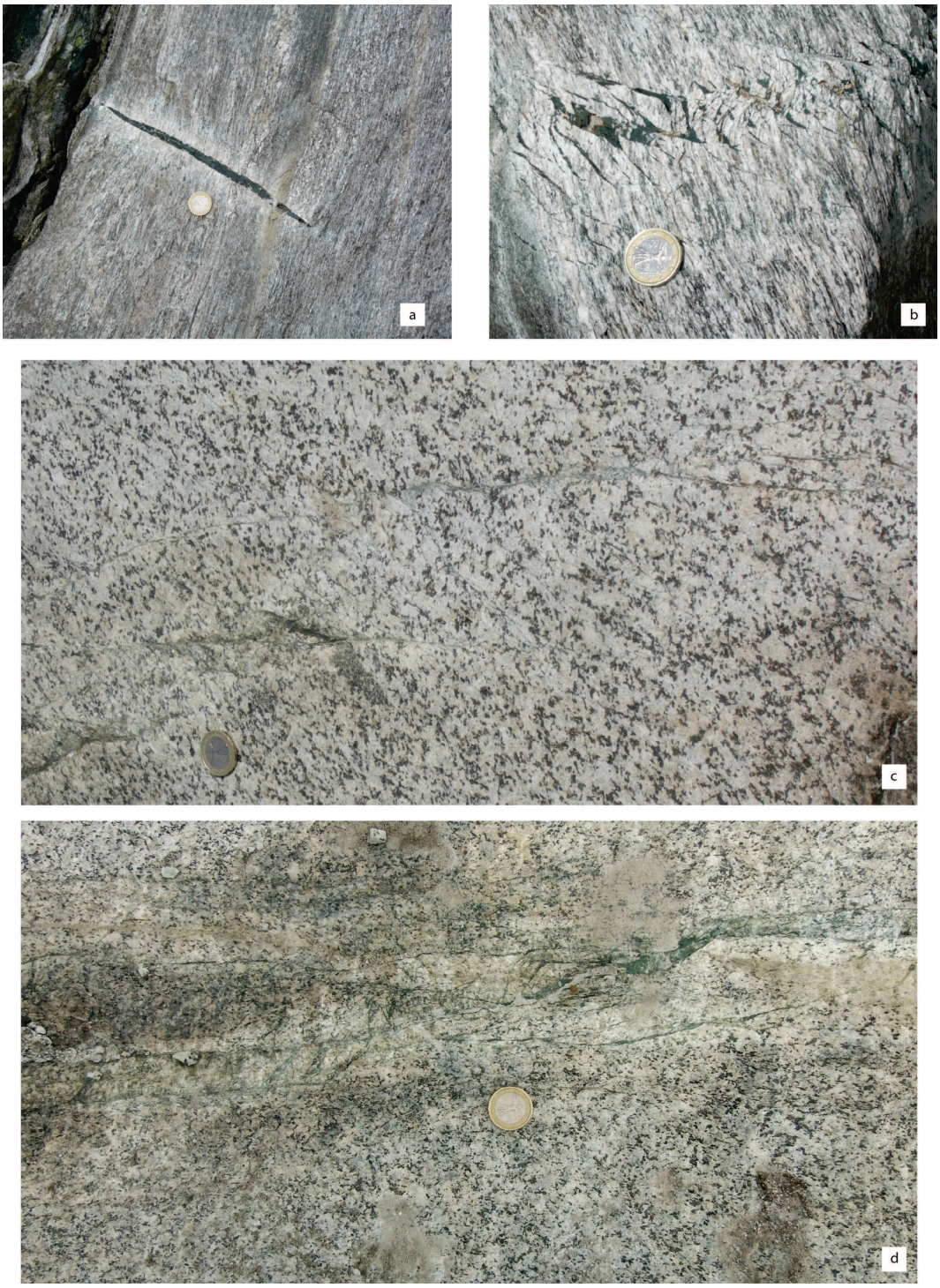

Figure 4: ***(a)*** *Extensional chl-filled vein with the typical Alpine-type alteration halo along the selvages, Moosboden area..* ***(b)*** *sigmoidal tension gashes that show multiple events of shearing and extensional fracturing (Moosboden area).* ***(c)*** *contractional jog between twoen-echelon segment of a fault (note the sinistral stepping between the two segments; Moosboden area);* ***(d)*** *Extensional jogs between sinistral segments of a fault (note the sinistral stepping between adjacent segments, Laghetti area).*

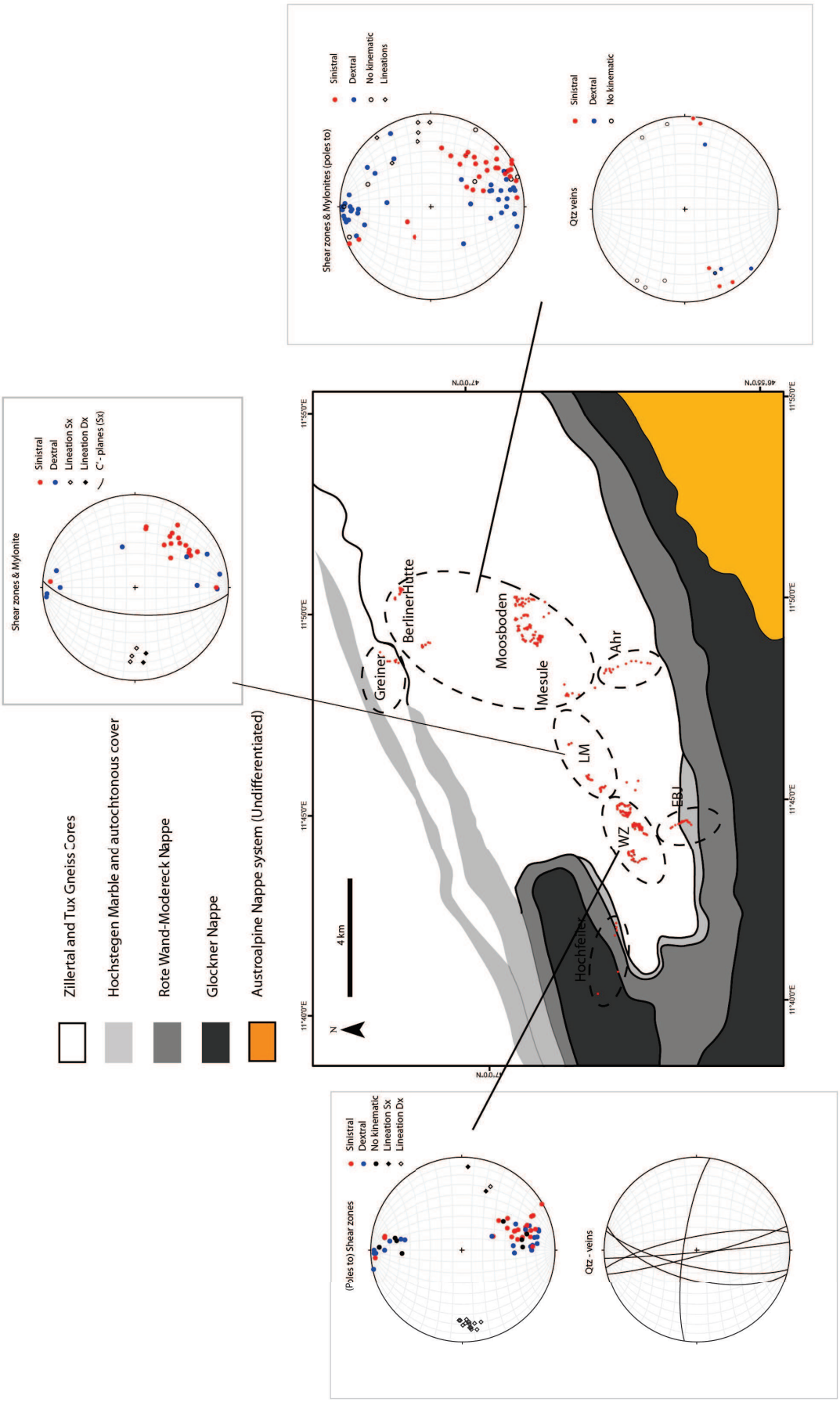

Figure 5: Representation of structural data from ductile shear zones. Is worth noting the rotation of structures from scatterd orientation toward a precise and peculiar trend from the West to East.

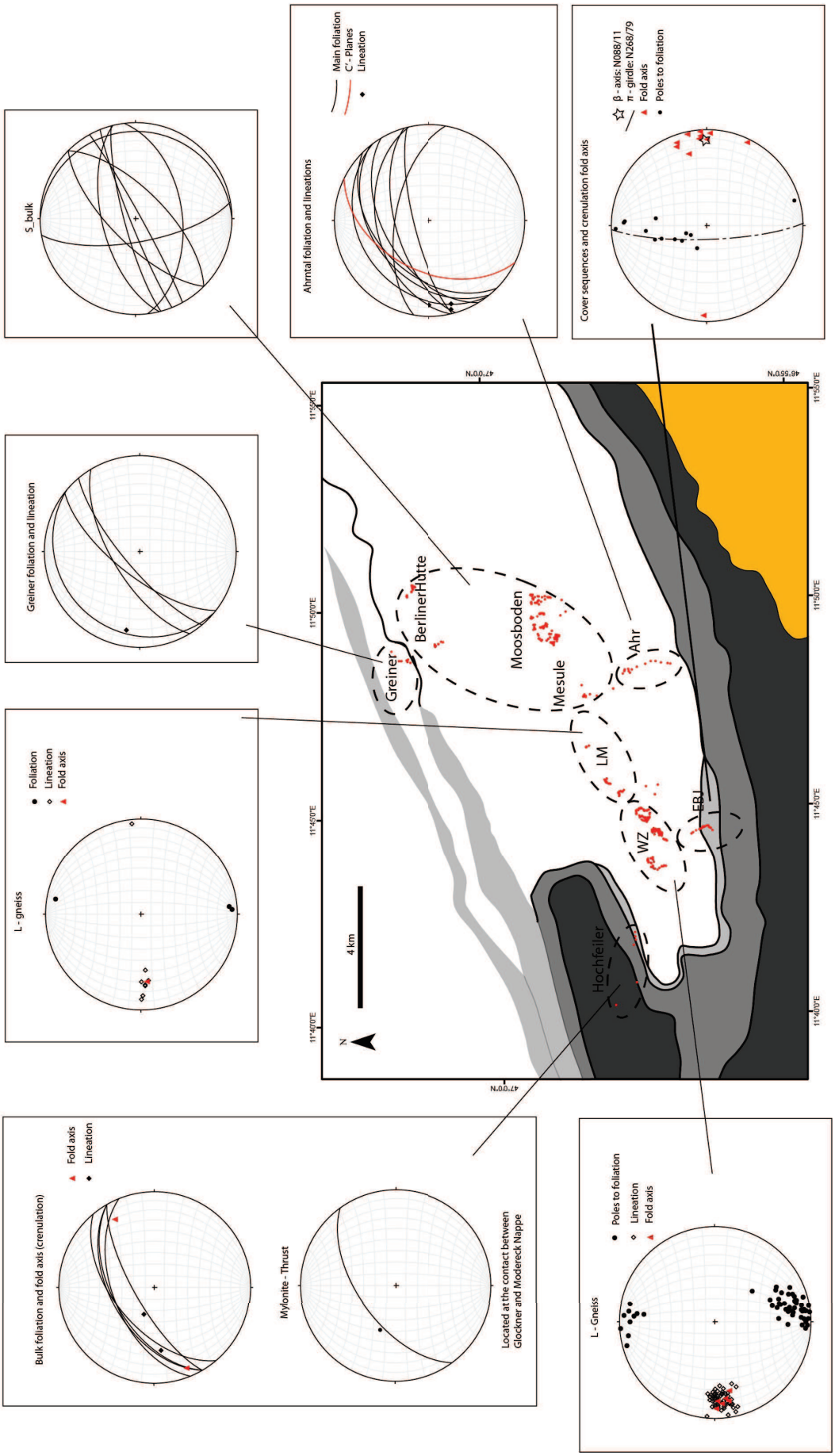

Figure 6: Representation of main rock structural feautres (foliation, lineation, fold axes, ...).

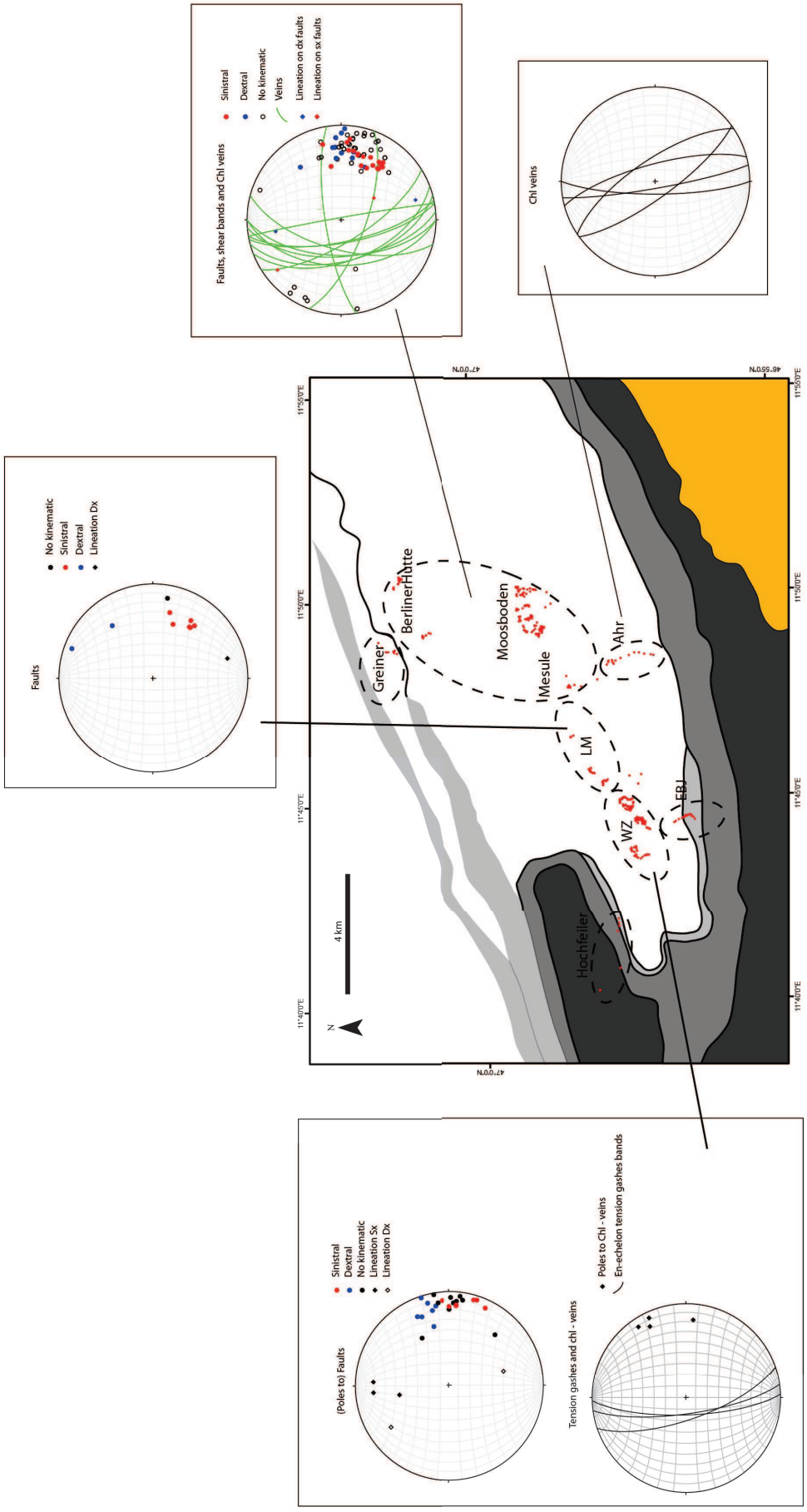

Figure 7: Orientation and kinematics data of faults and qtz-chl veins.

1.2 Structural framework of the studied area

The field structural analysis has revealed the presence of different ductile deformation structures and of a heterogeneous distribution of deformation.

The eastern area (Mesule-Moosboden-Berlinerhutte area, Greiner and Ahrntal Shear Zone outcrops) shows a scale-independent partitioning of ductile deformation on major and local strike-slip shear zones. On the kilometer scale, two major subvertical ENE striking strike-slip shear zone (Greiner Shear Zon,e to the north, and Ahrntal Shear Zone to the south) bound the Zillertal Gneiss Core (ZGC), that can be approximated as a multikilometric low strain domain. Inside the ZGC lower order strike–slip mylonites, exploiting structural discontinuities and compositional boundaries, outline outcrop-scale low strain domains where deformation is homogeneously distributed and display a subvertical ENE striking

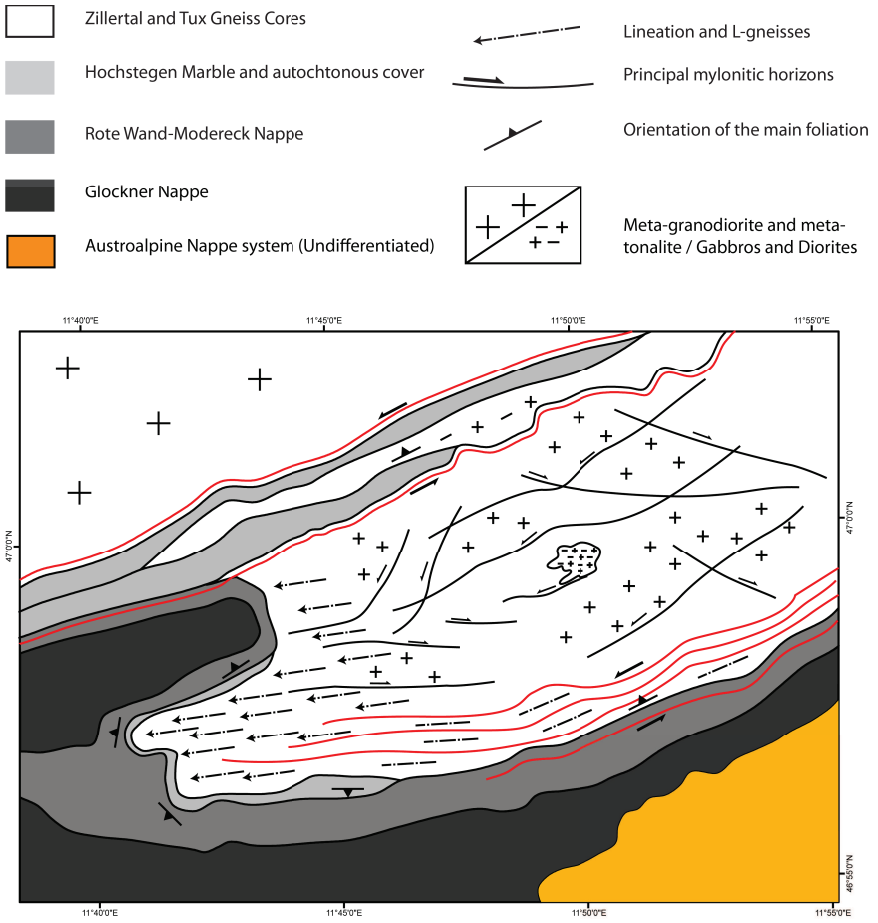

Figure 8: Simplified geological maps of the Zillertal Gneiss Core in the Southwestern Tauern Window.

bulk foliation. Quartz-calcite-biotite-plagioclase veins commonly accompany ductile deformation, and are in turn involved in the ductile deformation.
In the western area (Hochfeiler, Weisszint and Eisbruggjoch areas) ductile deformation is more homogeneous inside the ZGC, and gave rise to pervasively lineated gneisses. Subvertical strike-slip mylonites are usually transposed into the main weak foliation, but in some cases small heterogeneous shear zones crosscut the L-fabric. Small scale features, such as parasitic folds and axial plane foliation, suggest the presence of a regional anticlinal fold which limbs and axial zone are respectively located along the cover sequences of Hochfeiler-Eisbruggjoch areas and along the ZGC. Ductile deformation is accompanied by pervasive veining. The change in deformation style between the Mesule-Moosboden and Weisszint areas occurs approximately in the Laghetti-Muttenockkar area. Here, the Ahrntal Shear Zone gradually disappears, splaying into a set of narrow and discrete north-dipping shear zones that are frequently observed in the westernmost region.

Brittle deformation is recorded throughout the whole area by subverticalstrikeì-slip faults and chlorite-quartz-epidote veins scattered arount a N-S shortening direction. Faults are segmented and typically arranged in en-echelon arrays at all scales. Only “minor” faults are present in the area with a maximum offset of a few meters. Commonly, en-echelon chl-qtz veins define sigmoidal tension gashes.

1.3 Discussion

1.3.1 Deformation sequence

The deformation sequence for the studied area can be summarized as follow:

1. The deformation sequence includes two main stages: a first stage of ductile deformation, syn-kinematic to amphibolite facies metamorphic conditions (*Pennacchioni & Mancktelow*, 2007; *Cesare et al.*, 2001); and a later brittle stage developed under subgreenschist facies conditions (*Pennacchioni & Mancktelow,* 2013).

2. The ductile deformation is heterogeneously distributed. At the kilometer

scale, the eastern portion of the investigated area consists of a large low strain domain (preserving extensively the intrusive fabric of pre-Alpine intrusive protolith to the Alpine amphibolite-facies deformation), bounded both north and south by two major (a few km thick) mylonitic shear zones referred to as Greiner and Ahrntal Shear Zones, respectively. In contrast, the deformation in the western part is more pervasive and the overall structure geometry resemble that of an ENE striking anticlinal fold. At the outcrop scale shear zones exploited precursor structural (e.g. fractures) and compositional (e.g. dykes) heterogeneities. The shear zones have a variable orientation and show a strike-slip kinematics. Based on the switch between left- and right-lateral shear zones the shortening direction during ductile deformation can be constrained at N345E. This orientation coincides with the average direction of most amphibolite facies extensional veins (filled with quartz, biotite, calcite and plagioclase). The poles to foliation in low – and high – strain domains fall within the range N337-349E, almost parallel to the inferred shortening direction. Veins and foliation are then perfectly perpendicular: this means that the principal axes of stress and principal finite strain axes have had the same orientation during ductile deformation, thus defining a perfectly coaxial stress field (*Pennacchioni & Mancktelow,* 2007). The inferred shortening direction is identical all over the studied region and indicates ththat there is no rotation/refraction of the stress axes at the regional scale across the tectonic unit.

3. The stage of brittle deformation following ductile shearing results in discrete but pervasive fracturing throughout the whole area. These brittle fractures include extensional and shear fractures, these latter having both dextral and sinistral strike-slip kinematics and arranged in sets of conjugate structures. Shear fractures and faults are segmented at all scales and are typically arranged in en-echelon arrays linked by contractional stepovers. Extensional veins usually display an en-echelon arrangement defining conjugate sets of tension gashes, commonly sigmoidal.Fault slip

is commonly on the order of centimetres to decimetre; faults with metric slips are rare. The switch in kinematic of faults around N270E, the average direction of extensional veins and the acute angle between conjugate structures all point to define a shortening direction close to N-S, therefore similar to the regional σ_1 during the precursor ductile/metamorphic stage (*Pennacchioni & Mancktelow*, 2013).

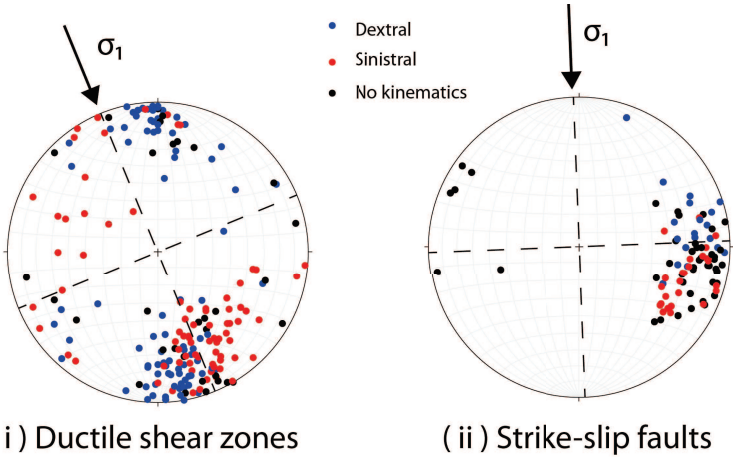

Figure 9: Comparison between the two shortening direction obtained respectively from: (i) switch in strike-slip ductile shear zone kinematic; (ii) switch in kinematics of

4. Both the ductile and the brittle deformation occurred under hydrous conditions as witnessed by the common occurrence of veins associated with deformation structures. The stage of high temperature, syn-metamorphic ductile deformation is accompanied by cyclic formation of quartz-calcite-biotite-plagioclase veins. Synmetamorphic fracturing was triggered by the geometric compatibility problems arising during the synchronous activity of non-parallel shear (*Mancktelow & Pennacchioni*, 2005). Veins were locally overprinted by ductile deformation and in turn crosscut the ductile fabric indicating several cycles of coeval brittle and ductile deformation under amphibolite facies conditions (*Pennacchioni & Zucchi,* 2013*; Pennacchioni,* 2005). The stage of faulting is accompanied by widespread formation of quartz-chlotite-epidote-feldspar veins and these minerals are the cause for cementation of cataclasites. The small acute angle between conjugate faults and shear bands (24° between the

average orientation of dextral and sinistral structures, respectively N261/67 and N288/65) result from fracturing in the presence of a fluid pressure and a relatively low differential stress.

5. The occurrence of tensile veins and hybrid fractures highlight the fact that the host rock during deformation can bear only small differential stress (lower than four times the tensile rock strength). This fact is likely to be due again to the constant presence of fluids and to fluid pressure cycling during both ductile and brittle deformation.

6. An episode of fluid-rock interaction postdated the main phase of faulting and is associated with the local development of episyenites.

1.3.2 Deformation partitioning and tectonic interpretation

Across the eastern part of the study area, ductile deformation is localized at the multikilometer scale onto two shear zones with a strike-slip kinematic (Greiner and Ahrntal) that bound a low-strain domain (the Zillertal Gneiss Core) characterized by coaxial deformation (*Pennacchioni & Mancktelow,* 2007), in which both the maximum and minimum axes of both stress and strain are subhorizontal and oriented respectively N345E and N075E (Fig. 1.3.1). At the outcrop scale, the deformation is also heterogeneous and the non-coaxial component is localized on a network of strike-slip shear zones of variable thickness (from centimetric to metric). Similarly to the "large" scale picture, the stress and strain axes have are subhorizontal and oriented accordingly to a shortening direction of N345E.In the western part of the study area, deformation is more homogeneous inside the ZGC, where a pervasive L-fabric is developed likely reflecting a pure constrictional strain (*Sullivan*, 2013).

The brittle deformation does not appear to have suffered a partitioning in the area. The whole region is characterized by the same architecture with widespread conjugate strike-slip faults and extensional veins consistent with subhorizontal maximum and minimum strain/stress axes and a shortening direction around N-S. Both the ductile shear zones and faults have a strike-slip kinematics that would

mainly account for lateral escape tectonics. This kinematics also dominates at the overall scale of the Eastern Alps during the retrograde path from peak metamorphic conditions (*Goldny et al.,* 2008; *Rosenberg et al.,* 2008).

No structure related to thrust tectonics have been observed: the unique exception that may be attributed to thrust tectonics is localized along the contact between cover units in the Hochfeiler area where a top-to-NW mylonite has been measured. *Selverstone* (1988) and *Oehlke* (1993) interpreted this structure as the folded surface of the nappe thrust between Venediger duplex and Modereck nappe. Thrust structures due to the latest phase of cooling of the already domed Pennidic nappe pile has been reported by *Wöelfler et alii* (2008) to crop out along the southern margin of the Window, south of the Neves lake. No structure linked to the extensional unroofing of the Zentralgneis units have not been identified even though the region is located in the centre of the western "younging" trend of cooling ages given by *Luth & Willingshofer* (2008). Ductile and brittle structures related with the activity of the Brenner fault and coeval with the footwall uplift have been reported by *Axen et al* (1995) in the nearest regions to the Brenner fault. A mylonitic foliation dipping slightly towards west overprints the former ductile structures (mylonites of the Zillertal and Tuxer Cores) but it affects a small volume of rock that extend about 5 km eastward, in map view, from the Brenner line. Our area is apparently free of Brenner-related extensional structures. It should be noted that, the extension direction (S80°W) inferred by *Axen et al.* (1995) is very similar to the orientation of the lineation of both strike-slip mylonites and L-gneisses. We have to admit that, *Selverstone* (1988) had already interpreted these linear fabric as the easternmost trace of the ductile Brenner activity. She describe also the slight difference between the orientation of crenulation lineation (due to regional folding) and stretching lineation (due to regional extension), that can be noted also comparing structural data from the Weisszint and Eisbruggjoch areas (β-axis and π-girdle). However, further investigations are needed in order to establish the exact relationship between the L-fabric and the western extension.The dip-slip extensional brittle faults described by *Axen et al.* (1995) are very similar in terms of general structure and paragenesis

to the dominantly (67% of measured structures) strike-slip faults observed in the area investigated in this thesis. Some authors (*De Vecchi & Baggio*, 1982; *Axen et al.* 1995; *Bertrand* 2010) described a gradual change in fault "regime" form the strike- and oblique-slip tectonics of the central Tauern Window, toward the eastern and western bounding low angle normal faults, explaining the different observed kinematic in our zone.

Numerical models show how strong can be the partitioning between crustal thickening, lateral escape tectonics and normal faulting during the evolution of the orogen and also across its thickness at the same time (*Seyfert et al.,* 2004).

As we can see in our area, convergence in a ductile environment (i.e. lower crust) can be accommodated by synchronous folding and strike – slip shear zones, as it has been already reported in similar tectonic settings (Simplon fault zone, *Manktelow & Pavlis,* 1994). Normal faulting seems to develops at higher structural levels and usually in the brittle field (*Axen et al.* reports that only the upper portion of fold hinges have been overprinted by the mylonitic foliation related to the Brenner fault). There would be, therefore, a partitioning of the strain component during the progressive convergence and uplift of the Tauern Window, with the extensional structures having being mainly localized at the base of the Brenner Fault within a thickness of a few kilometres in the footwall, and strike-slip and folding limited to the lower ductile environment.

–

The occurrence of a well defined homogeneous L-fabric in the western area (Weisszint-Hochfeiler) suggests the presence of a constrictional strain regime (*Sullivan,* 2013). In this zone of homogeneous deformation can be applied the models presented by *Fossen & Tikoff* (1998) for transpressive tectonics. Their "model E" describe a subhorizontal pure constrictional regime very similar to that observed in the southwestern Tauern Window. In fact, the prolate strain ellipsoid, the SL – L fabric and the horizontal lineation all together account for a type E transpression. This is also supported by the comparison between the orientation of structures in the zone of homogeneous deformation and the zone where strain is

repartitioned and original attitude of structures is preserved. This comparison highlights the strong rotation of planar fabric into a position perpendicular to the stretching direction (flow apophyses) and the neoformation of linear fabric in agreement with the strain regime above described (Fig. 1.1.4; transition from east to west). Such a tectonic setting can be also classified as a purely thinning deformation zone where lengthening dominates (*Tikoff et al.,* 1999). *Pennacchioni & Mancktelow* (2007) have shown the occurrence of a general component of simple shear diffuse over the whole region with a dextral kinematics. This is also in agreement with the kinematics of the two major bounding Greiner and Ahrntal Shear Zones (both sinistral)

This type of transpression is typical of convergent settings where margins have a convex geometry or there is a change in convergence vector along strike: these situations are expected to generate normal faults perpendicular to the margin that may accommodate exhumation of deep–seated rocks (*Fossen & Tikoff,* 1998). The shape of the Southalpine indenter, that should resemble that of the converging former margin, is generally convex (looking just at the switch in strike between the Giudicarie and Pustertal lineaments). The study zone develops just in front of the region where the former margin should present the maximum convexity. Therefore, the exhumation tectonics could be due also to this particular geometry, as it is well shown also in other zones of the Alps (Simplon faut zone, *Manchtelow & Pavlis*, 1994).

The model of transpression can be applied also to the eastern region (Mesule – Moosboden), given the constant stress field under which the entire region deformed during the Alpine metamorphism, but we have to be aware of the deviation from the theoretical model caused by strain partitioning.

The difference in rock fabric between the eastern and western poriton of the studied area could be due to the southern disappearance of the Ahrntal shear zone around the Lake Neves area. Actually, there is a gradual transition between SL tectonites of the eastern Ahrntal toward the L-genisses, as it is possible to see inside the Ahrntal shear zone where lineated gneisses are embedded in well

foliated mylonites; in the Weisszint area, instead, a few major SL mylonites crosscut huge domains of lineated gneisses. The Ahrntal Shear Zone seems to be gradually transformed in a set of narrow and discrete minor shear zones at the end of the major lineament just below the Weisszint. Therefore, the disappearenca of one of the major bounding strike.slip zones could have caused a changing in the partitioning of the strain.

–

No partitioning between the different tectonic component occurred between the high and low strain domain, as demonstrated by the overall strike-slip kinematics of the observed structures. Folding observed in the Hochfeiler area, which can be interpreted as the genetic process of L-gneisses, might be interpreted as a thickening process (as in San Andreas fault, *Teyssier et al.,* 1998), but no discrete planes related to thrusting have been observed.

–

In summary the structural study reveals that during the retrograde path of Alpine deformation, the whole study zone had experienced deformation under a relatively constant regional transpressive regime with a σ_1 in the range between N345° and N360°. This shortening direction has resulted in a first convergence phase that bring to the formation of stacked nappe pile by thrusting; traces have been overprinted by the ongoing deformation at the peak metamorphic conditions characterized by strike-slip shear zones linked to the lateral escape tectonics and folding parallel to the shortening direction and perpendicular to the extension direction. Extensional structures clearly related to the Brenner low angle normal fault activity have not been observed, and therfore the exhumation structures are relegated toward the Vizze region and Brenner zone. The partitioning in strain intensity over the region is not associated with a partitioning of components of thrusting, lateral escape and detachment in no stage of deformation, as is instead observed in other geological contexts (*Fossen et al.*, 1994).

1.3.3 Nucleation of shear zone

The investigated region provides an ideal natural laboratory for the study of the process of ductile shear zone nucleation. It shows spectacular glacier-polished outcrops within metagranitoids that preserve all stages of incremental development of structures in a relatively simple and "isotropic" material. Granitoids, such as that of the Zentralgneis units, are avoided of pervasive anisotropies, and are characterized instead by the occurrence of discrete compositional and structural discontinuities. Shear zones exploited these discrete anisotropies to nucleate and develop. The Zentralgneis unit has offered to Alpine deformation a wide variety of discontinuities on which it has been able to localize, allowing to us to constrains some of the parameters controlling shear zone nucleation and evolution.

In the study area there are two main types of isochoric simple shear zone. (1) Most of the observed ductile zone of deformation are heterogeneous, continuous and defined by a sigmoidal foliation. This usually develops along the selvages of tabular "strong" lithologies, inside the host rock (such as the paired shear zones developed along aplitic dikes and epidote-garnet vein halos). (2) Homogeneous shear zones shows a uniform distribution of strain across the whole zone as proved by the occurrence of a well define oblique foliation; often bound by undeformed host rock, this type of shear zone shows an abrupt decrease in strain intensity across its walls. This type usually develops exploiting weak lithologies bounded by stronger ones (as mafic dikes and lamprophyres).

The analysis of the whole set of compositional discontinuities has allowed us to identify a precise "hierarchy of deformation" that reflect the relative "strength" to the ductile flow, i.e. the viscosity contrast between adjacent lithologies The Zentralgneiscomponents are ordered in this way, from the weakest to the strongest: (i) lamprophyres, (ii) basic dikes, cumulates and ultramafic bodies, including the mafic microgranular enclaves, (iii) quartz veins, (iv) pegmatites, (v) granodiorites, (vi) epidote – garnet veins; (vii) aplite dikes. Hence, the type of exploited precursor determined the type of shear zone: (i) weak precursors

compared to the host metagranodiorites ("unfilled" fractures; quartz veins; biotite-rich basic dykes, Fig. 1.3.2c,d) localized strain: shear zones have commonly a rather homogeneous strain distribution and a sharp boundary to almost undeformed host rock; (ii) strong layers (aplite dykes; alteration haloes surrounding veins; Fig. 1.3.2a,b) localized the deformation at their boundaries forming paired shear zoned at their selvages mainly developed within the metagranodiorite.

Actually, the "strength" have to be interpreted as the viscosity of a rock. According to *Lister et al.* (1983), the viscosity (competency) contrast between two rock is the parameter that controls the localization of simple shear and thus the nucleation of simple shear zones. This competency contrast can be even small, as in the case of paired shear zones developed along aplite dyke selvages. The development of lobes and cusps folds in aplitic layer under a constrictional regime (Fig. 1.1.2b) is the proof of the small (less than an order of magnitude) competency contrast between granodiorite and aplite.

Therefore, any surface that correspond to a viscosity contrast could be exploited by ductile deformation as a site of nucleation for shear zones. Almost any structural or compositional (rheological) surface heterogeneity was capable of been exploited by localized shear deformation. Shear zones are linked to these heterogeneities and never extended beyond the original length of the structural/compositional precursors.

Sometimes, major shear zones develops through linkage of adjacent structures by the formation of a zone of intense and pervasive deformation (strongly foliated domains between step-overs). Pervasive deformation of host rock domains and/or high temperature fracturing/veining developed usually in response to geometric compatibility problems along the shear zone network. Veining is another expression of the high – temperature fracturing process already described in similar tectonic context (*Pennacchioni*, 2005; *Pennacchioni & Zucchi*, 2012). In our working area, this is spectacularly represented by the occurrence of discrete ductile heterogeneous and continuous shear zones crosscutting the L-fabric of the

Weisszint gneisses (Fig. 1.1.2d): if the heterogeneity pre-date the formation of the L-fabric, it would be folded and /or transposed into the main foliation as the nearby aplitic dyke. This is the demonstration that ductile shear zones need brittle precursors to nucleate and develop.

In contrast with numerical and rock-analogue models (e.g. *Mancktelow*, 2002) shear zone nucleation never occurred within homogeneous metagranodiorites simply because of the presence of isodiametric scattered weak particles (e.g. weak biotite grains or basic enclaves in the granodiorites). This never occurred also in cases of biotite alignments reflecting original late-magmatic healed fractures (*Mancktelow & Pennacchioni*, 2013).

ion of an aplitic dike with a zone texture: heterogeneous shear zones develop both at the contact between the granodiorite and the aplite and at the contact internal to the dike between composizional zones (Berlinerhutte area); ***(b)*** *paired shear zone developed on the alteration halo of an epidote-garnet vein crosscut a homogeneously sheared (at its interior) mafic enclave (Mesule area);* ***(c)*** *homogeneous deformation accommodated by the mafic components of a dike with magma-mingling texture (Moosboden area);* ***(d)*** *homogeneous deformation localized inside a lamprophyre: no foliation developed at the contact with granodiorite (photo: G. Pennacchioni, Mesule area).*

A compositional heterogeneity or a structural discontinuity remains itself also

during further event of ductile deformation. Therefore, it could be exploited several times, recording a complex history of deformation phases, necessarily not due to the same tectonic event. Reactivation of original ductile shear zones can explain the controversial sense of shear of some paired shear zones exploiting the alteration halos surrounding epidote – filled veins. In these shear zones generally, the offset of markers across the central vein appears opposite than that at the flanking heterogeneous shear zones (this latter being consistent with the shear sense of other associated Alpine shear zones). This occurs locally but consistently across the whole tectonic unit.

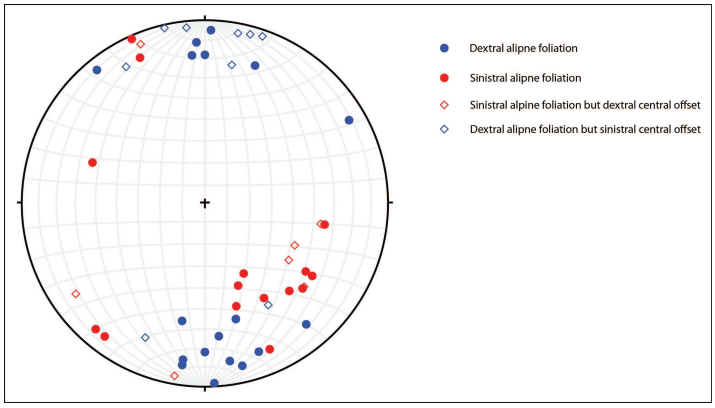

Figure 11: Structural data on orientation and kinematics of epidote-garnet veins and relative paired shear zones

These paired shear zones present a peculiar morphology: the central mm – thick vein is usually surrounded by a cm-wide alteration halo and the host rock inside it does not shows any trace of deformation (even if the general strain of the zone is very high, Fig. 1.3.5b). The central vein usually behaves as a discontinuous brittle (or brittle – ductile) shear zone. Alpine deformation localizes at the boundary of this halo: selvages are exploited as compositional and rheological discontinuities on which heterogeneous continuous paired shear zones nucleate. The competency contrast between the alteration halo and the host granodiorite is likely to be due to the microsctructure of plagioclase resultant from a process of fluid – rock interaction (*Mancktelow & Pennacchioni*, 2005). Veins have a ca. ENE-WSW preferential orientation and the alteration halo is not a constant features, but it is often not present or discontinuous along the same vein. Pull – apart structures and pods along the veins are frequently found.

In Figure 1.3.4 is reported the schematic representation of an outcrop of the Laghetti-Muttenockkar area, where several of these opposite markers have been investigated. The central vein and the surrounding altered rock do not present any particular foliation, suggesting that the discontinuity behaved as a fault-like structure (e.g. *Pennacchioni* 2005). The altered zone seems to behave as a whole localizing the Alpine deformation at its boundary preserving the internal structure. Where the alteration halo is not present, the displaced markers along the central

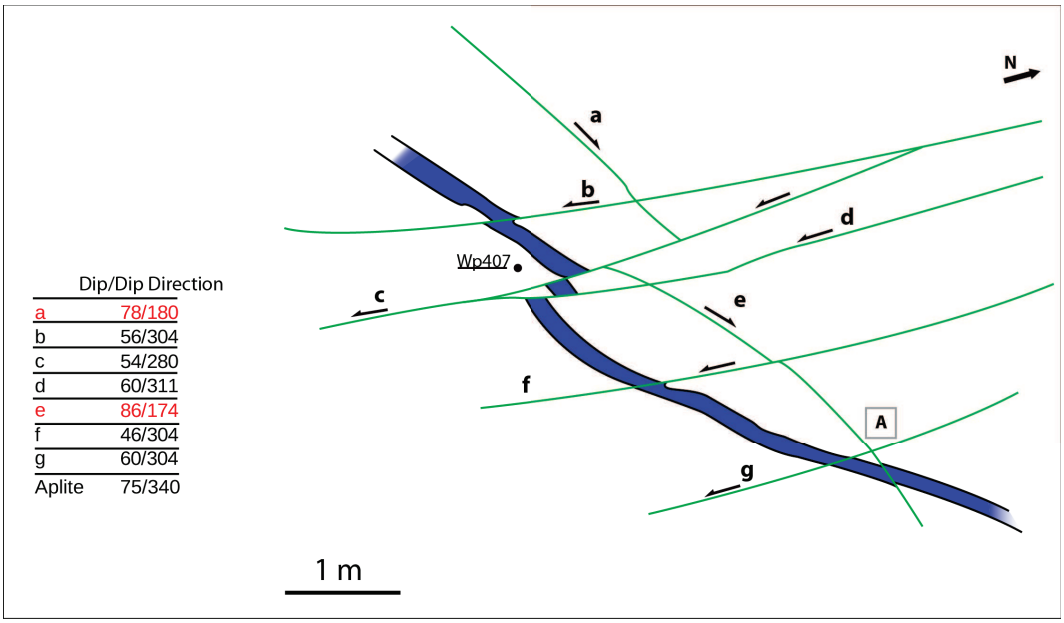

Figure 12: this outcrop shows a great number of controversial markers. Structures (A) are reported in Figure 1.3.5c,d.

vein are dragged into the sigmoidal Alpine foliation (Fig. 1.3.5e,a). Hence, veins with large halos preserve the original fault-like displacement along the central part, whereas structures with small halos present strong dragging of the marker. This peculiar geometry indicate that the development of the alteration halo post-dates the displacement along fault-like central veins, and pre-dates the development of Alpine sigmoidal foliation.

Conjugate structures have been also observed and the bisection of the acute angle is directed ca NW-SE. The development of these veins as extensional joint or shear fractures is not consistent with the Alpine stress directed ca. N-S. An inversion of the kinematic due to rotation of structures across the direction of

maximum lenghtening (ISA_1) as suggested by *Pennacchioni & Mancktelow* (2007) is unlikely to have occurred, since that structure orientation span over a wide range and kinematics do not show the expected switch around N075E.According to the above describe elements, the contrasting sense of shears are interpreted as due to Alpine reactivation of original ductile shear zones developed in the pre-Alpine granitoid protolith as result of the original evolution during pluton cooling similar to what is described for some intrusions elsewhere (e.g. *Pennacchioni*, 2005; *Pennacchioni and Zucchi*, 2013).

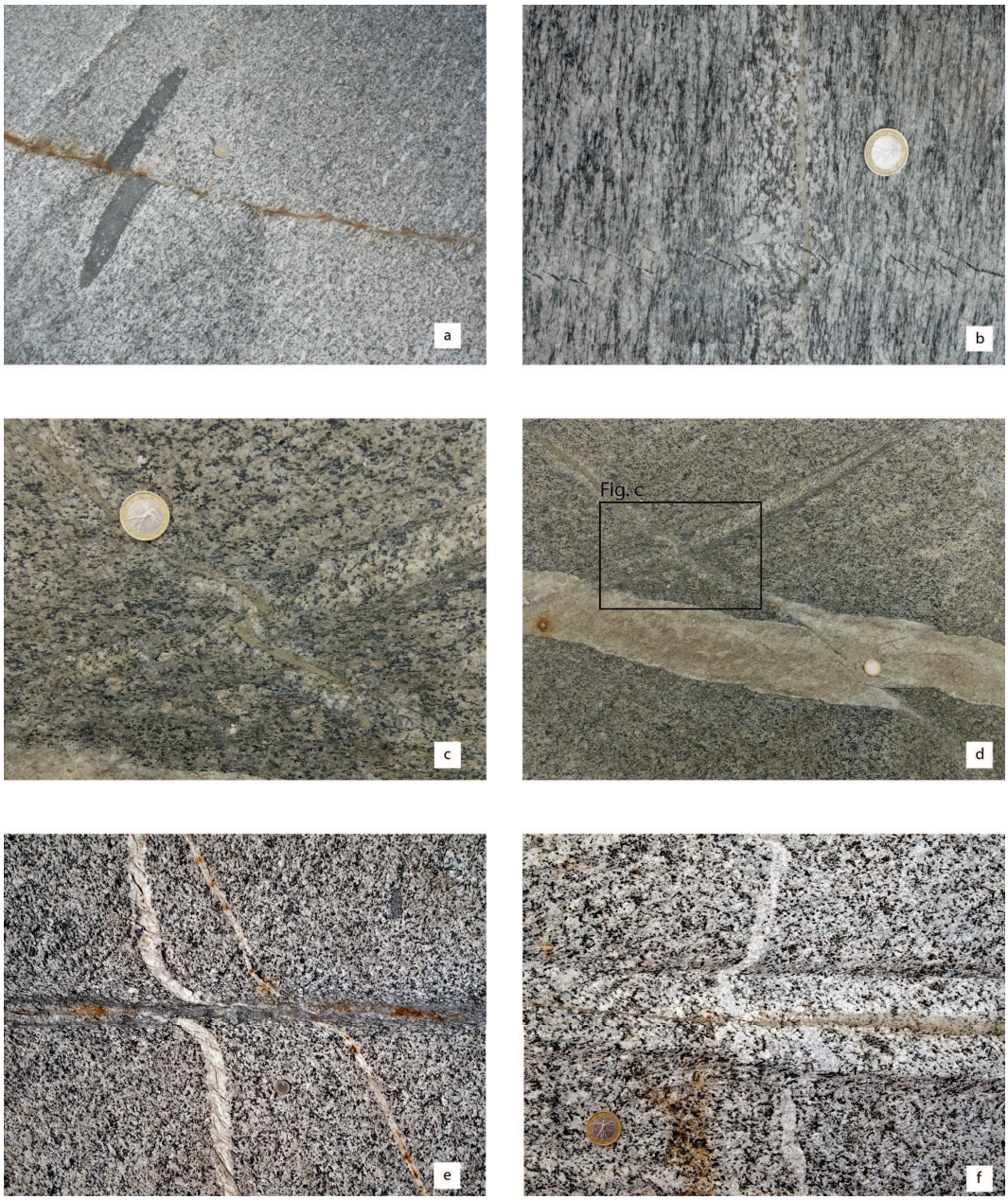

Figure 13: Examples of marker with opposite sense of shear. ***(a)*** *Joint that offsets sinistrally an MME; the sigmoidal foliation and dragging of the offset marker are dextral (Berlinerhutte area);* ***(b)*** *Even at high grade of deformation, the rock interested by the alteration halo of ep-grt veins are preserved from the deformation. An en-echelon array of chl-qtz vein crosscuts the ductile fabric (Moosboden area);* ***(c)*** *Magnification of fig. (d); the cerntal vein show a dextral offset of another eidote vein, but the weak alpine foliation is sinistral;* ***(d)*** *the previously displaced epidote vein of figure (c) shows a weak homogeneous dextral foliation along the central vein but the aplitic dikes is sinistrally displaced;* ***(e)*** *dragging of an aplite dyke along an epidote vein without alteration halos;to obtain this geometry the aplite dyke should have been offset dextrally and then dragged toward left by the alpine foliation;* ***(f)*** *central offset opposite to the alpine foliation shear sense.*

1.4 Conclusion

In the southwestern tauern window, the alpine deformation developed under a transpressive constant stress field oriented for the whole tectonic history ca. N-S. Under this stress field, deformation partitioned in a "fractal" way, i.e. scale independently, from the kilometre to the meter scale.

A first event of ductile deformation under amphibolite facies conditions localized on compositional and structural precursors at all scale partitioning the simple shear into discrete shear zones both at the kilometer and outcrop scale.

Brittle event developed under subgreenschist facies conditions with the development of cojugate set of en-echelon extensional (sigmoidal tension gashes) and shear fractures (faults) with strike-slip kinematics.

Veins, alteration halos and fracture geometries are the witnesses of the hydrous conditions under which deformation developed during both the ductile and brittle stage. Moreover, they indicate that the granitoids of the Zentralgneis were very weak, i.e. they could bear small differential stresses.

The patttern of ductile deformation fabric of the region highlight the strain partitioning at the regional scale that occurred during the collision. Two major simple shear zones (the Greiner and the Ahrntal) bound a multikilometric low-strain pure shear domain in the easternmost portion (the Zillertal Gneiss Core). In the western part strain is more homogeneously distributed and led to the development of a pervasive lineated fabric. The region as a whole can be classified as a pure constrictional transpression zone (*Fossen & Tikoff*, 1998) in which lengthening dominates (*Tikoff et al.,* 1999). The overall kinematics of the zone is not well defined, but according to *Pennacchioni & Mancktelow* (2007), a general dextral shearing should characterize the whole area.

Analysis of structural data from original fieldwork and available literature have demonstrated the coexistence in this zone of strike-slip zones, folds and lineated fabric compatible with the convergence and lateral escape tectonics. No other structures related to the other orogen building processes (thrusting and

exhumation) have been observed. Remnants of thrust tectonics due to nappe stacking may be confined to the thrust surface between cover and basement units, otherwise it should have been overprinted by the dominant strike-slip movements caused by the lateral escape tectonics during the peak metamorphism and retrograde path. Structures due to the Brenner-related exhumation are not observed. Hence, the partitioning in strain intensity over the region is not associated with a partitioning of components of coeval thrusting, lateral escape and detachment in no stage of deformation.

Ductile deformation could localize only in the presence of brittle and compositional precursors. In such situation, the viscosity contrast across these heterogeneities controlled the geometry and shape of the shear zones. Weaker rocks usually accommodate deformation in their interior through homogeneous shear zones, whereas viscous lithologies usually develop sigmoidal heterogeneous continuous either singular or paired shear zones. In addition, shear zones do not extend over the length of the former precursor, and linkage between nearby structures is usually achieved by diffuse deformation of the host rock (foliated domains). High temperature fracturing and veining exploited by the ongoing deformation are the demonstration that ductile strain needs structural and compositional heterogeneities to nucleate and to make shear zone nucleate.

Deformation history recorded by an exploited heterogeneity can be polyphasic, as it has been demonstrated by paired shear zones developed on epidote-garnet veins. A former deformation phase, maybe related to the Variscan pluton emplacement and cooling, has been overprinted by the recent Alpine amphibolite facies deformation.

Chapter 2

Fluid-rock interaction – Episyenites

The history of fluid – rock interaction in the southwestern Tauern Window is already well documented. From peak metamorphic conditions backward, fluid has always played an important role in controlling the evolution of deformation through metasomatism: Garbenschiefers (*Steffen et al.*, 2001) and aluminous schists (*Selverstone et al.,* 1991; *Barnes et al.,* 2004) outcropping along the northern margin of the ZGC are two outstanding examples. At the same time, metamorphic devolatilization reactions caused metasomatims of the host rock and veining inside the Gneiss Core, bringing to the formation of the already described quartz-calcite-biotite-plagioclase veins (*Cesare et al.,* 2001). During the exhumation, along with brittle deformation, fluids carried on their influential role controlling the development of faults and en-echelon tension gashes under subgreenschist facies condition (*Axen et al.,* 1995). The last event of fluid – rock interaction recorded in the Zentralgneis unit is the episyenitization of granitoids, that is reported for the first time in this work.

Episyenites are not so widespread in the Alps. The first vague report on episyenites in the Alpine belt is that of *Cathelineau* (1986) for the Mont Blanc episyenites, fully unfolded by later studies of *Rossi et al.* (2005). For the Eastern Alps there is a unique record of episyenite from the Alpeinerscharte Molibdenum vein-type deposits (*Melcher et al.*,1996). The Alpeinerscharte deposit is located just few kilometers north of our studied area, in the Tux Gneiss core. These two findings have formed under different conditions and timing: Mont Blanc episyenites formed during alpine deformation as proved by their strict relationship with veins and shear zones of alpine age (*Rossi et al.,* 2005); the Alpeinerscharte episyenites formed probably soon later than the Moybdenum veins during a post-orogenic intrusive stage in paleozoic times (*Melcher et al.*,1996). Even though

reported under different names, rocks similar to those described by *Rossi* are usually found inside all granitoid and gneiss cores exposed in the Alps associated to the so called Alpine-type veins that are also an essential element of the tectonic evolution of the orogen (data reported in this work; *Axen et al.*, 1995). These veins have been exploited by several generation of Alpine mineral collectors because of their capability to give enormous and wonderful crystals of quartz, albite, adularia, etc. Indeed, vein paragenesis is made of quartz + pericline (albite) + adularia (k-feldspar) + calcite ± sphene ± apatite (and occasionally sulfide minerals).

2.1 Episyenites in the Mesule area

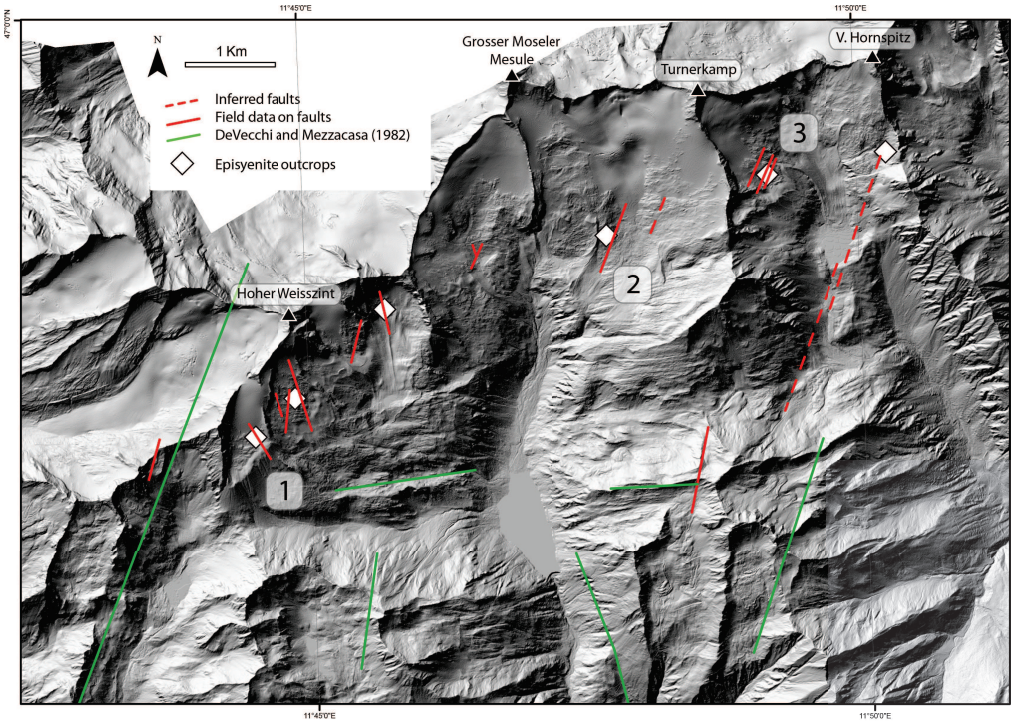

Figure 1: Regional distribution of faults and episyenite outcrops (data from DeVecchi & Baggio, 1982).Z

In this section we present the result of field and laboratory characterizations of host rock, episyenites and cataclasites from the Moosboden – Mesule area. The first objective is to define the field relationship between episyenite and brittle structures/rock fabric, and secondly the mineralogical and textural changes due to

different processes (events of episyenitization and cataclasis).Episyenites of the Mesule area

In the investigated area episyenites crop out in different locations inside the Zentralgneis unit always in strict correlation with faults or fractures systems (Fig. 2.1.1). Outcrops of episyenites are found in: (1) de-glaciated outcrops below the Gross Moseler close to the Mesule fault system (as it is also reported in *Pennacchioni & Mancktelow,* 2013); (2) under the Weisszint peak, (3) in the glacial cirque between Turnerkamp and V. Horsnspitz, at the Moosboden basin just below the Trattenbachkees (3.a) and at the Äußere Grüne Plate (3.b). Most of the outcrops are located between 2700 and 2800 m a.s.l.. Detailed mapping of locality (3.a) is reported in Fig.s 2.2.2 and 2.2.3. Most of the analysed sample comes from the Moosboden outcrop (3.a).

2.2 Detailed mapping of Moosboden episyenite

One of the Moosboden episyenites has been mapped in high resolution in order to reveal field relationship between faults and alteration halos. Results can be summarized as follows:

- Brittle structures are usually made of single meter-long en-echelon strike-slip segments; contractional jogs usually develops between overlapping portion of nearby segments and they are characterized by pervasive antithetic fracturation; observed structures have small horizontal displacements in the order of tens of centimetre to half a meter in a few cases;
- Episyenites are always found in strict correlation to faults or fracture system; not all faults are decorated with episyenites and, when present, they characterize only parts of the entire structure (Fig. 2.2.3);
- Fracture often defines the limit of the alteration halo; the outcrops-scale geometry of episyenites is governed by the spatial arrangement of fractures and faults (e.g. “en-echelon-like episyenites”, figure 2.2.1a).

Fractures commonly bound the alteration acting as restraining walls, but in most cases they work as the central pathway for fluid with the alteration that develops on both sides of the cleft;

- Episyenitic alteration completely overprints cataclasites and there are no occurrence of episyenites involved in cataclasis;
- There are no clear relationship between faultmaturity and episyenitic alteration intensity: episyenites can develop from knife-sharp fractures with no strike-slip displacement as it can be found along with evolved structures with tens of meter of throw and meter-wide cataclastic horizons; sinistral and dextral structures are equally interested by episyenitization;
- Fracture density have not any direct control on alteration development: highly-fractured contractional jogs often do not present any kind of alteration, in contrast with single knife-sharp fractures that are often highlighted by highly porous halos;
- Spatial development of episyenites are completely insensitive to compositional discontinuities when the alteration spreads entirely inside granitoid rocks, such as aplitic and pegmatitic dikes. However, quartz-poor mafic lithologies, such as lamprophyres and phyllonites, act as restraint to fluid diffusion;
- Foliation and textural anisotropies of the host rock influence in different ways the development of alteration: (i) bulk foliation does not shows any control on episyenite evolution and it is completely overprinted; (ii) thick mylonitic zones limit the spreading of alteration, being usually made of mafic phases (biotite-phyllonites); (iii) thin shear zones in a few cases bounds episyenites, i.e. they limit the lateral development; (iv) episyenites form a sort of lateral apophyses along paired shear zones developed after epidote-garnet veins;

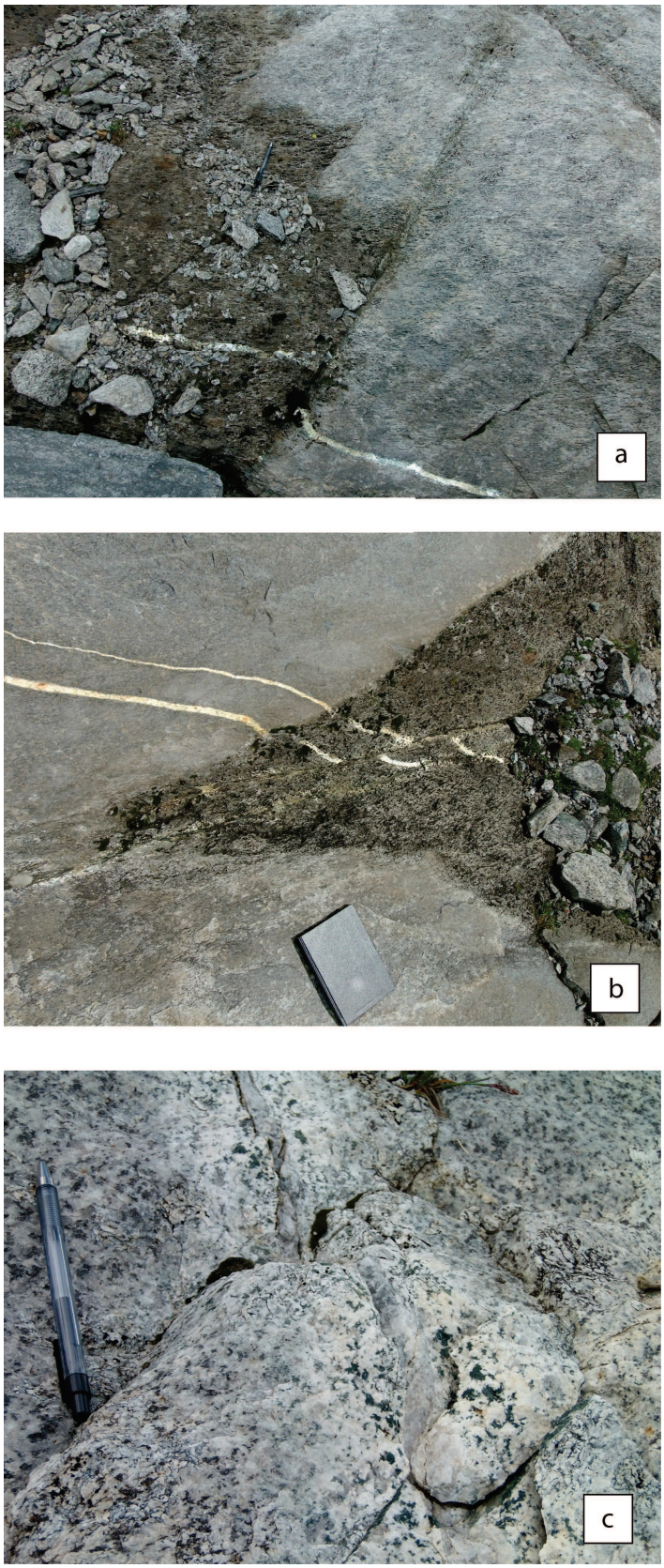

Figure 2: ***(a)*** *"en-echelon" episyenite bounded by en-echelon shear fractures with a variable offset (from 0 to 9 cm where the aplite dyke is cut) – locality[A] of the following detailed map;* ***(b)*** *episyenite apophyses developed along a paired shear zones (epidote-vein) – locality [B];* ***(c)*** *Alpine-type vein halo developed along the selvages of a quartz-chlorite vein.*

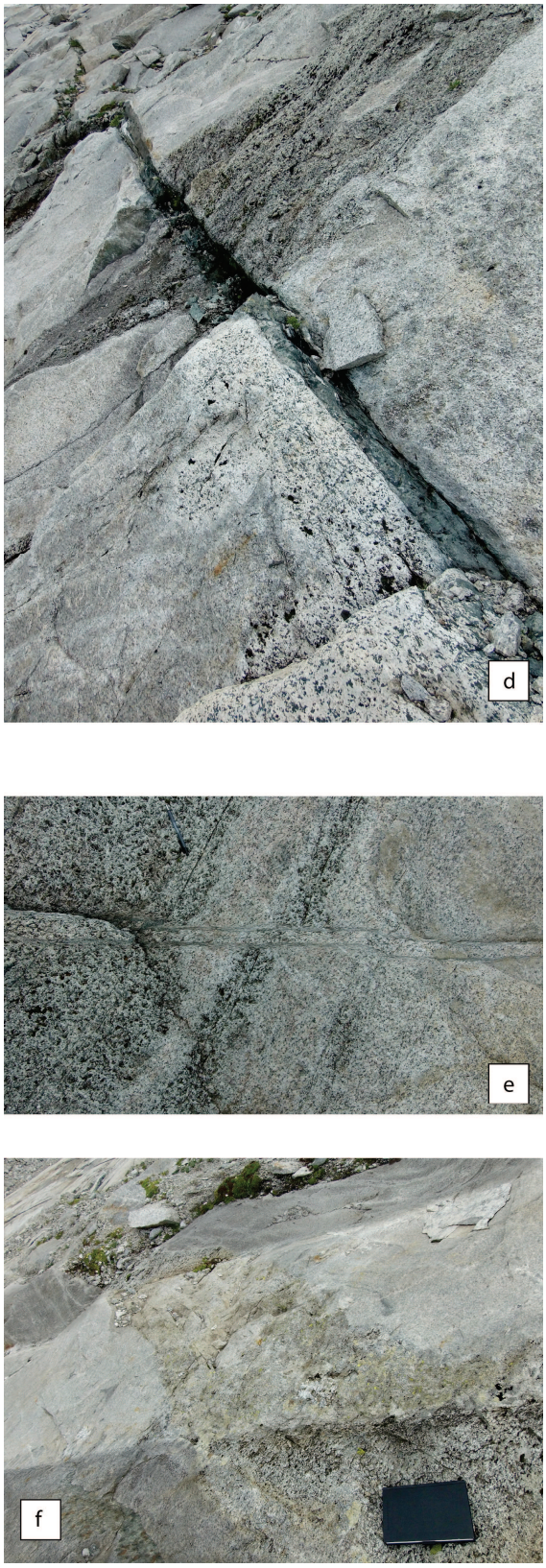

Figure 2.2.1 (cont.): ***(d)*** *crosscutting relationship between episyenites and Alpine-type vein halo: the former follows a brittle structure (oriented W-NE in the photo), the latter follows a mylonitic lamprophyre spreading from it – locality [D];* ***(e)*** *three subparallel dextral faults crosscut a paired shear zone and are differently touched by the episyenite formation – locality [E];* ***(f)*** *aplitic dyke (with dextral alpine foliation) is crosscut by a late fault and overprinted by episyenite – locality [F].*

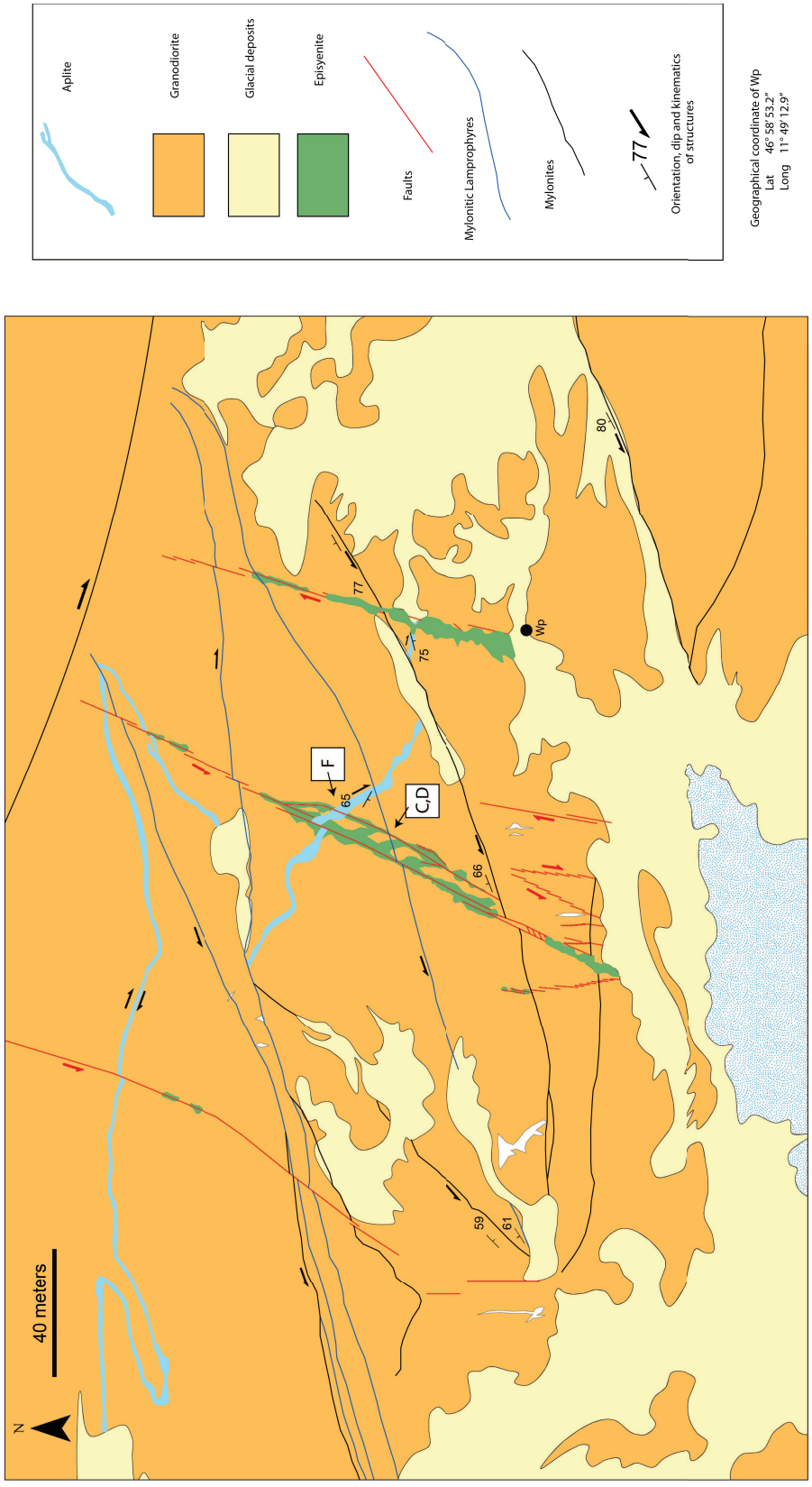

Figure 3: Geological map of the Moosboden main outcrop of episyenite [3].

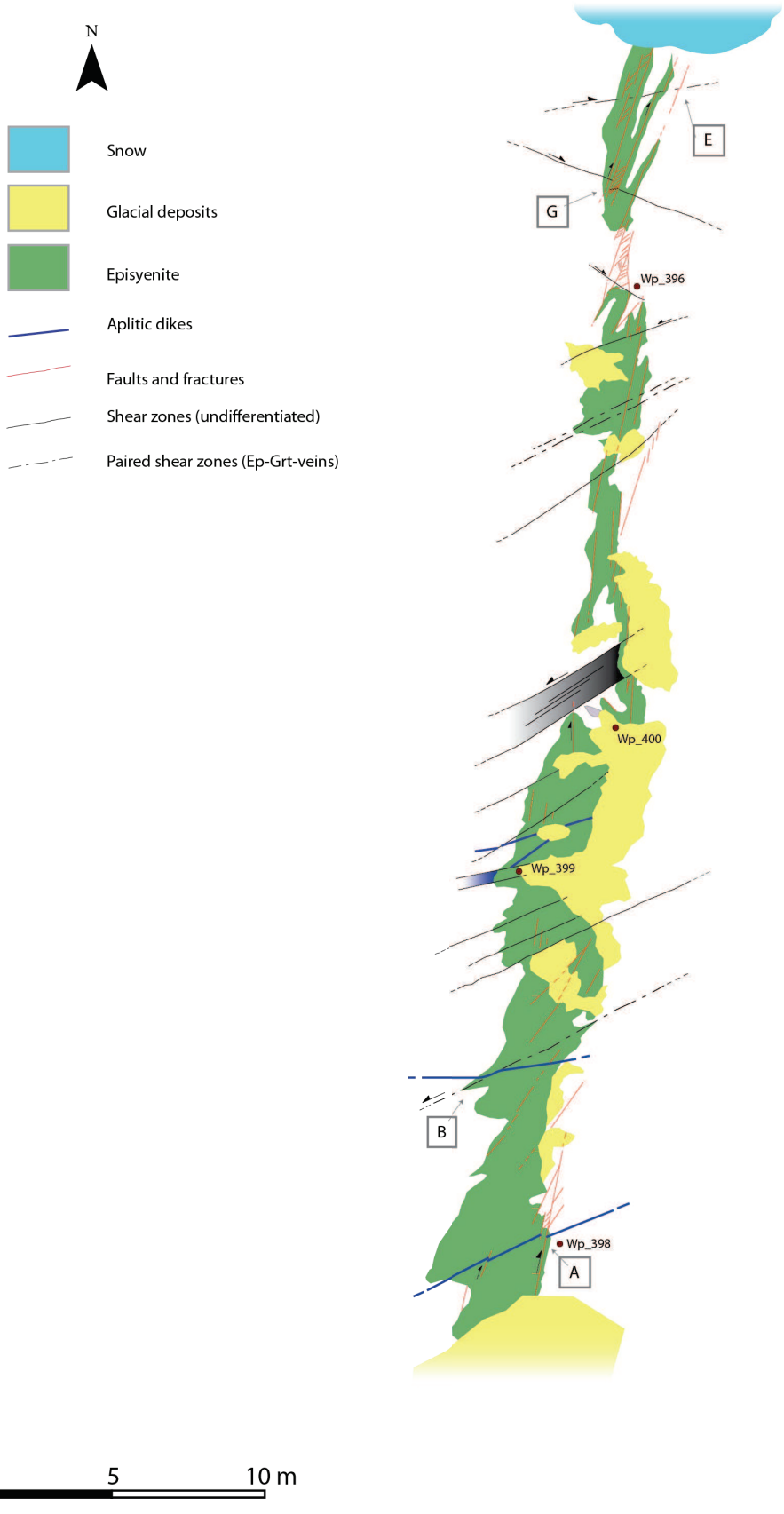

Figure 4: Sketch representing the observed relationships and geometrical features of episyenites and faults in the eastern structure of the Moosboden outcrop.

2.2.1 Field characters of Alpine-type vein halos

Episyenites described above are separated from Alpine-type vein halos for several characteristics:

- their occurrence along quartz-chlorite-epidote-albite vein selvages as lighter (and greenish) dm-thick halos; there is only one outcrop where these halos depart from vein selvages and interest a wider volume of rock (Fig. 2.2.1d). This morphology suggest a forming process called "lateral secretion", already documented in other ore deposits and veins (*Wagner et al.* 2000; Fig. 2.2.1c), in which fluids hosted in the wallrock dissolve mineral phases that are redeposited in a nearby tensile crack;
- Veins are Mode-I and III syntectonic fractures, hence also the alteration is coeval with the brittle deformation event (e.g. sigmoidal tension gashes).
- Commonly, this alteration type highlight contractional jogs between en-echelon fault segments, i.e. where fracture density is higher;
- Episyenites frequently crosscut Apline-type halos in region nearby to faults (Fig. 2.2.1d);
- Biotite-rich lithologies (such as lamprophyres and biotite-phyllonites) are widely chloritized and usually act as fluid pathways (Fig. 2.2.1d).
- Vugs left by quartz dissolution are completely filled with green compact chlorite (Fig. 2.2.1c);

2.3 Petrography and mineral chemistry – EMP analysis

Sig. Raul Carampin is gratefully acknowledged
for their invaluable help in microprobe
setting and data acquisition.

Episyenitization interests more than one single "granitoid facies" of the Zentralgneise suite: metagranitoids, aplites and lamprophyres are usually the most common lithotypes involved in the alteration process. Here, I briefly describe the petrographical features and mineral composition of the different "host rocks" and related episyenites. In the area where we have sampled episyenites crop out mainly granitoids and aplites belonging to a former Calk-alkaline I-type magmatic series of Late Carboniferous age (*Eichhorn*, 2000; *Cesare,* 2002) that has been heterogeneously involved in Alpine deformation.

Analysis has been performed with a Cameca SX50 Microprobe at the Department of Geoscience, Univ. of Padova. Each "class" of mineral phases detected during petrographical analysis, such as "General silicates", "Phyllosilicates", "Carbonates" and "Zeolites", has been analysed using dedicated microprobe settings in order to avoid problems due to sample heating and elements vaporization (Alkalies, OH^- and CO_3^{2-}).

Mineral compositions are reported in Appendix A.

2.3.1 Mineralogy and microstructures

2.3.1.a Mineralogy and Microstructures of Metagranitoids

Representative samples are 12-104F, 12-105B. They are respectively a weakly foliated metatonalite and a mylonitic granodiorite. The metatonalite charaterized by a medium to coarse-granied weak gneissic structure, defined by phyllosilicates. Instead, the mylonitic fabric of metagranodiorite is defined by a fine-grained Bt-

Ms foliation. Principal phases are quartz, plagioclase and K-feldspar, and biotite. Secondary phases are muscovite, garnet and epidote (often in association with minor amount of magmatic allanite). Accessory phases are Rutile, Zircon and Apatite.

Quartz shows weak plastic deformation, with ondulose extinction and elongated subgrains that overprint a microsctructure due to GBM. Magmatic plagioclase has an oligoclasic composition (Ab_{85}), but is often widely destabilized into fine-grained Ms-Ep aggregates hosted in a coarser matrix of polygonalized Ab (saussurite alteration). K-feldspar (Or_{91}-Ab_8) show perthite structure with Ab exsolution lamellae often also destabilized into fine grained aggregates of unknown phases. Siderophyllitic Biotite [$(K_{1,798}\ Na_{0,018}\ Ca_{0,009})\ (Mg_{1,249}\ Fe^{2+}{}_{3,487}\ Al^{VI}{}_{0,564}\ Mn_{0,063})\ (Al^{IV}{}_{2,491}\ Si_{5,509}\ O_{20})\ (OH,F)_4$] has decussate texture and, where Alpine deformation has been more intense, defines the main foliation. Minor amounts of phengitic [$(K_{1,887}\ Na_{0,043})\ (Al^{VI}{}_{3,132}\ Fe^{2+}{}_{0,599}\ Mg_{0,348}\ Mn_{0,006})\ (Al^{IV}{}_{1,431}\ Si_{6,596}\ O_{20})\ (OH,F)_4$] is also present.

2.3.1.b Mineralogy of Aplite

Aplites (sample 12-104E) form centimetre to meter-wide fine-grained dikes inside the Zentralgneis granitoids. Its petrogenesis and time of emplecement is similar to that of the Zentralgneise granodiorite. Isiomorphic feldspars form the aplitic framework in which allotriomorphic quartz has crystallized.Principal phases are Plagioclase and K-feldspar, Quartz. Minor amount of Muscovite and chloritized Biotite are also present.

Quartz shows little or no sign of deformation. Euhedral to subhedral K-Feldspars (Or_{90} – Ab_9) shows either perthitic structure and “tarntan” twinning typical of Microcline. Quartz and Feldspars (Albite?) usually form Myrmekite intergrowths that locally substitute K-Feldspar. Plagioclase (Oligoclase – Ab_{85}) exhibit a poikilitic texture defined by small inclusions of Muscovite and Epidote. Muscovite [$(K_{1,864}\ Na_{0,042})\ (Al^{VI}{}_{3,193}\ Fe^{2+}{}_{0,466}\ Mg_{0,360})\ (Al^{IV}{}_{1,407}\ Si_{6,593}\ O_{20})\ (OH,F)_4$]

are slightly enriched in Al and fall within the Phenigitic composition field.

2.3.1.c Mineralogy of “Alpine-type vein halo”

Reference sample: 12-104A. Principal phases are: Plagioclase, Chlorite and Muscovite. Other secondary but relevant phases are: Titanite, Albite, Apatite, Zircon. Minor amount of Calcite, Epidote and Allanite are also found. Quartz is completely absent.

Chlorite (Ripidolite; $(K_{0,002}\ Na_{0,006}\ Ca_{0,008})\ (Al^{VI}_{2,734}\ Fe^{2+}_{6,406}\ Mg_{2,751}\ Mn_{0,056})\ (Al^{IV}_{2,746}\ Si_{5,254}\ O_{20})\ (OH)_8$; Fig. 2.3.1) has a feathery aspect and grows pseudomorphing Biotite, parallel to the former cleavage planes. Chlorite occupies also vugs left by the dissolution of Quartz and, inside them, crystal aggregates have lower aspect ratio (rounded shape, Fig. 2.3.3d,e,f). Both forms have the same grey-greenish pleochroism and grey anomalous interference colours.

Euhedral Muscovite1 grows along vug's walls and shows heterogeneous interference colours due to slightly variation in the content of Al^{IV}, Fe^{2+} and Mg. Muscovite2 has phengitic composition $[(K_{1,919}\ Na_{0,013})\ (Al^{VI}_{3,421}\ Fe^{2+}_{0,400}\ Mg_{0,255})\ (Al^{IV}_{1,543}\ Si_{6,457}\ O_{20})\ (OH,F)_4]$ and forms fan-like platy aggregates found together with Chlorite and Titanite (Fig. 2.3.3f). Idiomorphic apatites are not so rare.

Plagioclase_Core (Ab_{77}) shows a rim enriched in Albite component (Plagioclase_Rim, Ab_{85}) that grows euhedrally against Chlorite-filled vugs. In some cases Chlorite1 seems to develop at the expense of Plagioclase_Rim (Fig. 2.3.3e).

Albite + Titanite + Ilmenite + Muscovite2 ± Apatite ± Calcite are secondary phases often associated with Chlorite. Ipidiomorphic inclusion-free Albite forms spectactular aggregates surrounded by Chlorite in vugs (Fig. 2.3.3d). Ilmenite contains small amount of Mn $(Fe^{2+}_{0,94}\ Mn_{0,05})\ (Ti_{0,992}\ Fe^{3+}_{0,016})O_3$.

2.3.1.d Mineralogy of cataclasites

In general, cataclasite mineralogy depends on protolith mineralogy and

composition. However the stable paragenesis is given by quartz ± albite ± muscovite ± epidote ± chlorite. At least 70% of the neo-formation paragenesis volume is made of quartz, that shows different morphologies: (i) fine grained quartz along principal slip planes; (ii) thin ribbons of cryptocrystalline quartz, white mica and epidote, coating clasts of protolith and cataclasite, then involved in cataclasis; (iii) euhedral undeformed crystals filling veins and open spaces. Chlorite usually overgrows mafic phases such as biotite of protolith clasts. No particular flow structures, secondary planes of Riedel structures are observed.

2.3.2 Mineralogy of Episyenites

2.3.2.a Aplite episyenites

Sample 12-104D.

The former magmatic feldspar framework is mainly preserved; quartz is completely absent Main mineralogical changes are linked to Plagioclase and K-Feldspar alteration and reprecipitation. Plagioclase1 is widely transformed into saussuritic, cloudy assemblage upon which grows epitaxially Plagioclase2 (Ab_{99}). The boundary between these two feldspars is very straight and sharp (a few μm wide) and it is often highlighted by dark solid or fluid inclusions (Fig. 2.3.2d,e). The epitaxial growth is demonstrated by the prosecution of former albite twinning of Plagioclase1 into Plagioclase2 (Fig. 2.3.2f).

Kfs2–Adularia (Ab_2 – Or_{98}) grows along vug walls assuming particular pyramidal shapes already documented in episyenites by *Cathelineau* (1986; his figure Plate(1)-6 and Fig. 2.3.2d). Kfs1 and Adularia, when found in contact, are usually distinguished according to different crystallographic orientation and different unmixing/twinning structures.

The second generation of feldspars grows preferentially upon their respective magmatic phase (Plg2 upon Plg1, Adularia upon Microcline/Sanidine).

A distinctive characteristic of episyenites developed from Aplites is the presence

of Ca-K Zeolites as pore-filling phases, such as sheaf-like fibrous Scolecite ($Na_{0,023}$ $Ca_{0,959}$ $Al_{1,944}$ $Si_{3,055}$ $O_{10)}$ and prismatic K-Heulandite [($Ca_{1,598}$ $K_{0,510}$ $Na_{0,024}$) Al_3 ($Al_{1,358}$ $Si_{0,789}$) Si_{13} O_{36} · $12H_2O$] (Fig. 2.3.2e).

2.3.2.b Granodiorite episyenites

Samples 12-104B/C-Epi/H/I/J, 12-105A.

Episyenites preserves mainly the magmatic Feldspar framework of the host rock; Quartz and Phyllosilicates are completely removed and/or altered. Principal phases are: Oligoclase and Albite (Plagioclase1 and Plageoclase2), Chlorite, Calcite and Muscovite. K-Feldspar2 + Apatite + Anatase + Hematite + Zircon + Allanite + Granet are the typical accessory phases found in episyenites. The dissolution of Quartz had left a pervasive porosity that is commonly occupied by Calcite and Albite. However, weathered samples have no vug-filling phases showing the porosity in its totality.

As we have already seen in Aplitic episyenites, Plagioclase2 (Ab_{98}) grows epitaxially upon Plagioclase1 (Ab_{85}). Frequently, Plagioclase2 seals microfractures and veins. Both (magmatic) plagioclase and K-feldspar have an earthy aspect very similar to that developed after kaolinitization or illitization. .

Chlorite is present under different forms:

1. Green – greyish chlorite with grey interference colours, pseudomorph after biotite (A – chlorite in the classification diagram, Fig. 2.3.3d,e,f);
2. Brown – dark yellow to deep red chlorite, high relief, rough aspect; usually found together with and substituting green Chlorite; it forms fine grained massive aggregates in association with K-Feldspar2 + Anatase + Apatite + Calcite + Hematite; sometimes it displays a rounded to hexagonal habit (I-B-D chlorite, Fig. 2.3.2b, Fig. 2.3.3a,b);

3. Green to brown Vermicular Chlorite in fine aggregates made of discernible single "worms" in association with Calcite + Hematite + Anatase (Fig. 2.3.2c);

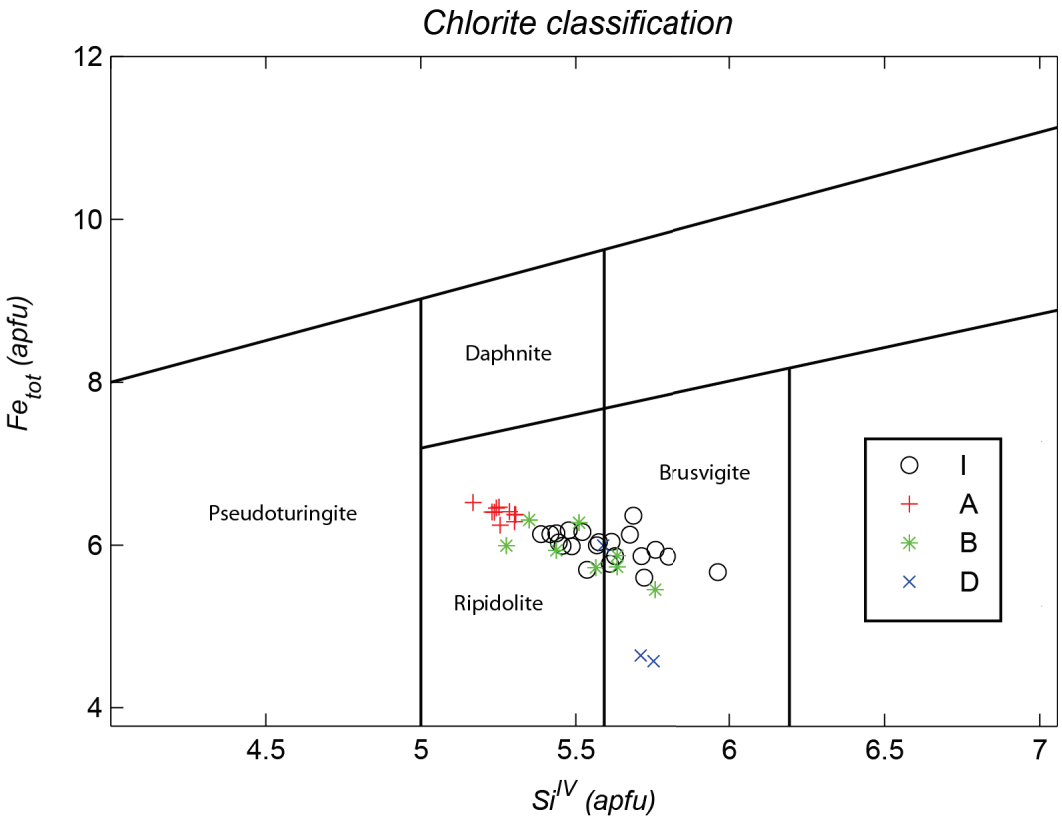

Figure 5: Chlorite classification diagram.

From the chemical point of view, there is no clear correlation between morphology and composition. All Chlorite types has Fe/(Fe+Mg) ratio ranging from ca. 0,60 to 0,70. Their content of Fe_{tot} and Si^{IV} classifies them as Ripidolites or Brunsvigites. Only two analysis of Brown Vermicular Chlorite shows a composition that fall within the field of Pycnochlorite (chlorites belonging to the aplite-episyenite).

Powder diffraction analysis has revealed that what we have classified throught petrography and chemical analysis as vermicular chlorite is actually an authigenic clay mineral made of ordered interlayers of Chlorite and Clays (Chlorite-

Vermiculite; F. Zorzi personal communication).

K-Feldspar2 (Or_{97} Ab_2) is intimally associated with Brown Chlorite, and it is present in most of the collected samples (Fig.2.3.3a). It shows no zonations or exsolution textures. However, in sample 12-104H, along with this type of Chlorite we can see fine aggregates of Sericite or Illite (Fig. 2.3.3b).

Gem-like small (up to 400μm) tabular crystals of Anatase and acicular Apatite usually decorate brown chlorite aggregates.

Hematite ($Fe^{3+}_{1,877}$ $Ti_{0,060}$ $Fe^{2+}_{0,055}$)O_3 grows in thin sheets parallel to the former Biotite cleavage planes or, when found inside geodes, as rose-like aggregates.

Allanite is quite stable inside this assemblage, but the outer magmatic rim of epidote has been completely altered and substituted by secondary phases such as Calcite and Albite.

Calcite ($Ca_{0,996}$ $Fe^{2+}_{0,001}$ $Mn_{0,003}$)CO_3 appears either as vug-filling phase and platy thin crystals that often include Vermicular Chlorite, Anatase and Albite. In most cases Calcite is pervasively twinned. There are no difference in composition between morphological types, as has been highlighted by cathodoluminescence microscopy.

2.3.2.c Episyenite from Cataclasites

Cataclasite structure is completely preserved. Principal phases are: albite, (vermicular) chlorite and calcite; muscovite, hematite, anatase and zircons are found as secondary and accessory phases. Plagioclase of protolith clasts have a dull brown aspect due to the small inclusions of phyllosilicates probably as a consequence of kaolinitization. Albite forms fine aggregates of euhedral-subhedral crystals around protolith clasts and vug walls. Lamellar calcite often fills the remnant open space. Aggregates of vermicular chlorite, hematite, muscovite and anatase delineate the former fractures and slip planes. Calcite is decorated by tabular thick twins.

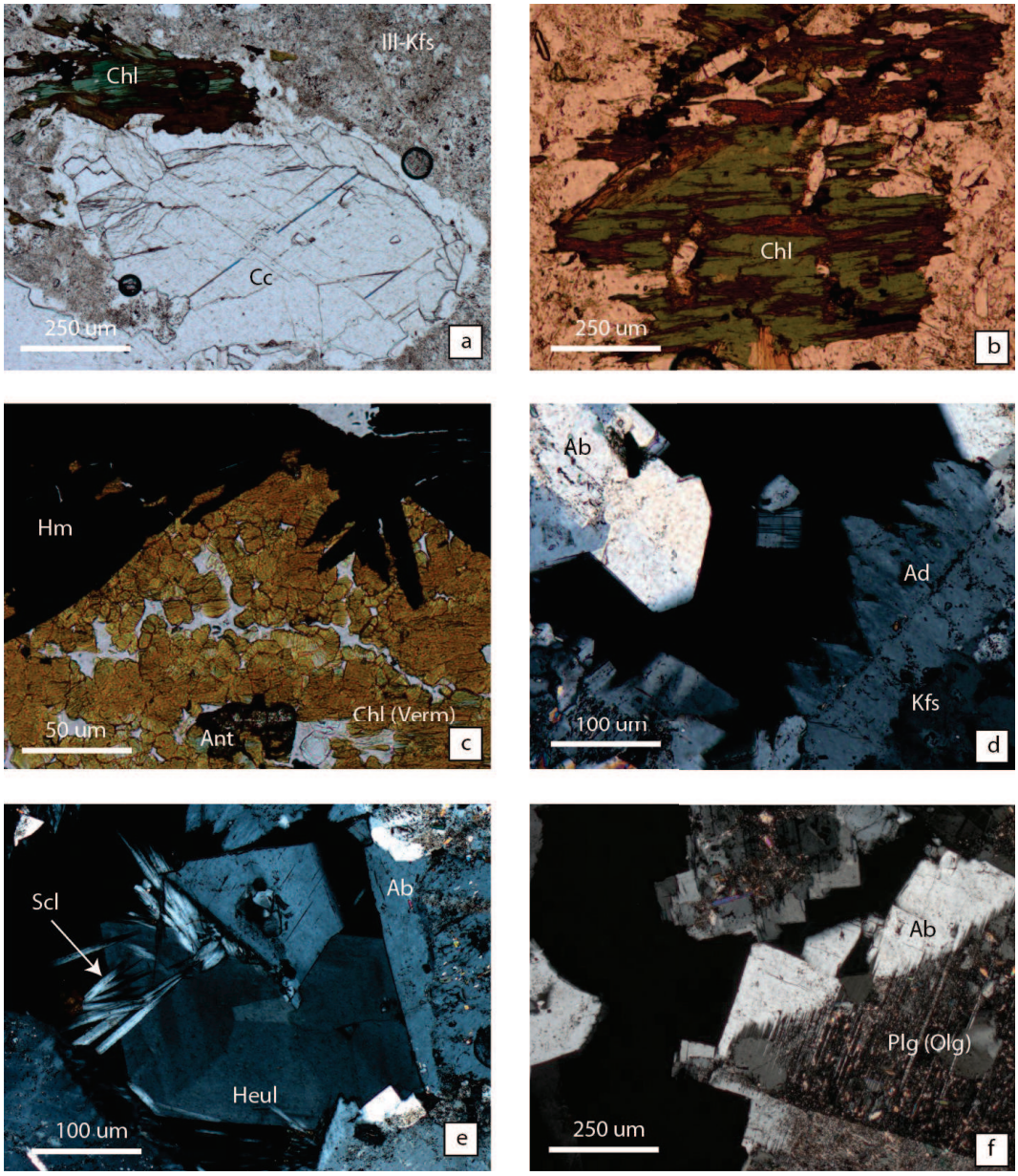

Figure 6: ***(a)*** *Pore filled with calcite (Cc) formed within illitized feldspar (Ill-Kfs).* ***(b)*** *Brown chlorite pseudomorphin green chlorite (in turn pseudomorphing magmatic biotite).* ***(c)*** *Rose of hematite surrounded by thin worms of Chlorite-Vermiculite interlayers; (Ant for Anatase).* ***(d)*** *Adularia (Ad) and Albite (Ab) growing on the former magmatic feldspar. Note the spiky aspect of Adularia.* ***(e)*** *Zeolites of Aplite: rayed Scolecite (Scl) and prismatic Heulandite growing inside a vug.* ***(f)*** *Epitaxial growth of the Plg2 (Ab) on the former magmatic plagioclase (Oligoclase) now completely illitized.*

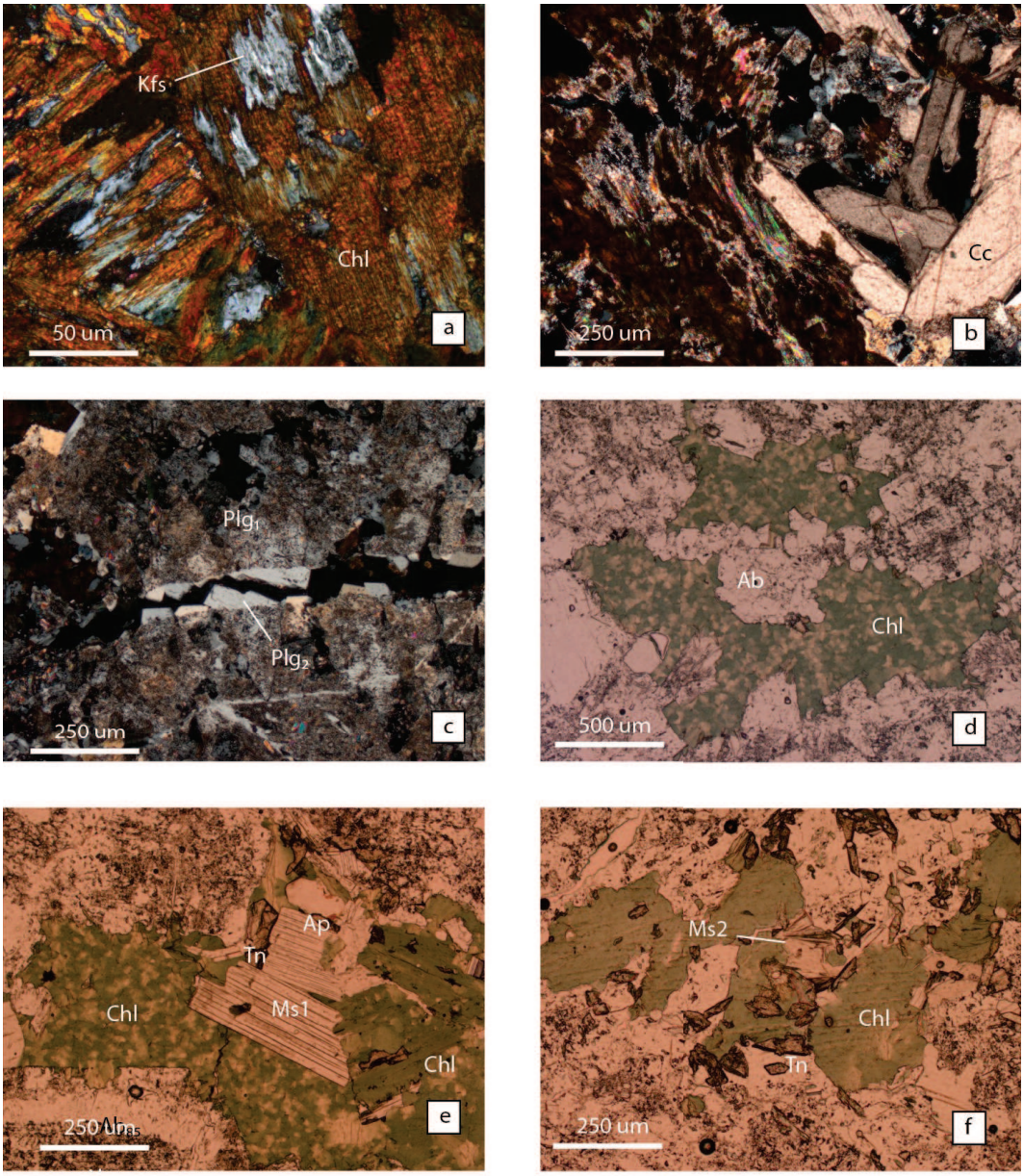

Figure 7: ***(a)*** *K-feldspar and Chlorite: assemblage found also during SEM investigation.* ***(b)*** *Platy calcite associtaed with chlorite and illite (pseudomorphing the former K-feldspar).* ***(c)*** *Fracture filled with Plg2 (Ab) developed inside Plg1 Completely altered.* ***(d)*** *Aggregate of hydrothermal Ab inside a chlorite-filled vug in Alpine-type halos.* ***(e)*** *Typical paragenesis of Alpine-type halo: feathery and orbicularchlorite, muscovite, titanite and apatite.* ***(f)*** *Thin fans of muscovite2 grows inside chlorite.*

2.3.3 – Chlorite geothermometry

The widespread occurrence of chlorite in episyenites has allowed to evaluate the conditions of episyenite formation through the application of several different chlorite geothermometers. Temperatures have been evaluated using the compositional geothermometers proposed by *Cathelineau & Nieva* (1985). Is

	T (°C)	St_dev	N#
I	325.4	23.5	21
B	337.3	25.7	8
D	311.1	13.6	3
A	379.4	6.9	10

Figure 8: calculated temperatures for chlorites analysed in samples 12-104I, 12-104B, 12-104D ans 12-104A according to Cathelineau and Nieva (1985).

worth mentioning that, the feasibility of these chlorite geothermometers are still under debate. However, some interesting result has been obtained. Chlorite form the Alpine-type vein halo yield temperatures of 370°C (± 6 °C, 10 measures). Instead, given the high compositional variability of chlorite from episyenite, temperatures span over a wide range (between 270°C and 350°C; average T: 329°C ±25°C; 33 measures). Geothermometers based on the oxigen isotope fractionation between quartz and chlorite yielded temperatures that highlight the possibility of overestimation compositional temepratures (320°C for the "Alpine-type chlorite"; Lacroix personal communication, *Lacroix et al.* 2013). Therefore, a slight overestimation is to be expected for compositional geothermometers.

Calcite geothermometers (*Rice*, 1977) have not been applied because of the absence of basilar prerequisites (dolomite-calcite coexistence). However, a gross temperature estimation based on calcite twins indicate a T of deformation above 170°C and below 250°C (*Ferrill et al.*2004).

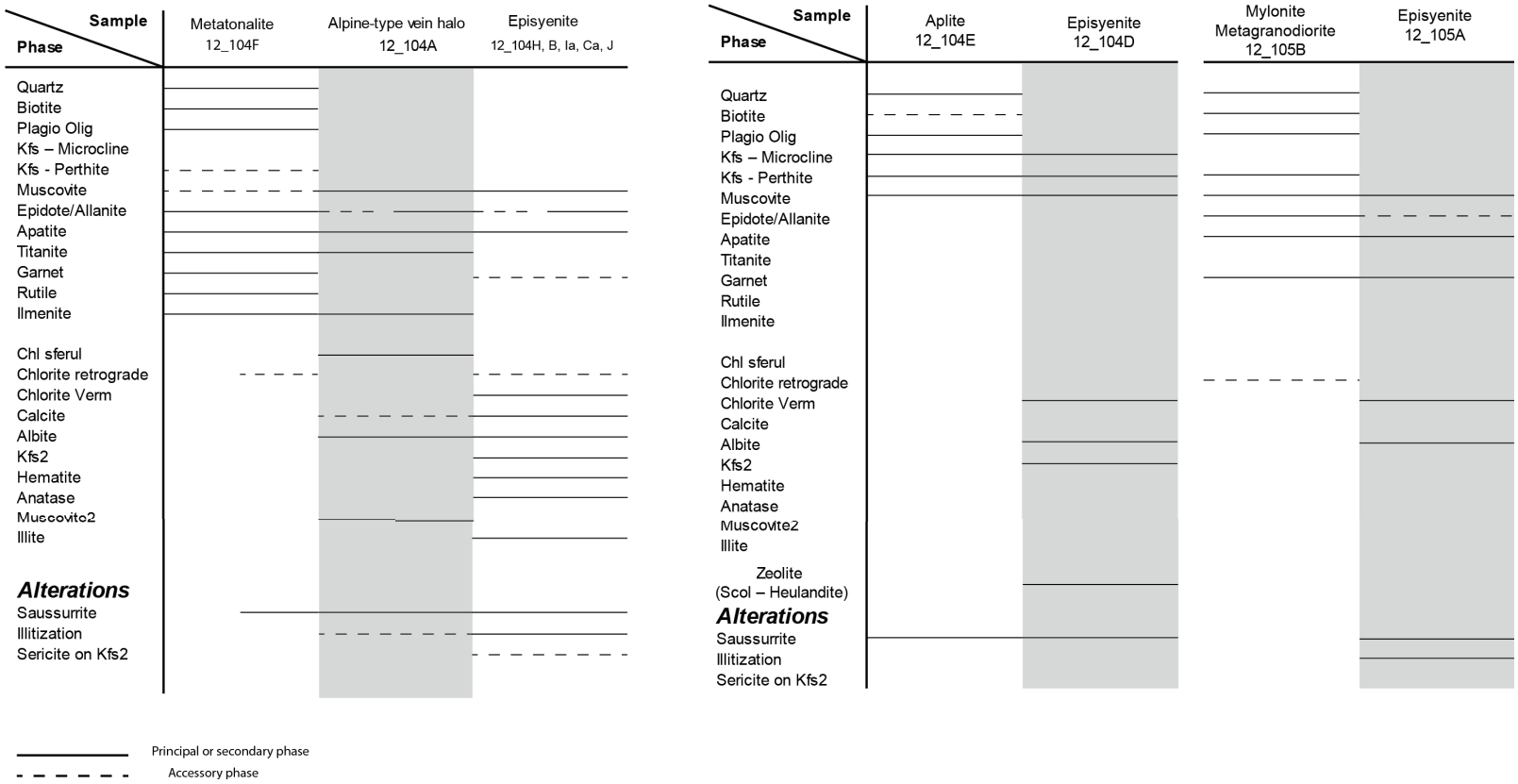

Figure 9: table showing summary of the petrographic investigations on episyenites, host rock and cataclasites.

2.3.4 Interpretation

During the retrograde path from peak metamorphic condition toward the surface, the Zentralgneise granitoids undergone to several episodes of fluid-rock interaction at different pressure and temperature. In our samples, the first alteration event that can be observed is the saussuritization of calcic plagioclase and chloritization of mafic minerals such as biotite and garnet. Resulting alteration paragenesis are usually made of Ab + Ms + Ep + Chl. These two type of retrograde alteration have been already reported to occur at conditions below the amphibolite facies, i.e. under greenschists facies. This process interests the whole rock volume.

According to the paragenesis shown by cataclasites, brittle faulting may have occurred under greenschists to subgreenschist facies conditions. This brittle event might have included several phases of dilatancy of the fault plane during the latest phases of slip, as it is witnessed by the occurrence of massive and microcrystalline quartz. The different morphologies could be due to different velocity of deposition of quartz and then to the dilatancy activity (that influence the stability of fluid).

A second type of alteration is the so called "Alpine-type vein halo", usually localized on decimetre-wide halo around vein selvages, and rarely as irregular pods unrelated to nearby veins.. The paragenesis is given by Quartz + Albite + Adularia + Chlorite, Secondary but peculiarphases, that occur in both fissures and halos, are sphene, muscovite and apatite. . Alteration halos n characterized by quartz absence. Plagioclase rims evidently formed during this second stage of alteration have a more albitic composition than that of the former magmatic plagioclase (Ab_{77} against Ab85). *Eggleton et al.* (1985) proposed a chloritization reaction for magmatic biotite that can be easily observed in our sections:

$$1\text{biotie} + 0.21\text{anortite} + 1.64H_2O + 1.46H^+ + 0.08O_2$$

$$\rightarrow$$

$$0.46\text{chlorite} + 0.11\text{sphene} + 0.1\text{epidote} + 0.56\text{muscovite} + 0.63\text{quartz} +$$

$$0.02\text{magnetite} + 1.46K^{+}$$

This reaction could account for both the partial albitization of plagioclase and for the complete substitution of biotite by chl-sph-ep-ms aggregates. Hence, three main processes has interested this phase: dequartzification, albitization and chloritization.

All the available literature on similar fissure paragenesis (*Wagner et al.,* 2000; *Weisenberger et al.,* 2011), alteration process (*Rossi et al.*, 2005) and mineralogical reaction involved (*Eggleton et al.,* 1985) suggest a temperature near to 340-400°C. Temperature evaluation based on several chlorite geotermometers (*Cathelineau & Nieva*, 1985; *Lacroix* 2013;) address for the same range of conditions (300-350°C).

Episyenites are the latest stage of alteration. Under the oprtical microscope, episyenitization shows itself through the partially or complete illitization of feldspars, the deposition of a second generation of feldspar and obviously through the complete removal of quartz. The peculiar feature of episyenites are, however, the occurrence of vermicular chlorite and platy calcite, both are indicated as proof of boiling condition of the fluid (*Nishimoto et al.,* 2014). Chlorite geothermometers show lower temperatures of formation for chlorite (and also calcite deformation): a lower temperature for fault-related episyenites are also confirmed by the stability of zeolites such as Scolecite and K-Heulandite in addition to the absence of muscovite and especially epidote.

2.4 Raman microspectroscopy

In order to quickly identify pore-filling mineral phases, samples 12-104H/I/J has been investigated using Raman spectroscopy. No special preparation of sample was needed.

Data acquisition has been performed during two sessions with a DXR Raman Microscope (Omnic Thermo Scientific) at the Department of Chemistry, University of Padova, controlled by Atlμs software.

Analytical conditions:

- Laser light: green 532 nm;
- Power: 10 mW;
- Exposure time: 45 s * 3 times;

A selected range of the obtained spectrum (from 100 to 1400 cm^{-1}) has been compared automatically by the Atlμs software with a mineral database (Rruff Project database, that can also be found online at http://rruff.info/) in order to identify the phase at which the spectrum belongs.

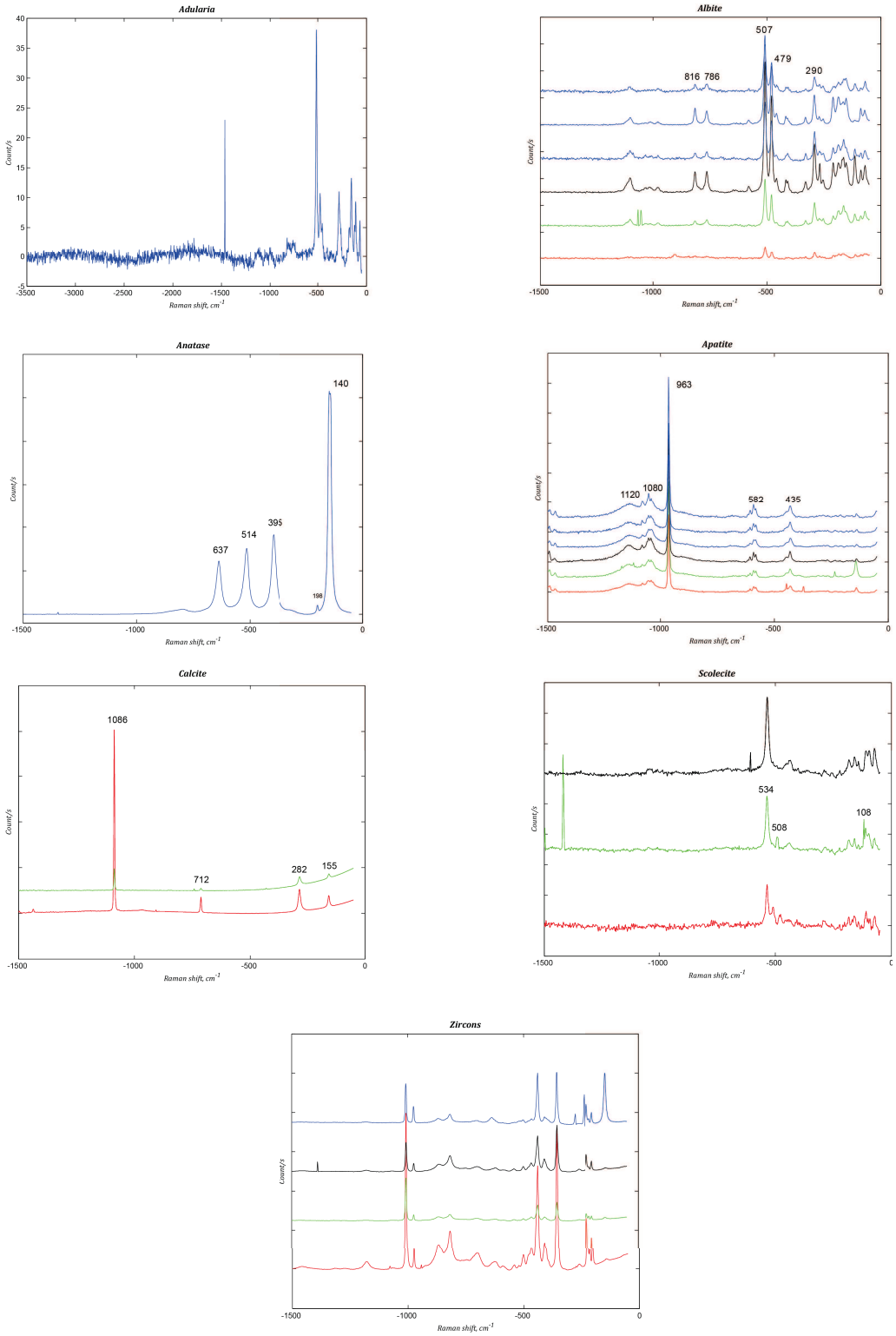

Figure 10: Raman shift diagrams of the investigated phases from samples 12-104H/I/J.

2.5 Bulk chemistry – XRF analysis

Data has been collected using a Phillips PW2400 XRF sequential WDS spectrometer at the Department of Geoscience, Univ. of Padova, equipped with a Rh tube (maximum released power 3 kW). Lost-On-Ignition has been measured before the XRF analysis, heating the sample in an oven at 860°C for 20 minutes and then to 980°C for 2 hours. FeO determination has been performed by titration (Permanganometry).

XRF data are reported in the respective table in Appendix A.

2.5.1.a Classification

From a first review of data it is possible to see the relative chemical changes due to various type of alteration on different rocks. *Cathelineau* (1986) report a useful diagram for episyenite classification according to their bulk chemistry. They are called Q_1-F_1 diagrams, where Q and F stand for:

$$Q_1 = Si/3 - K - Na;$$

$$F_1 = K - Na;$$

Elemental quantity are expressed as millications. Millication is a unit of measure used frequently by the French school, and it is calculated as follow:

$$Element_i = 1000 \cdot \left(\frac{\left(Oxide_i \right.}{\left(MW\left(Ox_i \right.} \right.$$

where $MW(Oxide_i)$ is the molecular weight of the oxide from the xrf analysis; $x(Element_i)$ is the number of cations of that element contained in its oxide.

Another useful diagram for the classification of igneous rocks is the R1-R2 diagram of *De La Roche* (1980), where:

$$R1 = 4 \cdot Si - 11 \cdot (K+Na) - 2 \cdot (Fe+Ti);$$

$$R2 = 6 \cdot Ca + 2 \cdot Mg + Al;$$

Q-F and R1-R2 diagram for episyenites and other analysed rock types are presented in figure ***. As we can see, there are three different path for three rock types analysed: a possible interpretation is that each lithological type reacts at the

alteration process in a different way.

(***A***) Cataclasites, that are mainly made of Quartz, describe a path of complete Albitization and quartz dissolution. Here, we can also notice the mass transfer that acted during cataclasite formation: there is a strong enrichment in Silica at the expense of K and Na (path ***A'***).

(***B***) The trend described by the episyenite developed after granitoids highly resemble trend of Type II episyenite of *Cathelineau* (1986). This path forms as a combination of quartz leaching and albitization and probably chloritization.

(***C***) Aplites are subjected to a main phase of dequartzification followed by a weak albitization.

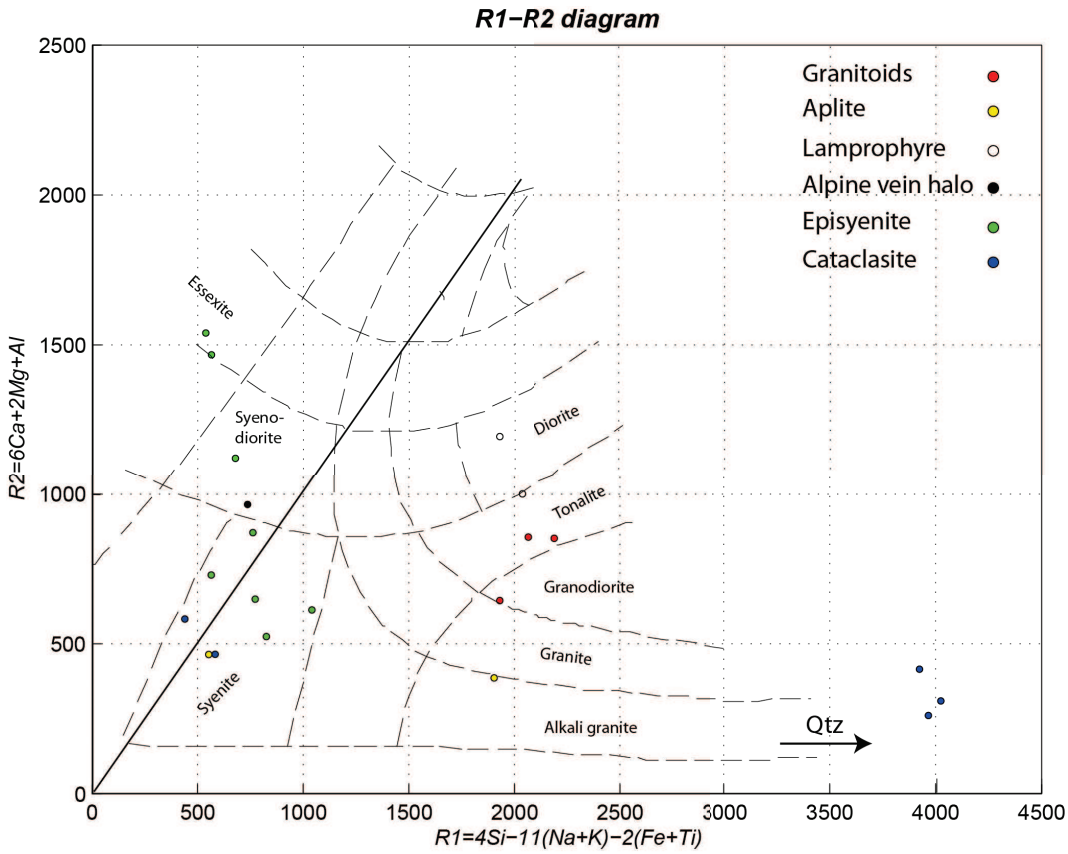

Figure 11: R1-R2 diagram of XRF bulk composition, according to De La Roche (1980).

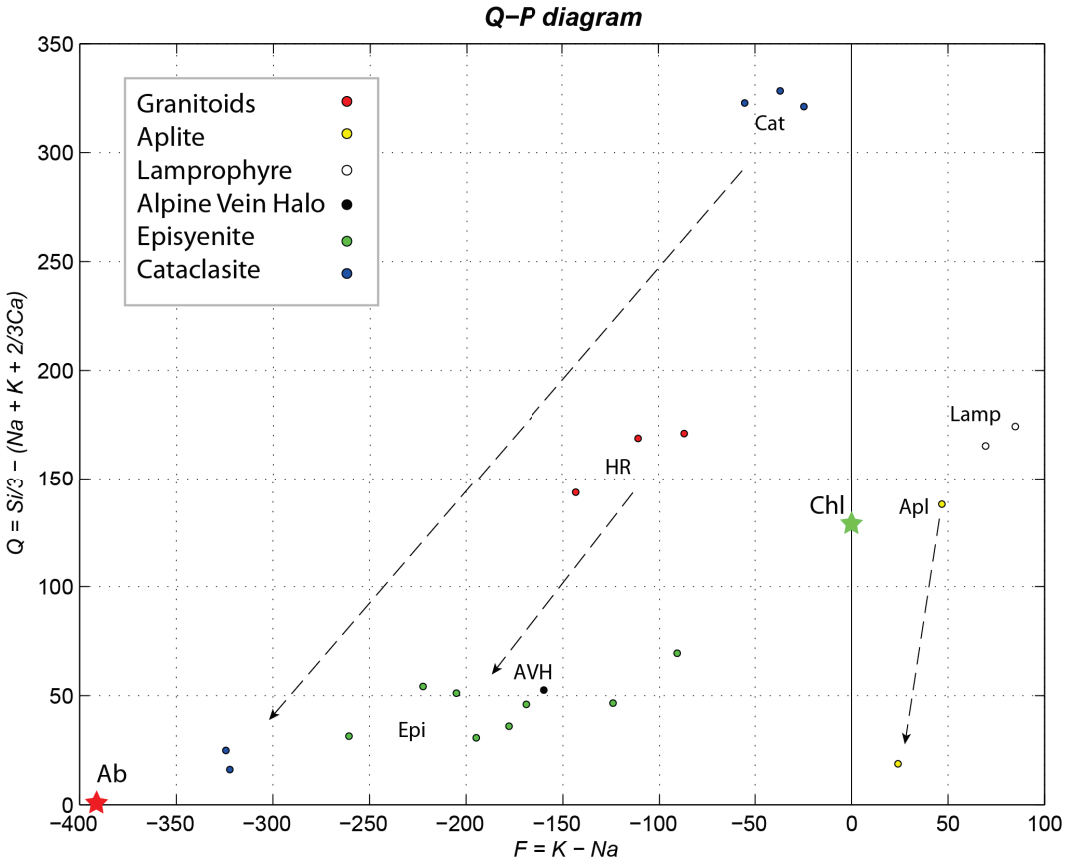

Figure 12: Q-F diagram showing the three main chemical variation path described in the text.

2.5.1.b Isocon Digram

In order to evaluate the real mass changes due to episyenitization, the graphical approach of *Grant* (1986; 2005). This method is useful to evaluate the bulk chemical changes due to metasomatic processes, and it is based on a simple mathematical relationship between concentration and mass/volume, described by *Grensen* (1967) as:

$$C_i^A = \frac{M^O}{M^A} \cdot \left(C_i^O + \Delta C_i \right)$$

where the C_i represent the concentration of the component *i,* the superscript A or O refers to the Altered and Original rock respectively; ΔC_i represent the variation in concentration. M^O and M^A are equivalent mass, that is the mass of the same volume of altered and original rock. We don't know the exact ratio between altered

and original rock mass, so we have to find it solving the equation for some elements that behaved as constant during the alteration, that is whose ΔC_i is equal to 0. In the graphical approach of *Grant* (1986, 2005), we have to plot C_i^A against C_i^O. Constant components, for which ΔC_i is equal to zero, will define a straight line toward the axis origin: the isocon line (isoconcentration line). This line is represented by a simplified form of the previous equation, where $\Delta C_i = 0$:

$$C_i^A = \frac{M^O}{M^A} \cdot C_i^O$$

According to this relationship we can define the mass ratio between altered and original rock, and then, we can obtain the effective change in concentration of all components. An element that plot above this line has increased its concentration during the alteration process; instead species that plot below this line have been lost.

The gain or loss, normalized to the original concentration, during alteration is given by the equation:

$$\frac{\Delta C^i}{C_i^O} = \left(\frac{M^A}{M^O}\right) \cdot \left(\frac{C_i^A}{C_i^O}\right) - 1$$

There are several ways to define the slope of the isocon, and then the overall mass change in respect to M^O (*Grant*, 2005): (a) graphical approaches such as straight distribution of (supposed) constant elements; (b) a priori assumption of constancy of certain components not interested by the alteration process; (c) constant mass or constant volume.

Very often, the constant components assumption is unreliable, and even more in our case. Al_2O_3, TiO_2, and Zr are usually employed as comparison parameters (*Grant*, 2005): the neoformation of Feldspars and Anatase demonstrate that in our isocon analysis we can not absolutely apply this assumption. Therefore, we have chosen to employ a constant volume approach (as in *Cathelineau*, 1986), using the value of porosity given by μ-CT analysis. The relationship for constant volume assumption becomes:

$$C^A = \left(\frac{\rho^O}{\rho^A}\right) \cdot C^O$$

where ρ^O/ρ^A is the density ratio that in our case is define by the mass loss. The mass loss can be assumed to be the same as the porosity (*Nishimoto et al.*, 2014). Micro-tomography has reported an episyenite porosity of 28%: this is the maximum relative value of vug volume because the analysed episyenite were weathered and most of the pore-filling Calcite gone away. Hence, from this number we can have a gross evaluation of the total mass flux during episyenitization.

Concentration changes has been calculated using an Excel spreadsheet and plotted using a dedicated Matlab script. Major elements plotted concentrations do not represent real values: they are all multiplied by an arbitrary numerical coefficient in order to plot them on the diagram in an ordered way.

2.5.1.c Episyenite on metagranitoids

Episyenites developed on granodiorite and aplites (granitoids in general) are strongly depleted in SiO_2, Al_2O_3, Fe_2O_3 and MgO. Instead, Na_2O and LOI are usually gained during the alteration. As we have already seen with the Q-F diagram, this chemical changes are ascribable to quartz dissolution (SiO_2), albitization (Al_2O_3) and alteration of biotite into chlorite (Al_2O_3, FeO, MgO depletion and LOI enrichment). The fickle CaO behaviuor is likely to be due to the simultaneous occurrence of albitization (that should cause a Ca depletion in the rock) and calcite deposition into vugs (CaO enrichment).

2.5.1.d Alpine-type alteration halo

Isocon and bar diagrams of vein alteration halos shows no sensible difference in respect to that of episyenites. The 1:1 proportion of CaO and Al_2O_3 variation led us to think to the destabilization of anorthitic component of plagioclase (where the

two oxides are exactly I the same proportion). FeO and MgO variation are smalles than those in episyenites: this could be due to the maintenance of #Fe during chloritization of biotite.

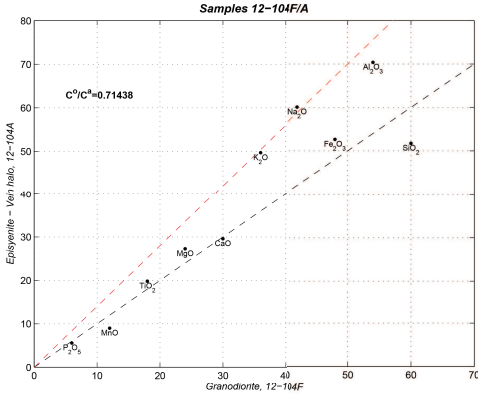

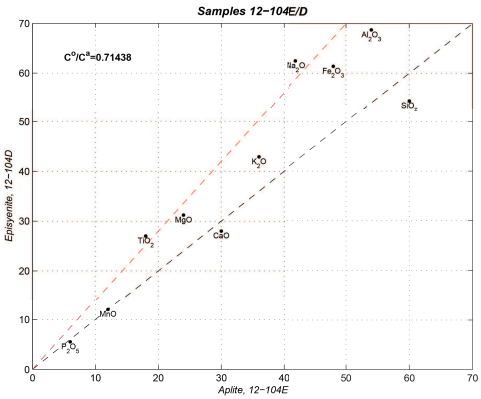

Figure 14: Isocon diagram for samples 12-104A (Alpine-type halo) and 12-104E (Aplite).

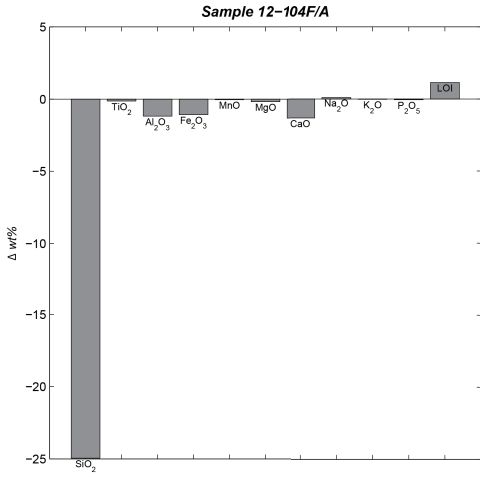

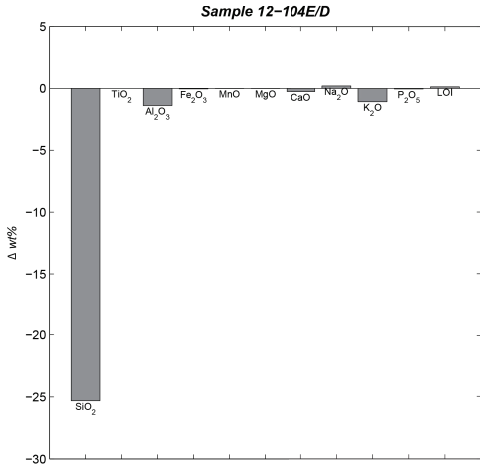

Figure 13: Weight percernt variation of principal elements for the Alpine-type alteration and for the episyenite developed on the aplite.

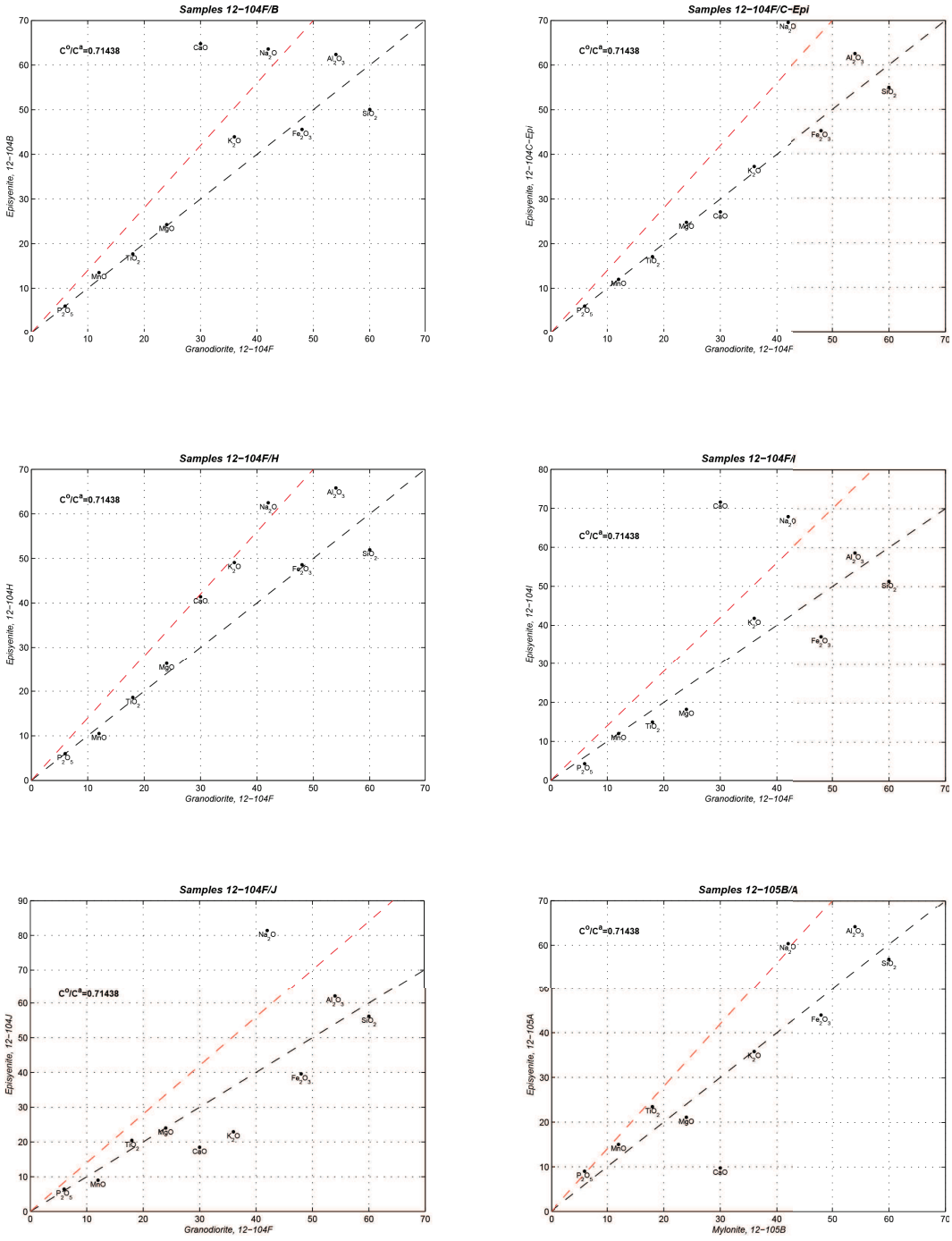

Figure 15: Isocon diagrams for episyenite samples.

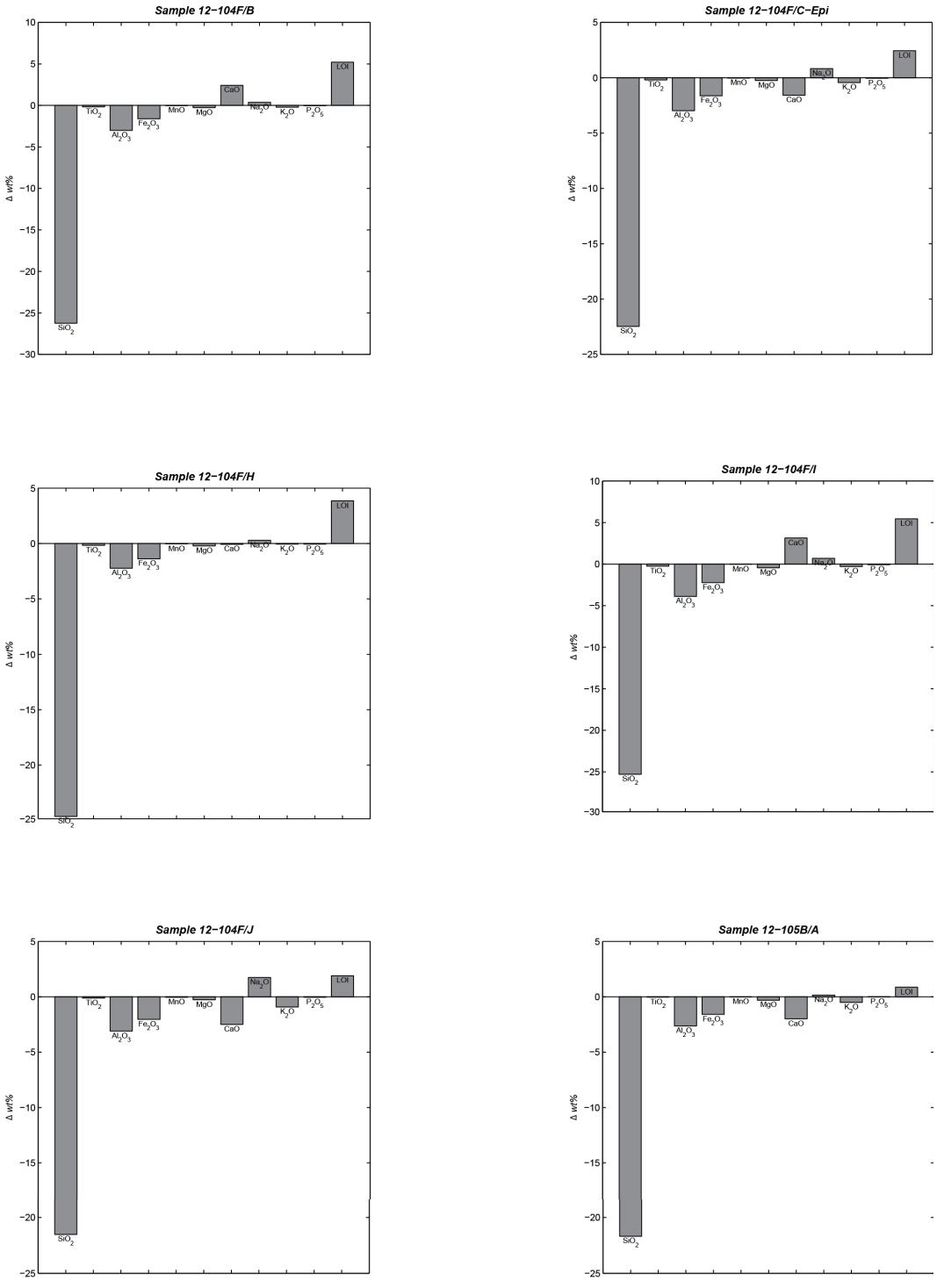

Figure 16: Bar diagrams showing the weight percent variation for episyenite samples.

2.6 SEM – BSE images

The investigation of episyenite thin sections by electron microscopy has revealed the microstructural features, such as porosity at different scale, that characterizes these rocks.

BSE images have been acquired by a CamScan MX3000 (with a LaB_6 source) at the Department of Geosciences, University of Padova. Analytical conditions of image acquisition are reported below each figure in Fig. 2.6.1.

The first observation that results looking at these images is that there are two porosity types characterized by different scale of development, volume involved and genetic process. As it has been already observed on handspecimens and optical microscopy investigations, the outstanding feature of these rocks is a intergranular porosity that develops at the expense of quartz, as Fig. 2.6.1a,b shows. Quartz dissolution starts from grain boundaries and fractures, as we can see from the amoeboid texture of quartz crystals in Fig. 2.6.1a, resulting in the development of a porosity that resemble the quartz "site" of the former rock texture. Therefore, this process lead to the development of a mm-scale porosity.

The most important result obtained from BSE imaging is the peculiar microtexture of plagioclase grains. Magmatic feldspars re-equilibrated under amphibolite facies conditions have an oligoclasic composition without any zonation. Where the rock is interested by episyenitic alteration, plagioclase is characterized by a patchy microtexture defined by heterogeneously distributed μm-scale pores. The BSE image in Fig. 2.6.1e point out the relationship that exist between this second order porosity and the heterogeneous composition of this plagioclase: albitic patches are more porous than the oligoclasic surrounding matrix. Fractures, cleavage and twinning planes are highlighted by this μm-scale porosity (Fig. 2.6.1c,e,f). Albitic haloes develops from these source regions spreading inside the oligoclasic plagioclase. The transition between oligoclase and albite patches are very sharp at the μm scale. The alteration of exsoluted plagioclase lamellae inside perthitic k-feldspar (Fig. 2.6.1c) demonstrate that this alteration process interests only the anorthitic component of feldspars. K-feldspar is not interested by any kind of

porosity or compositional variability. These characteristics are very similar to those described for a general process of plagioclase albitization by *Engvik et alii* (2008). According to *Engvik*, this type of porosity is the result of the re-equilibration of minerals in presence of a fluid phase by an interface-coupled dissolution-reprecipitation mechanism. The replacement of oligoclase by albite occurs along a reaction front that spreads from fluid infiltration points (such as fractures and cleavage planes). Along this reaction front, oligoclase is dissolved in the fluid and albite is directly deposited by supersaturation of the fluid (that should be Na-rich in this case). The reaction products is very porous, given the difference in molar volume between oligoclase and albite and the presence of a fluid phase. Porosity allow to the fluid to reach the reaction front, resulting in the prosecution of the reaction. *Engvik et alii* (2008) reports also a set of secondary reaction product vug-filling mineral phases (calcite, white micas and epidote) that are not observed in our analysed samples.

However, there are no microtextural evidences that define the temporal relationship between the development of these two types of porosity.

Several authors *(Engvik et alii,* 2008; *Petersson et al.,* 2012) proposed a unique mineral reaction that support the contemporary development of quartz dissolution and albitization processes:

$$Na_{0.8}Ca_{0.2}Al_{1.2}Si_{2.8}O_8 + 0.4 \cdot Na^+ + 0.8 \cdot H_4SiO_4 \rightarrow 1.2NaAlSi_3O_8 + 0.2 \cdot Ca^{2+} + 1.6 \cdot H_2O$$

The presence of silicic acid as reactant suggest that quartz dissolution should have occurred before than Na-metasomatism on plagioclase.

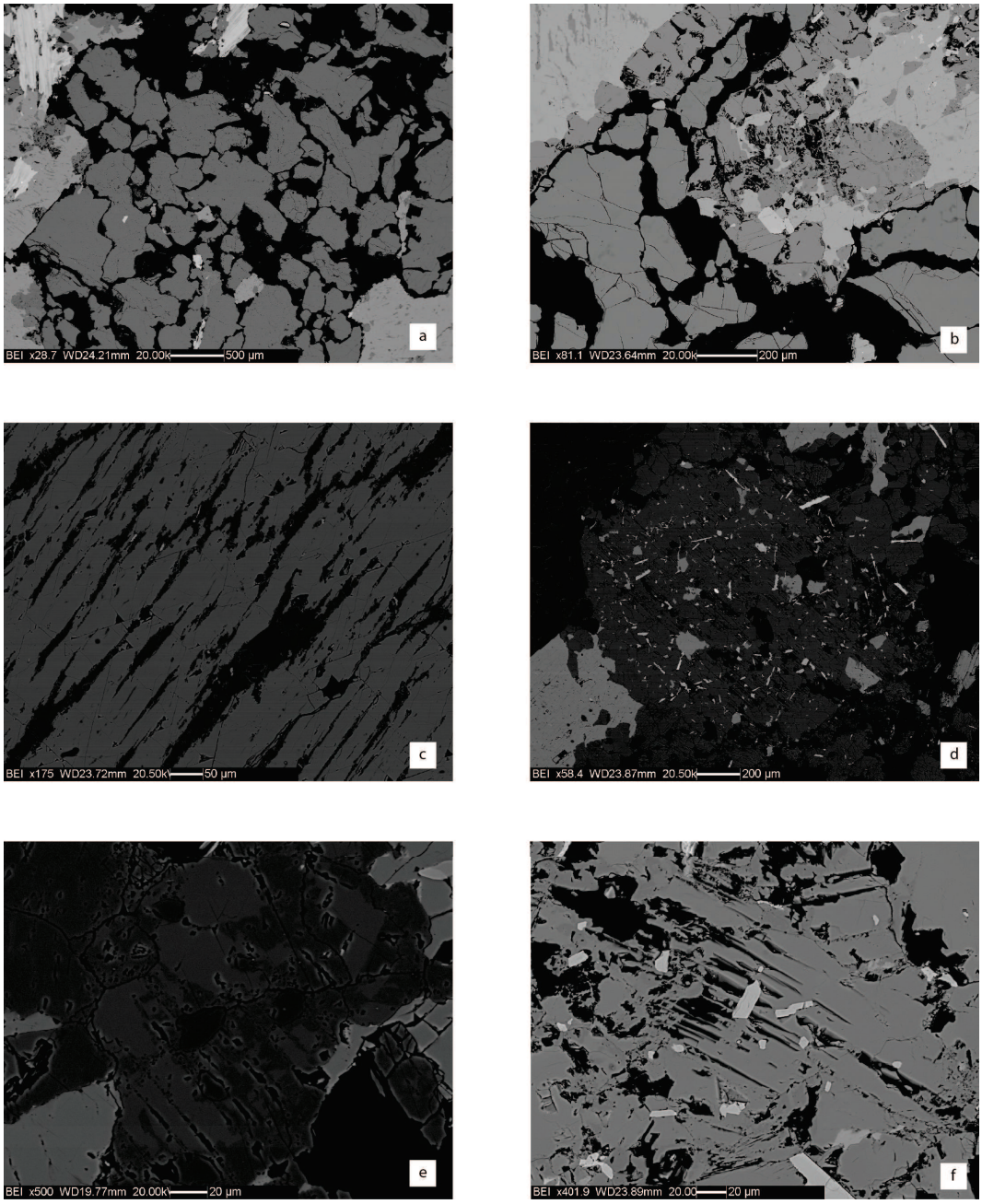

Figure 17: ***(a)*** *corroded quartz grain along crystal boundaries, incipient grade of alteration;* ***(b)*** *quartz and saussuritic plagioclase corroded by the fluids;* ***(c)*** *albite lamellae dissolved inside a perthitic K-feldspar;* ***(d)*** *saussuritic plagioclase that shows its twinning planes highlighted by the alteration;* ***(e)*** *patchy zonation of plagioclase due to the alteration that spreaded from the cleavage and twinning planes;* ***(f)*** *remnants of a former plagioclase destabilized by the saussuritic alteration (given the presence of muscovite inclusions) and then corroded along twinning planes by the albitization process.*

2.7 XRPD analysis and quantification of mineralogy

In order to validate the result obtained from Rietveld refinement of powder diffraction data, a composition-based quantification of mineralogy has been calculated from the XRF bulk chemical analysis using the MINSQ Excel spreadsheet (*Herrmann & Berry,* 2002). In this software, the operator have to insert the right assemblage of rock forming mineral phases, their respective compositions and the XRF analysis. Using mineral formula, the software calculates a fictitious bulk composition. Hence, through a least square minimization algorithm, the software try to find out the right proportion of mineral phases that minimize the difference between observed XRF analysis and calculated bulk chemistry. Residuals lower than 0.5% denote good quantification and agreement between calculated and observed bulk composition.

MINSQ have some limitation: when several phases with similar composition, such as K-phyllosilicates, are present, the software fails to evaluate the right contribution from each phase. Diffraction analysis in this situation are more accurate. Quantification errors are in the order of ±1% in optimal condition.

Mineral compositions utilized here are mostly that obtained from EMP analysis.

Samples 12-104C-Epi and 12-104J have been analysed using the Internal Standard method, adding a part of zinc oxide (ZnO) in 1:10 proportion (10 wt%).

As we can see from the following tables, the main mineralogical changes are: (i) quartz dissolution, with a net change of ca. 25 wt%; (ii) albitization of plagioclase in variable amount; (iii) chloritization of mafic phases and subsequent alteration of chlorite into clay – mineral (illite / chlorite – vermiculite interlayers).

Rietveld quantification

12-104F	***Wt%***	***12-105B***	***Wt%***
Albite calcian	58.1	Albite low	53.7
Quartz	22.6	Quartz	31.1
Annite	11.8	Annite	8.6
Epidote	3.4	Phengite	3.3
Almandine calc	2.7	Microcline	2.9
Phengite	1	Chamosite	0.5
Clinochlore	0.4		

MINSQ quantification

12-104F	***Wt%***	***12-105B***	***Wt%***
Plg1	59.1	Plg1	57.1
Qtz	18.8	Qtz	21.7
Bt	14.7	Bt	13.8
Ep	4.4	Grt	3.7
Grt	3.0	Ms	3.4
Kfs	0.0	Apatite	0.3
Apatite	0.0	Kfs	0.0
Ms	0.0	Ep	0.0
Residual SSQ	0.586	**Residual SSQ**	0.788

Rietveld quantification

12-104E	***Wt%***	***12-104D***	***Wt%***
Microcline	39.6	Microcline	54.2
Quartz	33.5	Albite	41.7
Albite low	25.6	Muscovite	2.9
Biotite	0.8	Biotite	0.7
Muscovite	0.3	Clinochlore	0.6
Chamosite	0.2		

MINSQ quantification

12-104E	***Wt%***	***12-104D***	***Wt%***
Kfs1	40.6	Kfs – Adularia	51.3
Quartz	32.0	Pl2	44.1
Pl1	25.9	Ms	4.2
Bt	1.1	Bt	0.3
Chl	0.1	Chl	0.2
Ms	0.1		
Residual SSQ	0.014	**Residual SSQ**	0.663

Rietveld quantification

12-104C-Epi	*Wt%*	*12-104J*	*Wt%*	*EP-1*	*Wt%*
Albite	69.4	Albite low	77.3	Albite	59.4
Amorphous	13.4	Amorphous	12.7	Microcline	24.8
Illite	7.5	Phengite	5.6	Muscovite	5.6
Calcite	4.1	Calcite	3.9	Quartz	5
Phengite	4.1	Chamosite	0.5	Epidote	2.4
Chamosite	1.1			Calcite	1.7
Hematite	0.4			Clinochlore	0.6
				Biotite	0.6

MINSQ quantification

12-104C-Epi	*Wt%*	*12-104J*	*Wt%*	*EP-1*	*Wt%*
Pl2	71.5	Pl2	76.9	Pl2	54.9
Chl (Verm)	10.9	Chl (Verm)	10.1	Kfs1	18.2
Cc	6.3	Phe	8.3	Ms	7.1
Illite	6.2	Cc	4.6	Bt	6.8
Phe	5.0	Chl	0.0	Qtz	6.0
				Ep	5.3
Residual SSQ	2.625	**Residual SSQ**	0.817	Cc	1.5
				Chl	1.2
				Residual SSQ	0.012

Rietveld quantification

CAT-1	*Wt%*	*12-104C-Cat*	*Wt%*
Quartz	57.5	Albite	93.5
Albite	25.7	Calcite	2.4
Microcline	11.6	Hematite	1.7
Clinochlore	4.5	Illite	1.1
Laumontite	0.5	Phengite	0.6
Biotite	0.3	Chamosite	0.4

MINSQ quantification

CAT-1	*Wt%*	*12-104C-Cat*	*Wt%*
Qtz	55.1	Pl2	87.9
Pl2	25.2	Ms	4.2
Kfs1	10.9	Chl (Verm)	3.1
A-1-Chl	6.6	Cc	3.0
Ms	0.8	Hm	2.0
Bt	0.8	Qtz	1.3
		Kfs1	0.0
Residual SSQ	0.235		
		Residual SSQ	0.118

2.8 Micro – computized tomography

Micro-computized tomography has been performed at the Department of Geoscience (Univ. Padova) using a SkyScan 1172 high-resolution (11 Mpixels) micro-CT. Image acquisition and elaboration has been done using NRecon SkyScan software.

Analytical conditions:

– Source voltage: 100 kV

– Source current: 100 μA

– Rotation step: 0.3°

– Exposure for each image: 1800 ms

– Filter: Al (0.5 mm)

– Image Pixel Sixe (resolution): 13 μm;

Five different tonality of "grey" are readely discernible in raw images (figure**). Hence, with density image segmentation we have defined 5 different group of phases with similar absorption. Absolute density measurements or calculations are not possible, hence we have classified mineral phases according to their relative density and morphology.

In Fig. 2.8.2 are reported the raw and elaborated images with separated density classes: (i) porosity, (ii) plagioclase (Oligoclase), (iii) K-feldspar (plus albite and residual quartz); (iv) chlorite, biotite and epidote, (v) high-density phases: allanite, zircons and possible anatase.

Using an image analysis software it is possible to calculate the area occupied by each phase group in a tomography (2D section of the image). In the table below, are reported the quantification of area proportion between different phases obtained from tomography images, the quantification obtained from Riedveld refinement of diffraction data of a similar sample, and the MINSQ quantification of the analysed sample. Considering the local variability and heterogeneity of the sample, there are good agreement between data obtained from different analytical

methods.

Area quantification	
EP-TOMO	**Area%**
Pl	65.9
Chl-Bt	5.9
Hd	0.1
Kf	28.2

Rietveld	
EP-1	***Wt%***
Albite	59.4
Microcline	24.8
Muscovite	5.6
Quartz	5
Epidote	2.4
Calcite	1.7
Clinochlore	0.6
Biotite	0.6

MINSQ	
EP-TOMO	
Pl2	51.0
Kfs1	29.6
B-ep	6.9
Quartz	6.4
A-1-Chl	3.2
B-Bt (hostrock)	3.0
Cc	0.0
Residual SSQ	0.4

Sections of the sample 3D reconstruction based on tomography images are reported in Fig. 2.8.1. “Voxel” (volume per element) occupied by the porosity have been quantified in 28% of the total volume.

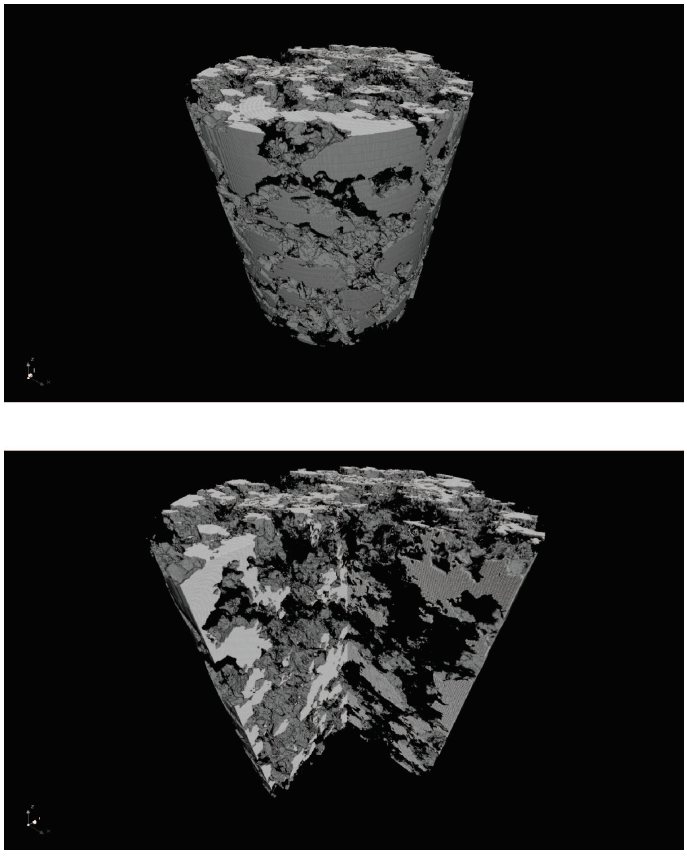

Figure 18: three-dimensional reconstruction of the cylindrical sample of EP-TOMO. Here the porosity is represented by the solid (grey) portion of the shape.

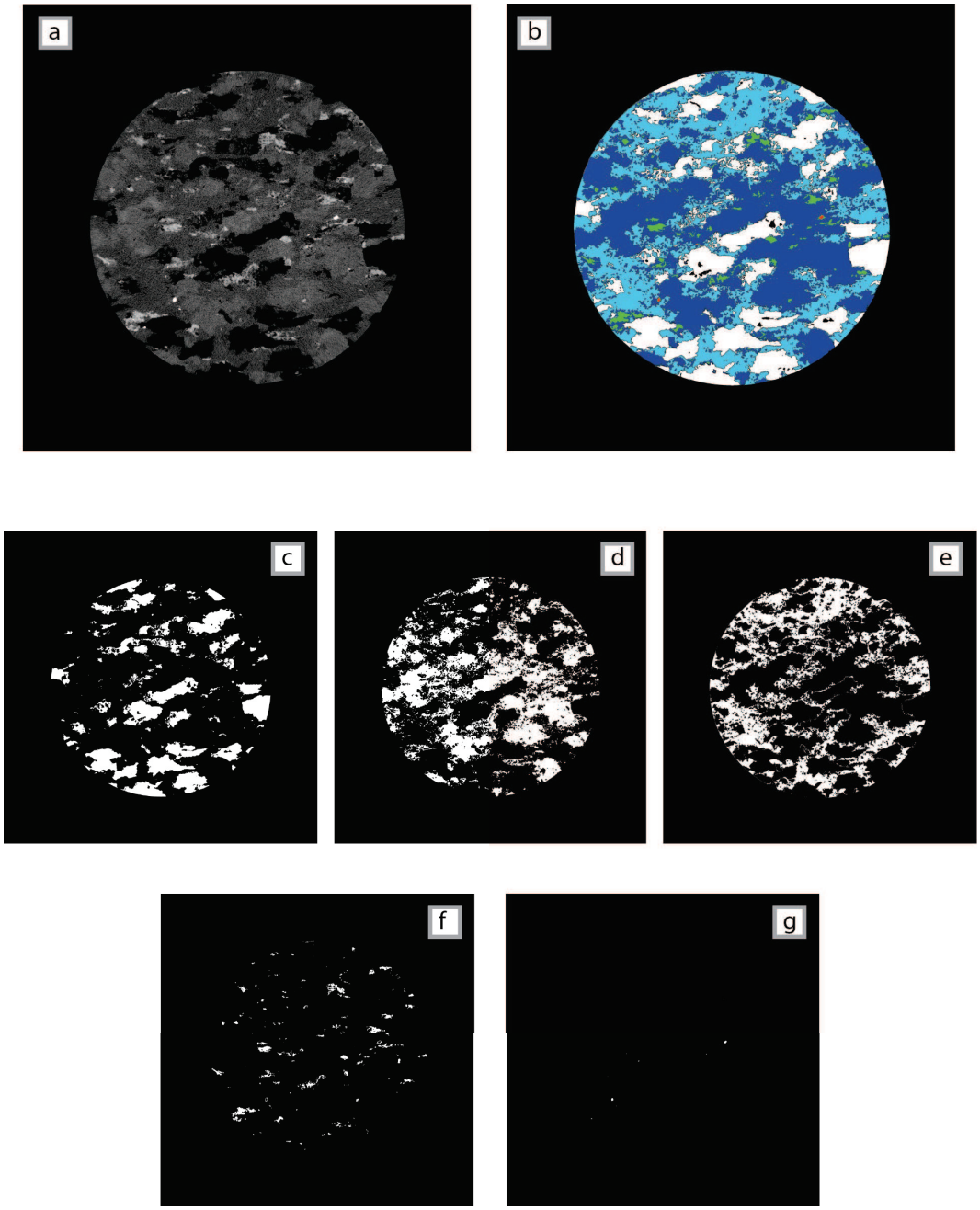

Figure 19: Segmented microtomography sections: comprehensive image before ***(a)*** *and after phase segmentation* ***(b)****;* ***(c)*** *porosity;* ***(d)*** *plagioclase;* ***(e)*** *K-feldspar;* ***(f)*** *biotite and chlorite;* ***(g)*** *high-density phases.*

2.9 Stable isotope analysis of Calcite

Dr.ssa Patrizia Ferretti is gratefully acknowledged

for data acquisition and elaboration

Four different single crystals of Calcite have been separated and prepared for isotopic analysis. Two of them comes from amphibolite-facies Qtz + Bt + Pl + Cc veins (Calcite Vena 11-240 and Neves Calcite Vena) of the Mesule area. Sample SANE01 comes from a Qtz-Chl vein of the Schwarzenstein area. Calcite Episyenite have been sampled at the Moosboden episyenite outcrop (3.a) along a fracture linked to the fault system.

Each sample has been hand-crushed on a agathe mortar. Analysis were performed at the University of Cambridge (UK).

From those isotopic data we can have a gross evaluation of the relative temperatures of formation of calcite in different veins.
As we can see in Fig. 2.9.1, $\delta^{18}O_{(SMOW)}$ data indicate that calcites of amphibolite facies and Qtz-Chl veins have a higher temperature signature than that of episyenites, as it should be expected given their different metamorphic environment of formation (respectively amphibolite-greenschist facies and "epithermal" environment). Oxigen composition of episyenite calcite is very similar to that presented in *Simmons et al.*(1994; $\delta^{18}O$=4.5‰) for platy hydrothermal calcite deposited by chloride solutions in a temperature range between 160°C and 300°C. $\delta^{13}C_{(PDB)}$ data suggest a different origin for carbon in calcite: in general, episyenite calcite shows a strong influence from bicarbonates dissolved in meteoric waters. Further analysis need other data.

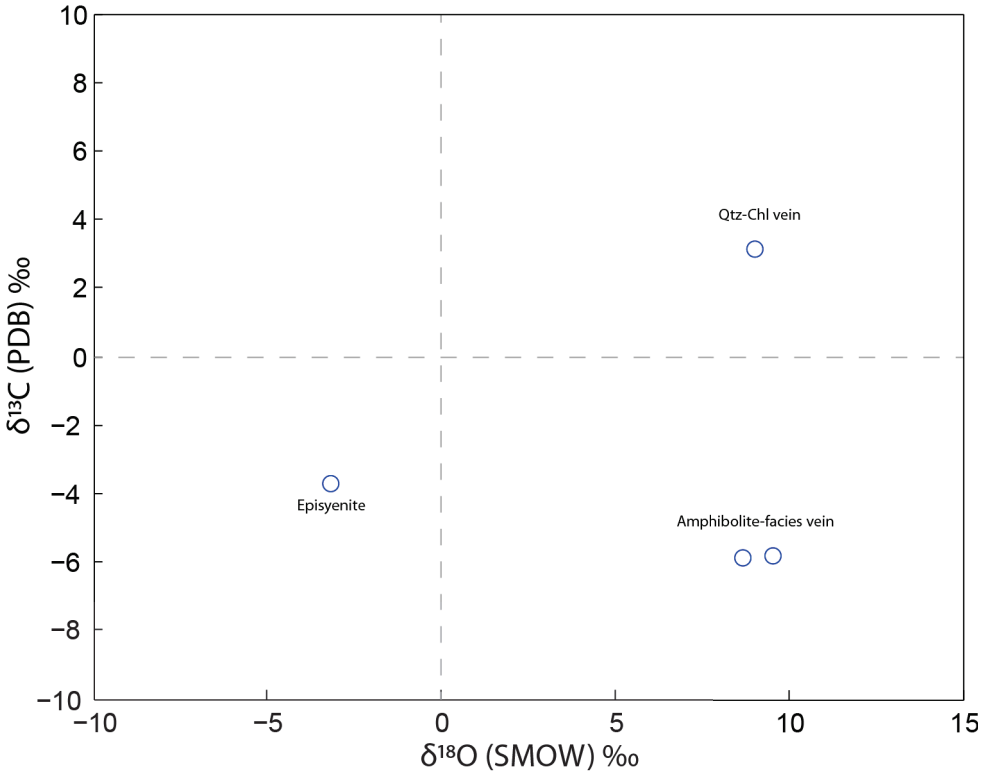

Figure 20: Carbon and Oxigen isotope ratios for calcite of different metamorphic origin from the Zillertal Gneiss Core.

2.10 Conclusion

Epiyenites are the result of fluid-rock interaction along fault planes and nearby volume of rock. Even though episyenite occurrence and distribution is controlled by fracture geometry and spatial arrangement, fracture density and/or the presence of important damage zones do not influence the location of episyenite development.

- Episyenites are always found in strict correlation with faults or fracture system; not all faults are decorated with episyenites and, when present, they characterize only parts of the entire structure;
- Fracture often defines the outcrops-scale geometry of episyenites according to their spatial arrangement; they commonly bound the alteration acting as restraining walls, but in most cases fractures work as the central pathway of fluid;
- There are no clear relationship between faults kinematics, throw, cataclasite thickness and the development of the alteration: episyenites can develop from knife-sharp fractures with no displacement as it can be found along with evolved structures with tens of meter of throw and meter-wide cataclastic horizons; sinistral and dextral structures are equally interested by episyenitization;
- Fracture density have not any direct control on alteration development: highly-fractured contractional jogs often do not present any kind of alteration, in contrast with single knife-sharp fractures that are often highlighted by highly porous halos;
- The composition of the host rock influence the spatial development, indeed quartz-poor lithologies commonly limit the diffusion of the fluid and of the alteration; in a similar way ductile textures of the host rock may limit or restrain the fluid diffusion.

These features demonstrate that, unfortunately, in a superficial hydrothermal environment there are no strict relationship between fluid pathways geometry,

fracture density, rock texture that can help to obtain useful information on the prediction of episyenite-type ore-deposit spatial development.

Stable mineral phases are: albite + vermicular chlorite + calcite + anatase ± muscovite ± adularia ± apatite ± ematite; and in a few rare cases is also found a second generation of quartz. The peculiar geometry of episyenite bodie, along with their mineral paragenesis and the association with mineralized veins are elements that suggest the origin of episyenites from process of fluid-rock interactions in a hydrothermal environment.

Episyenites are characterized by high porosity both at the hand-specimen scale and at the grain scale. In general, about one third (28vol%) of the original rock volume is now occupied by vugs and voids from the centimetre to micrometre scale. Mineralogical changes, bulk chemical variation and textural analysis point to define different genetic processes at the source of these two porosity types: (i) millimetre scale porosity is due to quartz dissolution as it can be deduced from the decrease of qtz content from about 30wt% in intact granitoids to 0-5wt% in episyenites and the average 25wt% drop in SiO_2 content; (ii) micrometre scale porosity is due to the albitization of anorthitic plagioclase as we can see from patchy compositional texture of porous plagioclase in BSE images that is also reflected by the slight enrichment in Na_2O content linked to albite crystallization and oligoclase substitution.

Engvik et alii (2008) and *Petersson et alii* (2012) proposed, in different terms, a unique mineral reaction that support the contemporary development of quartz dissolution and albitization processes:

$$Na_{0.8}Ca_{0.2}Al_{1.2}Si_{2.8}O_8 + 0.4 \cdot Na^+ + 0.8 \cdot H_4SiO_4 \rightarrow 1.2NaAlSi_3O_8 + 0.2 \cdot Ca^{2+} + 1.6 \cdot H_2O$$

According to this reaction, quartz dissolution occurred just before or at the same time of Na – metasomatism of plagioclase.

A similar hydrothermal alteration predates and locally overprints episyenitization.

Alpne-type vein halos are episyenite too, but field, mineralogical and isotopic data demonstrate their different origin. Metasomatic halo morphology of Alpine – type veins account for the genetic process of lateral secretion and, therefore, account for a local provenance of parental fluids: this fact is also supported by the isotopic signature of vein calcite (9 ‰ $\delta^{18}O$ – SMOW). Episyenites morphology and isotopic analysis suggest a strong influence of meteoric fluids conveyed through preexisting faults and brittle structures.

Concluding, the Zentralgneis have undergone a long history of multiple stages of fluid-rock interaction during its uplift. In the hydrothermal environment, Alpine-type veins, episyenites and cataclasites seems to have recorded this passage throughout all the alteration zones, from the propylithic, toward sericitic and potassic and silicic zones. Brittle structures have been exploited as fluid pathways many and many times, recording in the host rock all the history of fluid rock interaction.

Chapter 3

Fluid inclusion study on qtz in cataclasites

Microthermometry has been performed on fluid inclusion contained in quartz from sample 13_334 (N46° 57' 28" E11° 44' 47").

This specimen comes from the fault core of a sinistral strike-slip structure belonging to the "Mesule faults system" (75°vs275°, Sinistral, throw: 3m; width of cataclasite: 10-15 cm,10-8 of which made of massive quartz). The protolith and host rock is a granodiorite (Zentralgneise). Under unaided eyes, it shows two part with different textures: (i) a cataclasite *s.s.* with a Qtz+Pl+Mu+Chl stable assemblage as it has been already described; (ii) vein-like massive and euhedral quartz in which clasts of cataclasite and host rock are suspended (Fig. 3.4.1). This peculiar fabric is a common feature of several faults of the Mesule system. From field and microstructural surveying, it has been interpreted as the result of a latest phase of activity and dilatancy of these structures. Fluid inclusions are contained in this massive quartz portion of the cataclasite.

One of the first reason that encouraged us to perform microthermometric studies was the possible relationship existing between qtz-depleted episyenites and qtz-filled cataclasites. Given that both events are linked to faults, we have supposed that these two rocktypes may represent respectively source and sink of fault-driven fluids. Hence, inclusions should give us some constraints on fluid composition and physical conditions at which dilatancy and episyenitization occurred. Field evidence have demonstrated later that this "hydraulic" connection is not so straightforward because qtz-rich cataclasite are very often overprinted by the hydrothermal alteration, but at the same time in some episyenite outcrops, a second generation of Qtz is often found.

3.1 Sample preparation and methodology

Two double-polished thick sections (150 μm) have been cut from sample 13_334. A first characterization and classification of fluid inclusions has been made under optical microscope, and then suitable areas for microthermometry were selected. Sections are then left in acetone for 24 hours in order to divide section from glass and clean them up from any trace of superglue. Then, 18 selected areas have been cut and collected separately.

Microthermometric measurements have been performed with a Linkam TH600 heating/cooling stage at the Department of Geoscience, University of Padova. Before the execution of thermometric study, the instruments has been calibrated using CO_2 and H_2O synthetic standards, in order to define the possible error magnitude and a calibration line. Calibrations shows that instrument accuracy is in the order of ±0.1°C and a reproducibility of 0.2°C.

A first surveying of phase transition has been made at high cooling/heating rates (80°C/min) in order to identify essential transition points. Each sample then, has been cooled down to -90°C and then heated up toward the melting temperature at variable decreasing rates (60°C/min till first melting occurs, 5°C/min in the melting range, 1°C/min across the T_m). Homogenization temperatures were measured in a later lab experience, at higher heating rates (80°C/min). No decrepitations were observed.

3.2 Data acquisition and analysis

Most of the observed and investigated fluid inclusions hosts two phases (L+V, fluid-rich, 10-20% volume of vapor according to *Bodnar*, 1984) and only a few cases have shown solid phases at their interior (Fig. 3.2.1d). Inclusions are usually arranged into disordered three-dimensional clusters (Fig. 3.2.1a) or planar surfaces dipping into the crystals (Fig. 3.2.1c). Inclusions along grain boundaries are also present but no data have been collected on them. Inclusion are always smaller than 40 μm, with the exception of big irregular ones that in some cases

reach 60 μm in length. There are no distinct classes of morphology: the whole set of observed inclusion spreads from irregular to negative crystal shape passing through all the intermediate morphological types. However, in order to facilitate data analysis, an artificial subdivision in irregular, rounded and negative crystal shape is made. According to this classification, irregular and rounded inclusion are preferentially found in three-dimensional clusters, instead negative crystal inclusions describe linear trails and planar surfaces (fractures and/or crystal growth surfaces). This is not the rule, anyway. Therefore, a classification in primary, secondary and pseudo-secondary inclusions based on morphology is not always reliable where there are no other evidence (such as fractures or growth surfaces).

This wide spectrum of morphologies may have been caused by post-entrapment modifications: several examples of necking down are observed despite the belonging shape class. However, the occurrence of crystals with different inclusion density and crystal habit reveals the presence of several phases of fracturing and entrapment.

Over 100 data of melting and homogenization temperature have been collected. Melting temperatures T_m are all bracketed between -2 and 0°C. There are also some exception: a restrict number of inclusion (6) melts at variable temperature above 0°C, from 2.4 to 6.0°C. These data are not reported here because of their irreproducibility: in each experiment melting have occurred at different temperatures.

A melting temperature next to 0°C suggests an aqueous composition of the inclusion, and with a very low content of salts. *Bodnar and Vityk* (1994) have proposed an equation that describe the relationship between freezing point depression and salinity for a H_2O-NaCl system with a salt content smaller that the eutectic composition (23.2wt% $NaCl_{eq}$):

$$\text{Salinity (wt\%)} = 0.00 + 1.78 \cdot \theta - 0.0442 \cdot \theta^2 + 0.000557 \cdot \theta^3$$

where θ represent the freezing point depression in °C. According to this equation, the observed fluid inclusion have a low salinity content, included between 0 and 2.5 wt% $NaCl_{eq}$. Density values, obtained graphically following *Wilkinson* (2001, fig. 6), are all included between 0.75 and 0.95, with a strong clustering between 0.83-0.93 (figure ***). Isochores and critical point for H_2O-NaCl system have been calculated again according to the equation proposed for by *Bodnar and Vityk* (1994). Isochores steepness, thus, have been calculated with the following equation:

$$dP/dT\ (bar/°C) = a_s + b_s \cdot T_h + c_s \cdot T_h^2$$

where T_h stands for temperature of homogenization, a_s, b_s, c_s are parameters function of Salinity (wt%) for which I refers to the above-named paper for further information.

Given that T_h shows two peak of frequency around 210°C and 175°C, in Fig. 3.2.3E have been reported isochores calculated for these temperatures (with a Salinity of 1 wt% $NaCl_{eq}$).

Quartz in cataclasite 13_334, therefore, contains low-salinity aqueous fluid inclusions. These salinities and homogenization temperature are in agreement with a possible definition of the hydrothermal system as epithermal (*Wilkinson*, 2001).

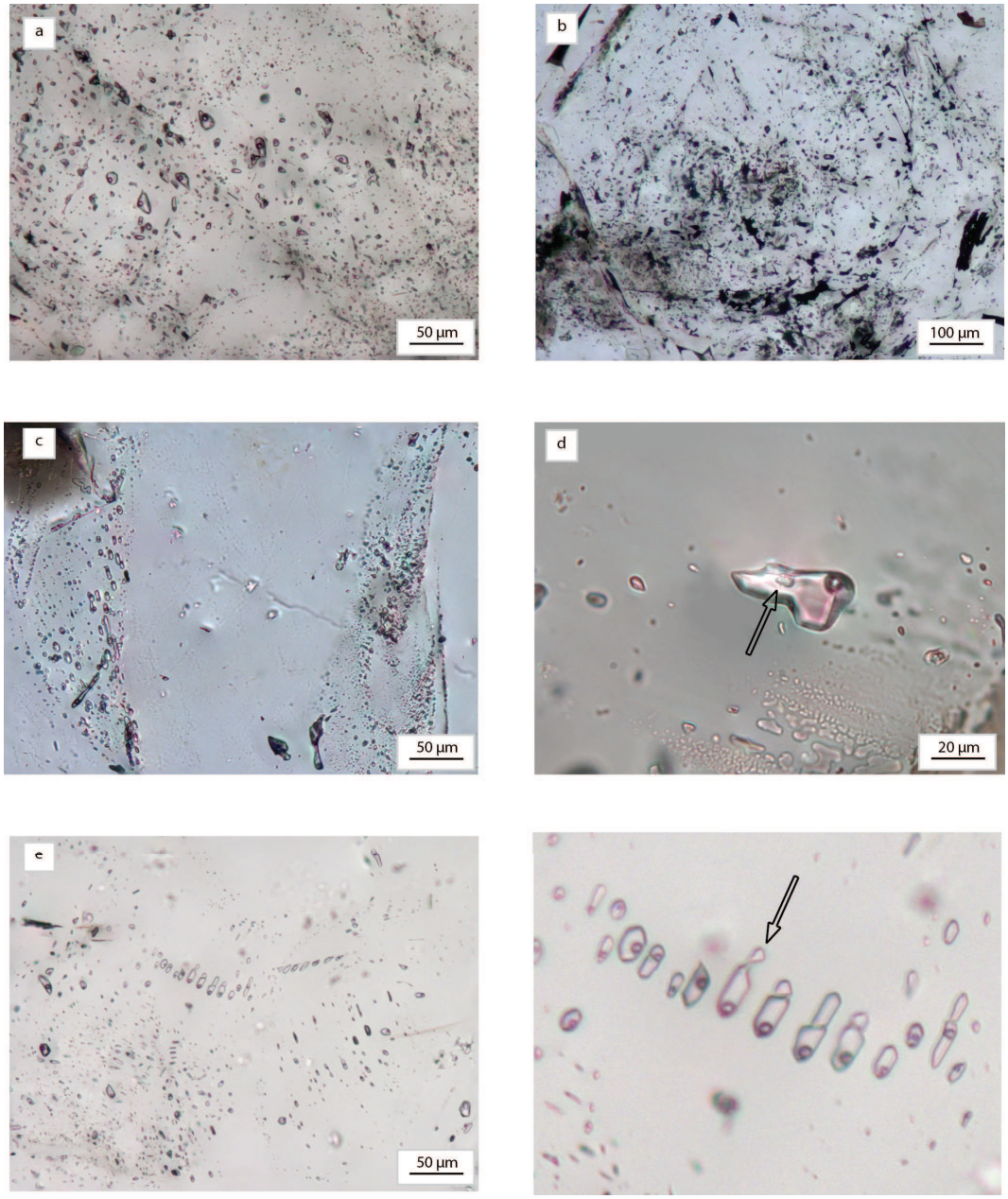

Figure 1: examples of fluid inclusions observed and measured during the experiments: ***(a)*** *rounded fluid inclusions arranged in an irregular three-dimensional cluster; L+V (V occupies 10-15 vol%);* ***(b)*** *growth surfaces in zone with the <c> axis of quartz defined by fluid inclusion planes;* ***(c)*** *secondary negative-crystal shaped fluid inclusion aligned along fracture planes;* ***(d)*** *big tri-phase fluid inclusion; the solid phase is insensitive to temperature changes;* ***(e)*** *pseudosecondary fluid inclusions with well developed negative crystal shapes;* ***(f)*** *articular of (e) showing necking down of negaive-crystal inclusions.*

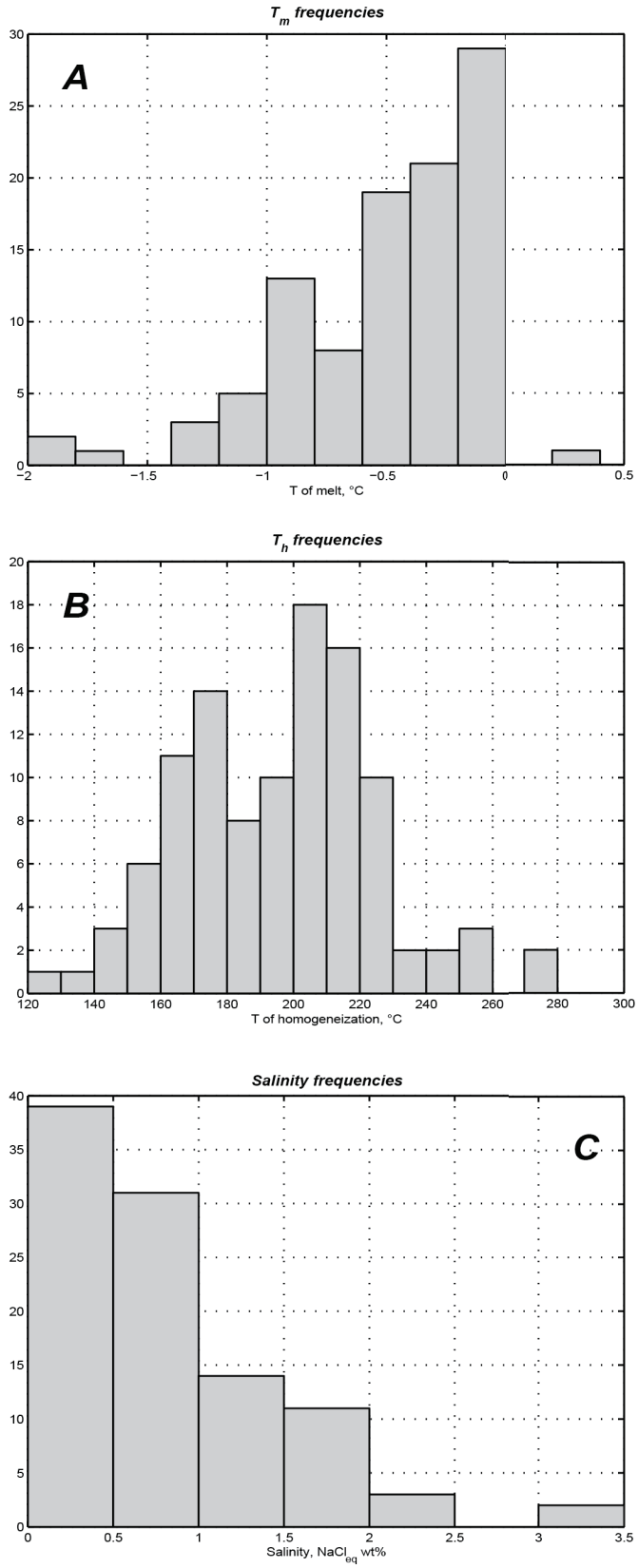

*Figure 2: Bar diagrams representing respectively: **A** – measured frequencies of temperature of melting; **B** – frequencies of homogeneoization temperatures; **C** – frequency of the calculated fluid salinity.*

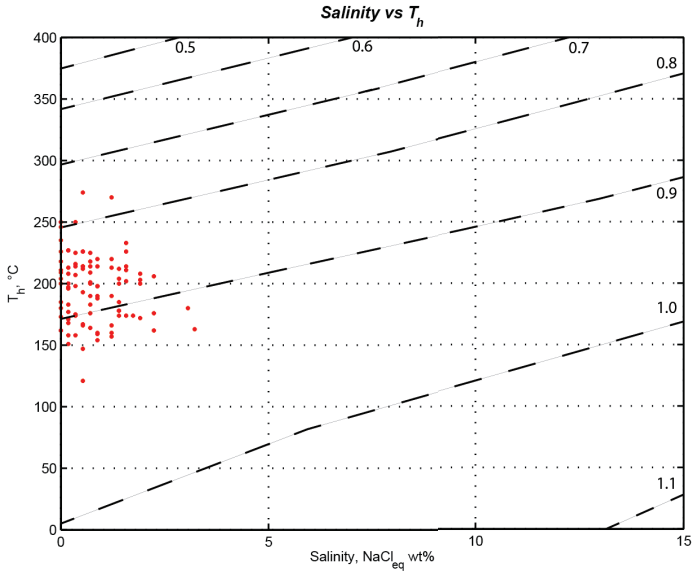

D

E

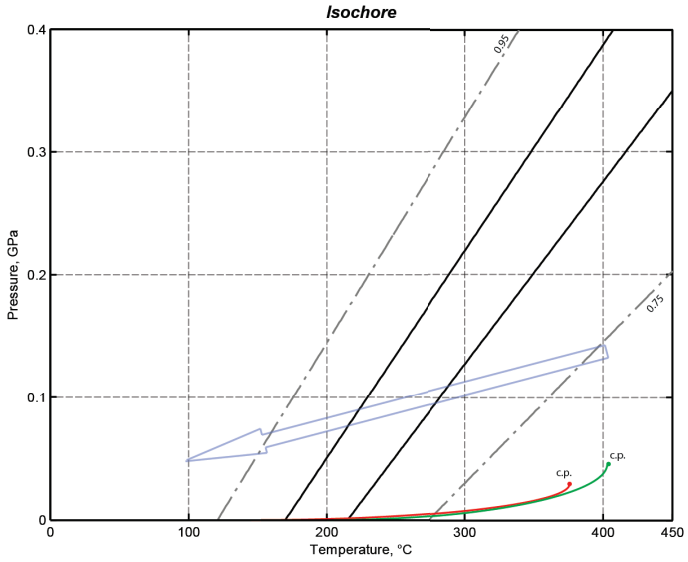

Figure 3: ***D*** *– clustering of microthermometric data in the Salinity vs. Homogenization temperatures diagram.* ***E*** *– calculated isochores (black dahed and solid lines). The bold arrow define a general exhumation path, from Selverstone et al. 1995. Green and Red curves are the equilibrium curves with their respective critical point (c.p.) calculated for aqueous solution with a salinity of: (Red) 0 wt% and (Green) 5 wt%.*

3.3 Data interpretation

In figure 3.2.3E is reported (bold arrow) the terminal part of the P-T-t path presented in several works of *Selverstone* (e.g. 1984, 1995; *Axen*, 1995) for the western Tauern Window. Lower PT condition constraints have been obtained from fluid inclusion studies (*Selverstone*, 1995; *Axen*, 1995). The sample 13_334 should have follow this path during its uplift history. Therefore, entrapment pressure P_e and temperature T_e should be defined by the intersection between isochores and P-T-t path. These intersections fall into a restrict range of pressures (0.5-1.3 MPa) but also into a wider one for temperature (from 100 to 400°C). If we consider the average data represented by the two central isochores identified before, this range is better defined (0.9-1.1 MPa and 225-275°C). However, data are again scattered over a wide range of temperatures. This scattering could be due to post-entrapment modification, consequence of the reequilibration of inclusion to new conditions encountered during the uplift. Underestimation of pressure due to post-entrapment modifications have been estimated by 0.7-1.5 kbar (*Selverstone*, 1995). However, post-entrapment modification should have led to strong textural changes of inclusions (*Vityk*, 1995; *Sterner*, 1989; *Bodnar*, 2003; *Barker*, 1995). In this case, no microstructural features clearly ascribable to reequilibration processes have been observed.

Pressure ranges defined above, describe a superficial environment of the Upper Crust (~5 km). At this depths, the pressure conditions recorded by fluid inclusions could reflect the hydrostatic and not the lithostatic pressure. *Sibson* (1994) have demonstrated that, for P lower than 0.25 Gpa (i.e. ~10 km), pressure regime could be hydrostatic. Fractures and veins act as communicating channels and fluid pathways. This means that, fluid inclusion entrapped in cataclasites and veins should record hydrostatic rather than lithostatic pressure. Hydrostatic pressure can vary frequently and considerably as a consequence of fault activity, vein opening, fracture sealing, ecc. (*Sibson*, 1994). Therefore, fluid inclusion entrapped under this hydrostatic regime may record different pressure condition (i.e. different fluid densities) even though they have formed at the same depth or temperature.

Concluding, there are no sufficient data for the formulation of a correct interpretation. Three possible way are still open: (i) entrapment during fault activity at variable P_{fluid}; (ii) post-entrapment modification; (iii) entrapment during uplift under decreasing PT conditions. Further investigations are needed.

3.4 –Implications for Episyenites

Cataclasites are usually overprinted by episyenite, as we can see from bulk XRF analysis of several samples (cat388 – 12-104G), but there are no occurrence of massive quartz alteration. Some (rare) episyenites are instead characterized by a second generation of euhedral quartz growing in their pores. In addition, the temperature range defined by homogenization coincides approximately with the temperature valuation obtained from chlorite geothermometers (200-250°C). Literature on fluid inclusion in episyenites reports low-salinity compositions (*Lopez-Moro et al.,* 2013).

There are no other evidence in support of quartz transport from episenites to cataclasites, but there are not any evidence that completely deny this theory, too. Further information are needed in order to prove or not the "hydraulic relationship" between qtz in cataclasite and episyenite.

Figure 4: Massive quartz vein inside the cataclasite. On the left side it is possible to see cataclasite clasts suspended in the quartz matrix. On the right, instead, is located the original cataclasite. Fault 13_334.

Chapter 4

U-Th/He on Zircon dating

Dr. Benedetta Andreucci is gratefully acknowledged for her help and collaboration.

4.1 Sample selection and analysis

Zircons and Apatites were selected and hand-picked under an optical stereoscope directly from the handspecimen of the most altered episyenites (samples 12_104H-I-J). In those samples, the biotite-replacing clay minerals form small aggregates that are easily separated from the rest of the rock without crushing and milling. Zircons and Apatite are usually found inside these clay-rich sites.

	Raw date (Ma)			Corrected date (Ma)		
		σ (Ma)	σ %		σ (Ma)	σ %
AC_EP_1_Zr	8.876	0.127	1.432	10.78	0.15	1.44
AC_EP_2_Zr	8.612	0.124	1.439	10.46	0.15	1.44
AC_EP_3_Zr	9.295	0.131	1.412	11.30	0.16	1.42
AC_EP_4_Zr	8.940	0.132	1.481	11.62	0.17	1.49
AC_EP_5_Zr	9.314	0.130	1.399	11.56	0.16	1.40

	Th/U	Ft 238U	Ft 235U	Ft 232Th	Rs (um)	ppm eU (morph)	ppm eU (Zr)	eU (morph)/eU (Zr)
AC_EP_1_Zr	0.333	0.826	0.800	0.800	70.63	722.73	933.26	0.77
AC_EP_2_Zr	0.396	0.826	0.800	0.800	70.77	740.97	1088.75	0.68
AC_EP_3_Zr	0.260	0.825	0.799	0.799	70.27	1185.85	1625.59	0.73
AC_EP_4_Zr	0.418	0.774	0.741	0.741	53.44	364.11	417.58	0.87
AC_EP_5_Zr	0.327	0.809	0.781	0.781	64.00	503.96	599.38	0.84

A hundred of Zircon single crystal have been separated. Most of them had prismatic bipyramidal tetragonal habit with the longest axis up to 500 μm. However only a few were completely intact, without abraded surfaces or fractures and then suitable for U-Th/He thermochronology. Only five of the best zircons have been selected to be packed and analysed. Before packing, crystals have been photographed and measured on two perpendicular sides, usually those parallel to the <a> axis. Width and height of the pyramids and total length of the crystal

(prism plus pyramids height) have been measured in order to define a geometrical approximation of the real shape. Then, crystals have been packed in a Nb-tube.

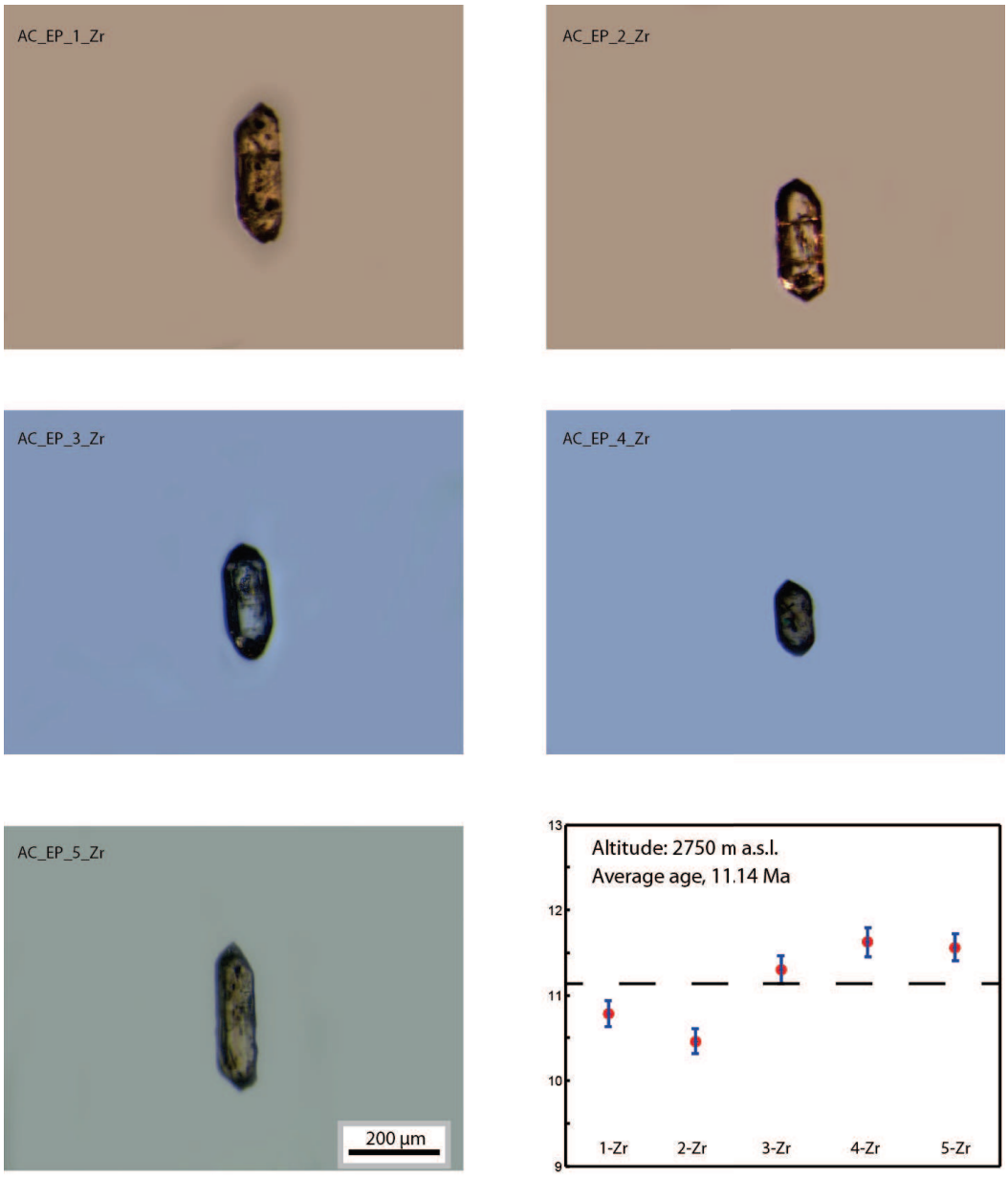

Figure 5: Selected zircons for U-Th/He dating. Diagram representing average data obrained from U-Th/He dating.

Analysis were performed at the Arizona Radiogenic Helium Dating Laboratory, Department of Geosciences, University of Arizona.

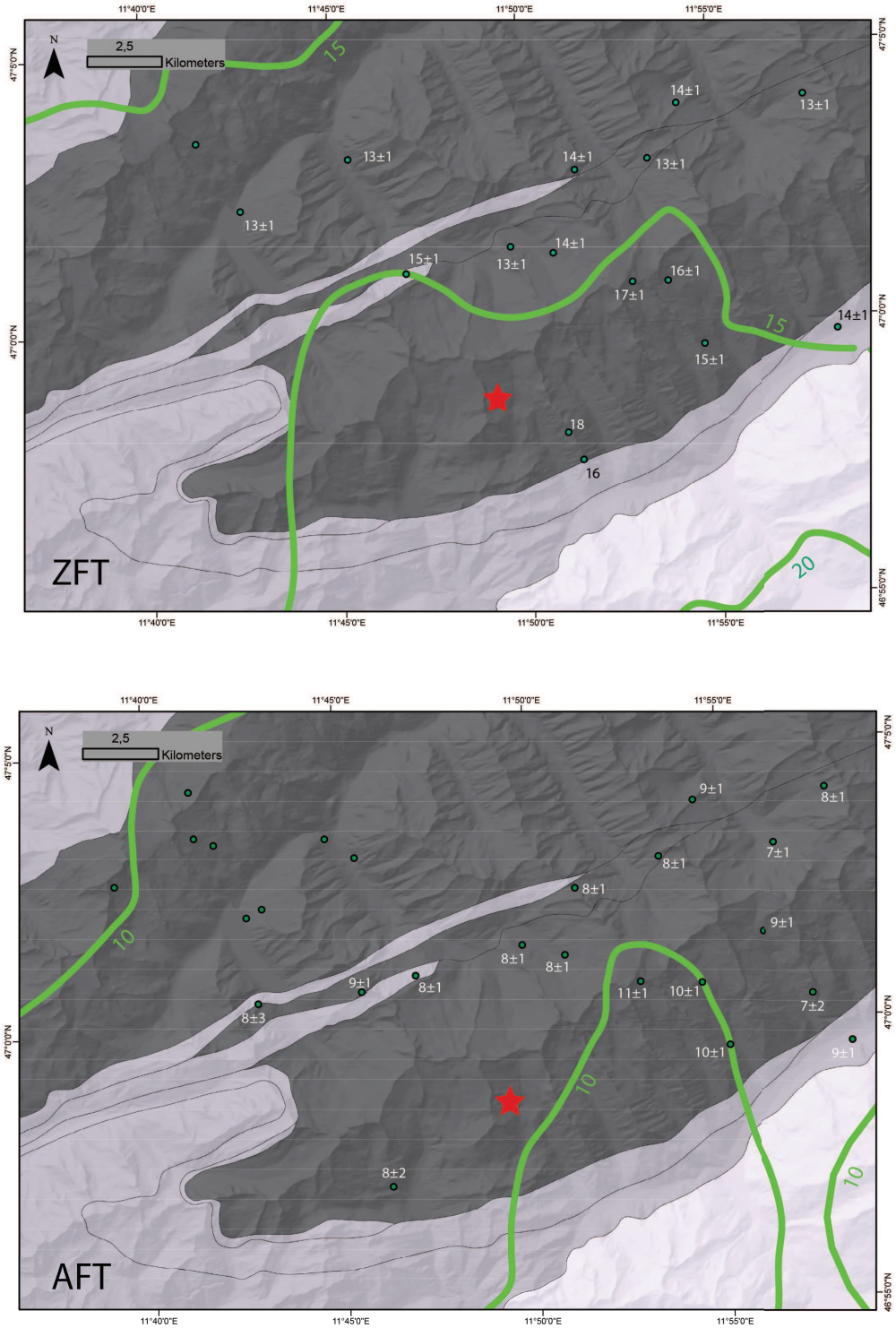

Figure 6: Sketch maps representing the regional distribution of respectively, Zircon Fission Track and Apatite Fission Track ages reported in literature (from Luth & Willingshofer, 2008; Most, 2003; Bertrand, 2013).

4.2 Data interpretation and discussion

Data discussion is entirely based on the database presented in *Luth & Willingshofer* (2008). The first step toward a right interpretation of thermochronologic data is the definition of a T_c, a closure temperature for the He system in Zircons. Several works based on experimental and natural data report variable T_c ranging from 140°C (*Reiners*, 2002, from very high damaged zircons in experiments; *Lünsdorf*, 2013) to 200-230°C (*Reiners,* 2002; *Reiners & Brandon*, 2006). T_c depends also on the rate at which the system cools down (*Reiners & Brandon*, 2006). Available literature reports different cooling rates during the retrograde metamorphic history and exhumation of western Tauern Window: from 375°C to 230°C cooling proceeds at ca. 50°C/Myr (*Selverstone*, 1985, 1995; *Luth & Willingshofer,* 2008*)*;from 20 Ma onward Alps cooled down at 25°C/Myr (*Luth & Willingshofer,* 2008). Therefore, at the time recorded by our ZHe data, cooling rates should had a value included between 50 and 20°C/Myr, for which *Reiners & Brandon* (2006) reports a T_c of about 175-200°C.

For the Mesule-Moosboden area, from which episyenite samples come from, *Luth & Willingshofer* (2008) reports these ages (figure ****):

- Zircon Fission Track (T_c at 230°C): 16-17 Ma;
- Apatite Fission Track (T_c at 110°C): 8-10 Ma;

these ages defines cooling rates of about 13-20°C/Myr.

Even though these ages have been obtained by the interpolation of scattered data they are useful for our following interpretation. If we assume then a closure temperature for ZHe of about 190°C, applying a cooling rate of 25-30°C at the T_c of ZFT we reach 200-190°C in about 1-2 Myr: this means that the ages reported by ZHe should be of ca. 14-15 Ma, and not 10-11 Ma as we have obtained. In addition, AFT ages reported in their database overlaps ZHe ages in our region. Thermochronologic data in *Most* (2003) and *Bertrand* (2013) for a nearby region also shows discordant ages in respect to what we observe (figure ***).

Younger ages may be explained supposing the occurrence of a resetting event in our area. Given the low closure temperature of the He system, a hydrothermal event could have triggered diffusion of He after the effective regional cooling below the specific T_c. This theory include three possible scenarios (figure ***):

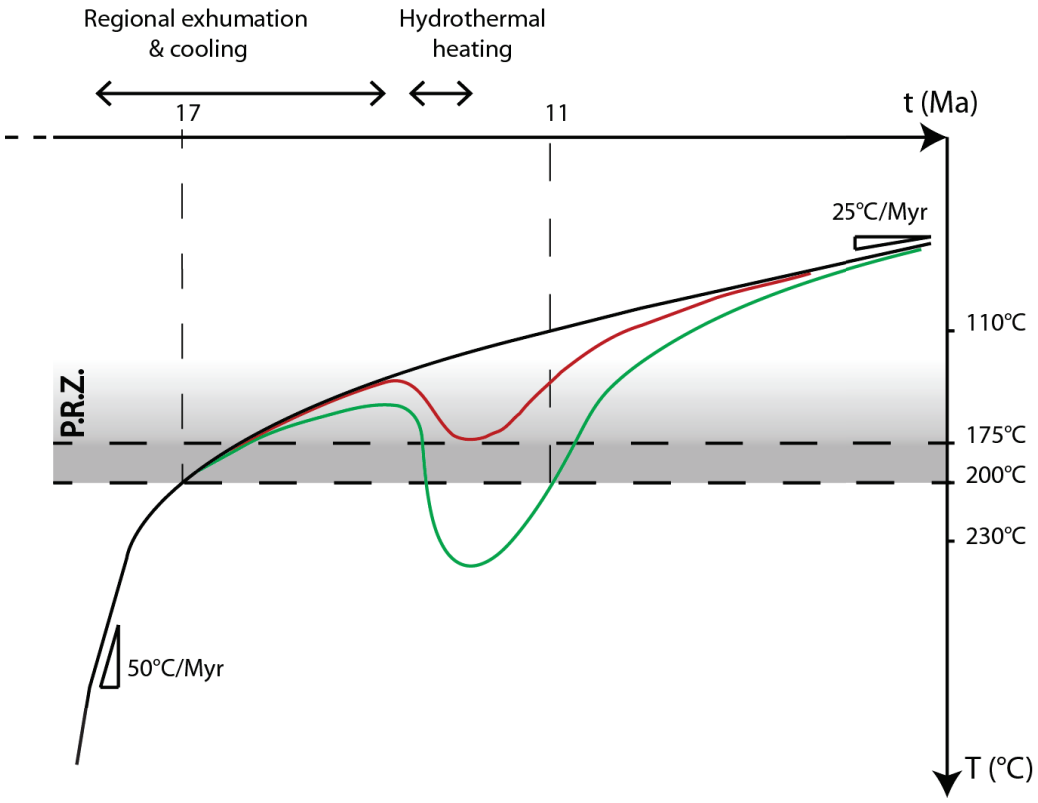

Figure 7: Possible cooling path for the analized zircons (see text for explanation).Black curve: regional path (1); Red curve: heating at T lower than the closure temperature (2); Green curve: heating at T above the T_c.

1. The sample cools down following the regional trend without any further heating or heating at a T lower than any PRZ or T_c;
2. The sample cools down at a certain age and then is heated up at a T lower than the T_c but sufficient to enter in the PRZ and trigger the diffusion of He and the partial annealing and younging, recording only partially the: in this case age data will be included between the first and the second cooling age; Ages should be correlated to eU and dimensions of the crystals;
3. The sample cools down and then is heated up at a T higher than the T_c: the system is completely resetted and ages have low dispersion, they all

address the second cooling age;

The theory of resetting by a “high” temperature (relative the system closure) event is then also supported by the low dispersion of our data (average age 11.4 ± 0.51 Ma). As we have already seen, these rock have undergone many and many different hydrothermal events; but only one occurred after the cooling of the host rock at T below 300°C: episyenitization. Even though they are not so reliable, chlorite geothermometers applied to episyenite gives temperatures included between 240°C and 350°C (to be considered T of the fluid in equilibrium with the product phase). Therefore, a hydrothermal reset of U-Th/He system after episyenitization seems not so strange.If it is so, ZHe data represent the cooling age after the hydrothermal heating, and then the minimum age at which episyenites has formed. In addition, the maximum age is represented by the regional cooling age (15-16 Ma) of ZFT.

In addition, given the post-slip overprint of episyenite on cataclasites, these data also define the minimum age of activity of our strike-slip faults. Some authors have found the lower limit of ductile activity of regional shear zone to be around 7 Ma (Greiner shear zone, *Schneider*, 2013).

Appendix A – XRF and EMPA compositions

		XRF	EMPA	Raman	SEM	XRPD-Rietveld	Micro-CT	Stable Isotope	Flinc	Zhe
Host Rock	Alpine-type	12.104A	x	x						
	Aplite	12.104E	x			x				
	Gdr	12.104F	x			x				
	Myl	12.105B	x			x				
	Lamp	13.345B	x							
Episyenite	Gdr	GDT-1	x	x						
	Gdr	12.104B	x	x						
	Gdr	12.104C-Epi	x	x		x				
	Aplite	12.104D	x	x		x				
	Gdr	12.104H	x		x			x		x
	+Cc	12.104I	x	x	x					x
	+Cc	12.104J	x		x	x				x
	Myl	12.105A	x							
	Lamp	13.345A	x							
Cataclasite		EP-1	x	x		x				
		EP-TOMO	x		x		x			
		12.104C-Cat	x			x				
		12.104G	x							
		CAT1	x			x				
		CAT388A	x							
		CAT388B	x							
		13_334							x	

	Host Rock				*Cataclasites*				
Type	***Aplite***	***Gdr***	***Myl***	***Lamp***					
Sample	***12.104E***	***12.104F***	***12.105B***	***13.345B***	***CAT1***	***CAT388A***	***CAT388B***	***12.104C-Cat***	***12.104G***
SiO_2	71,91	65,01	66,72	57,09	81,49	83,69	82,77	63,83	66,32
TiO_2	0,04	0,59	0,43	0,93	0,36	0,15	0,21	0,35	0,21
Al_2O_3	15,36	17,27	17,15	16,26	8,85	8,49	8,51	19,13	19,09
Fe_2O_3	0,43	4,97	4,61	7,32	2,79	1,09	1,64	3,33	2,13
MnO	0,01	0,08	0,04	0,13	0,04	0,01	0,02	0,03	0,02
MgO	0,10	0,95	0,82	5,80	0,65	0,25	0,39	0,33	0,25
CaO	0,75	4,45	2,59	5,49	0,96	0,61	0,61	1,79	0,73
Na_2O	3,32	4,53	5,58	1,27	2,86	2,60	2,60	10,23	10,34
K_2O	7,25	1,68	1,73	5,20	1,74	2,79	2,21	0,37	0,44
P_2O_5	0,12	0,14	0,10	0,18	0,10	0,04	0,05	0,09	0,06
Tot	99,29	99,67	99,77	99,67	99,84	99,72	99,01	99,48	99,59
L.O.I.	*0,27*	*0,52*	*0,43*	*3,64*	*0,87*	*0,43*	*0,64*	*1,67*	*0,85*
Sc	7	<5	<5	18	15	8	16	9	14
V	<5	39	21	176	35	10	21	21	16
Cr	<6	<6	<6	149	<6	31	7	<6	<6
Co	69	56	103	70	67	158	155	42	53
Ni	<3	<3	<3	20	<3	69	4	3	6
Cu	17	29	20	17	10	14	16	23	13
Zn	4	75	67	87	43	5	16	24	19
Ga	23	27	26	26	10	5	8	21	26
Rb	158	63	67	186	67	103	83	20	20
Sr	77	363	258	167	90	85	89	525	495
Y	14	18	10	20	21	5	6	10	8
Zr	42	376	223	114	193	99	134	213	126
Nb	8	10	15	7	24	3	26	5	5
Ba	388	841	910	1156	425	584	564	235	210
La	10	130	92	18	25	19	43	48	45
Ce	19	177	171	40	60	60	74	102	57
Nd	<10	37	15	<10	15	<10	15	47	35
Pb	57	17	18	18	9	31	38	10	11
Th	<3	19	16	6	9	6	7	14	8
U	17	7	4	8	<3	3	<3	5	6

				Episyenite								
Type				**Gdr (Chl)**	**Gdr**	**Gdr**	**Aplite**	**Gdr**	**Gdr +Cc**	**Gdr +Cc**	**Myl**	**Lamp**
Sample	**GDT-1**	**EP-1**	**EP-TOMO**	**12.104A**	**12.104B**	**12.104C-Epi**	**12.104D**	**12.104H**	**12.104I**	**12.104J**	**12.105A**	**13.345A**
SiO_2	63,14	62,83	64,55	56,05	54,24	59,51	65,18	56,27	55,58	60,84	63,01	58,92
TiO_2	0,66	0,29	0,27	0,65	0,58	0,56	0,06	0,61	0,49	0,67	0,56	0,94
Al_2O_3	17,21	19,16	18,75	22,51	19,95	20,00	19,55	21,05	18,74	19,83	20,32	16,77
Fe_2O_3	5,97	3,24	2,93	5,45	4,72	4,68	0,55	5,03	3,84	4,10	4,24	7,28
MnO	0,12	0,05	0,05	0,06	0,09	0,08	0,01	0,07	0,08	0,06	0,05	0,12
MgO	1,41	0,60	0,50	1,08	0,96	0,98	0,13	1,04	0,72	0,95	0,72	4,95
CaO	4,20	2,16	1,57	4,39	9,61	4,02	0,70	6,14	10,62	2,74	0,84	3,98
Na_2O	4,12	6,60	5,88	6,48	6,86	7,50	4,94	6,74	7,32	8,78	8,02	1,05
K_2O	2,18	4,19	4,66	2,32	2,05	1,74	8,64	2,29	1,95	1,07	1,72	5,59
P_2O_5	0,19	0,08	0,08	0,13	0,14	0,14	0,11	0,14	0,10	0,15	0,15	0,19
Tot	99,20	99,20	99,24	99,12	99,20	99,21	99,87	99,38	99,44	99,19	99,63	99,79
L.O.I.	*1,74*	1,68	0,89	*2,33*	*8,03*	*4,14*	*0,57*	*6,12*	*8,35*	*3,39*	*1,82*	*5,14*
Sc	11	11	10	<5	<5	17	9	<5	<5	7	13	25
V	56	13	15	39	30	34	<5	31	24	26	25	152
Cr	<6	<6	<6	<6	<6	<6	<6	8	<6	<6	7	128
Co	98	50	73	60	22	36	40	35	19	20	42	62
Ni	<3	<3	<3	<3	6	3	<3	41	49	4	84	20
Cu	24	17	15	36	25	21	21	23	26	18	15	15
Zn	84	53	51	77	77	75	13	79	61	72	59	102
Ga	22	16	16	30	26	24	23	28	25	22	24	28
Rb	85	81	91	93	88	78	203	104	76	48	70	190
Sr	315	450	386	635	1191	1025	174	1253	921	665	811	152
Y	36	14	14	19	15	19	13	16	10	17	14	24
Zr	360	198	185	394	406	384	58	372	262	424	342	125
Nb	16	11	19	10	10	10	10	8	8	14	12	9
Ba	744	1756	1882	955	946	1067	1022	1119	1150	502	1097	1382
La	52	61	66	135	111	89	11	126	86	149	109	21
Ce	119	105	106	232	179	156	30	202	156	225	173	43
Nd	11	<10	<10	39	21	17	<10	16	<10	63	<10	<10
Pb	20	28	36	25	15	17	59	18	23	6	15	9
Th	13	12	11	17	14	13	<3	13	13	24	16	10
U	<3	5	<3	9	6	6	8	8	6	8	8	<3

	Host rock						*Episyenite*									*Alpine-type halo*					
	Pl1	*S.d.*	*n*	***Kfs1***	*S.d.*	*n*	***Pl2***	*S.d.*	*n*	***Adularia***	*S.d.*	*n*	***Kfs/pseud bt***	*S.d.*	*n*	***Plg_Rim***	*S.d.*	*n*	***Plg_core***	*S.d.*	*n*
Na_2O	9.82	0.26	36.00	0.77	0.26	26.00	11.74	0.34	38.00	0.23	0.06	8.00	0.31	0.07	4.00	10.26	0.38	3.00	9.26	0.39	6.00
MgO	0.00	0.00		0.01	0.01		0.01	0.01		0.01	0.01		0.02	0.01		0.01	0.01		0.01	0.01	
Al_2O_3	22.05	0.50		18.43	0.15		19.76	0.09		18.27	0.11		18.41	0.05		22.21	0.20		23.46	0.50	
SiO_2	64.53	0.53		64.08	0.81		68.08	0.42		63.47	0.37		63.19	0.73		64.69	0.57		62.84	0.74	
K_2O	0.25	0.16		15.36	0.53		0.08	0.04		16.15	0.32		15.91	0.48		0.11	0.06		0.23	0.08	
CaO	2.96	0.48		0.01	0.01		0.19	0.06		0.00	0.00		0.01	0.01		3.02	0.31		4.47	0.49	
FeO	0.05	0.02		0.33	0.48		0.03	0.02		0.01	0.02		0.24	0.05		0.14	0.21		0.03	0.02	
Totale	99.63	0.57		98.69	0.60		99.85	0.49		98.14	0.63		97.84	1.17		100.30	0.51		100.26	0.43	
Si	2.853	0.026		2.987	0.019		2.980	0.008		2.990	0.003		2.980	0.005		2.843	0.012		2.776	0.026	
Ti	0.000	0.000		0.000	0.000		0.000	0.000		0.000	0.000		0.000	0.000		0.000	0.000		0.000	0.000	
Al	1.149	0.023		1.013	0.010		1.020	0.008		1.015	0.007		1.023	0.011		1.150	0.015		1.221	0.028	
Cr	0.000	0.000		0.000	0.001		0.000	0.000		0.000	0.000		0.000	0.000		0.000	0.000		0.000	0.000	
Fe^{2+}	0.002	0.001		0.013	0.019		0.001	0.001		0.000	0.001		0.009	0.002		0.005	0.008		0.001	0.001	
Fe^{3+}	0.000	0.000		0.000	0.000		0.000	0.000		0.000	0.000		0.000	0.000		0.000	0.000		0.000	0.000	
Mn	0.000	0.000		0.000	0.000		0.000	0.000		0.000	0.000		0.000	0.000		0.000	0.000		0.000	0.000	
Mg	0.000	0.000		0.001	0.001		0.001	0.000		0.000	0.000		0.001	0.001		0.001	0.001		0.001	0.001	
Ca	0.140	0.023		0.000	0.001		0.009	0.003		0.000	0.000		0.000	0.000		0.142	0.015		0.211	0.023	
Na	0.842	0.019		0.070	0.023		0.996	0.026		0.021	0.005		0.028	0.007		0.874	0.028		0.793	0.032	
K	0.014	0.009		0.913	0.037		0.004	0.002		0.971	0.016		0.957	0.020		0.006	0.003		0.013	0.004	
Ba	0.000	0.000		0.000	0.000		0.000	0.000		0.000	0.000		0.000	0.000		0.000	0.000		0.000	0.000	
Sr	0.000	0.000		0.000	0.000		0.000	0.000		0.000	0.000		0.000	0.000		0.000	0.000		0.000	0.000	
Pb	0.000	0.000		0.000	0.000		0.000	0.000		0.000	0.000		0.000	0.000		0.000	0.000		0.000	0.000	
Totale	5.001	0.018		4.998	0.024		5.010	0.018		4.998	0.010		5.001	0.009		5.022	0.010		5.017	0.013	
Sito Z	4.004	0.005		4.014	0.010		4.001	0.007		4.006	0.005		4.015	0.007		3.999	0.002		3.999	0.006	
Sito X	0.996	0.021		0.984	0.022		1.009	0.025		0.992	0.016		0.986	0.016		1.023	0.011		1.017	0.018	
Ab %	84.48	1.48		7.13	2.40		98.70	0.51		2.12	0.54		2.88	0.70		85.48	1.86		77.93	2.41	
An %	14.07	2.14		0.04	0.06		0.87	0.31		0.01	0.02		0.04	0.04		13.93	1.62		20.78	2.35	
Or %	1.45	0.97		92.83	2.43		0.44	0.23		97.87	0.54		97.08	0.69		0.59	0.32		1.29	0.45	

	Host rock		*Alpine-type halo*			*Episyenite*		*Host rock*		*Episyenite*		*Alpine-type halo*		*Episyenite*						
	Ms	*S.d. N = 8*	*Ms*	*S.d. N = 7*	*Ms2*	*S.d. N = 4*	*Ms*	*S.d. N = 2*	*Bt*	*S.d. N = 12*	*Bt*	*S.d. N = 3*	*A-1-Chl*	*S.d. N = 10*	*B-2-Chl*	*S.d. N = 8*	*D-Chl*	*S.d. N = 3*	*A-Chl (episy)*	*S.d. N = 2*	*Ia-Chl*	*S.d. N = 21*
Na_2O	0.16	0.04	0.23	0.07	0.05	0.04	0.16	0.02	0.06	0.03	0.04	0.04	0.01	0.02	0.01	0.01	0.01	0.02	0.04	0.05	0.02	0.02
MgO	1.69	0.15	1.22	0.16	1.25	0.12	1.72	0.07	5.27	0.15	4.20	0.45	8.39	0.24	10.55	1.22	14.26	3.61	6.79	3.24	10.19	0.68
Al_2O_3	27.95	0.39	32.20	0.74	30.88	0.83	27.40	0.12	16.31	0.33	18.03	0.65	21.15	0.15	18.86	1.22	18.11	0.66	18.75	3.46	18.29	1.04
SiO_2	47.43	0.31	45.30	0.71	47.34	0.52	47.42	0.65	34.66	0.39	35.57	1.87	23.90	0.18	25.00	0.77	26.58	1.18	26.21	3.45	24.95	0.57
K_2O	10.68	0.14	10.70	0.17	11.03	0.07	10.43	0.01	8.87	0.49	7.33	1.15	0.01	0.01	0.04	0.03	0.02	0.03	0.45	3.02	0.05	0.06
CaO	0.00	0.01	0.00	0.00	0.01	0.02	0.00	0.00	0.05	0.07	0.20	0.15	0.02	0.02	0.13	0.15	0.08	0.04	0.08	3.04	0.18	0.15
TiO_2	0.45	0.12	0.45	0.20	0.01	0.01	0.51	0.07	2.85	0.30	1.95	0.42	0.05	0.03	0.06	0.04	0.02	0.01	0.18	3.09	0.04	0.02
Cr_2O_3	0.03	0.02	0.01	0.02	0.02	0.02	0.00	0.00	0.01	0.01	0.01	0.02	0.02	0.02	0.01	0.01	0.00	0.01	0.00	3.01	0.02	0.02
Mno	0.05	0.04	0.02	0.02	0.01	0.02	0.06	0.01	0.47	0.07	0.37	0.07	0.30	0.04	0.46	0.10	0.43	0.11	0.51	3.01	0.40	0.08
FeO	5.17	0.11	4.07	0.70	3.50	0.53	5.57	0.06	26.23	0.49	23.93	3.34	34.76	0.48	32.01	1.43	28.23	3.56	35.58	0.80	31.90	1.21
ZnO	-		0.01	0.02	0.00	0.00	-		-		-		0.06	0.04	0.08	0.02	0.14	0.07	-		0.09	0.04
F	-		0.14	0.22	0.05	0.04	-		-		-		0.05	0.11	0.17	0.20	0.17	0.29	-		0.05	0.10
Cl	-		0.00	0.00	0.00	0.00	-		-		-		-		-		-		-		0.00	0.00
Totale	93.60	0.24	94.33	0.85	94.16	0.38	93.28	0.67	94.77	0.83	91.62	3.09	88.72	0.50	87.38	1.67	88.04	0.92	88.61	3.09	86.18	2.00
O=F,Cl	0.00	0.00	-0.06	0.09	-0.02	0.02	0.00	0.00	0.00	0.00	0.00	0.00	-0.02	0.05	-0.07	0.09	-0.07	0.12	0.00	0.00	-0.02	0.04
Totale	93.60	0.24	94.28	0.84	94.13	0.38	93.28	0.67	94.77	0.83	91.62	3.09	88.70	0.47	87.31	1.70	87.97	0.82	88.61	3.09	86.16	1.99
H2O calc.	4.33	0.01	4.36	0.05	4.39	0.02	4.31	0.04	3.77	0.03	3.75	0.07	2.72	0.02	2.69	0.06	2.78	0.07	2.71	3.01	2.67	0.06
Totale	97.93	0.25	98.64	0.87	98.52	0.40	97.59	0.71	98.54	0.86	95.37	3.14	91.42	0.48	90.00	1.76	90.75	0.87	91.32	3.08	88.82	2.05
Si	6.569	0.039	6.483	0.048	6.457	0.058	6.597	0.031	5.509	0.050	5.691	0.245	5.259	0.043	5.520	0.160	5.683	0.084	5.798	3.069	5.594	0.146
Ti	0.047	0.012	0.049	0.017	0.001	0.001	0.054	0.008	0.341	0.036	0.235	0.047	0.008	0.004	0.011	0.006	0.003	0.002	0.030	3.014	0.007	0.004
Al	4.563	0.059	5.227	0.102	4.964	0.123	4.493	0.021	3.055	0.054	3.402	0.157	5.483	0.029	4.906	0.288	4.571	0.306	4.888	3.095	4.829	0.202
Cr	0.003	0.003	0.002	0.002	0.002	0.002	0.000	0.000	0.002	0.002	0.001	0.002	0.003	0.004	0.001	0.002	0.000	0.001	0.001	3.001	0.003	0.003
Fe^{2+}	0.599	0.014	0.451	0.071	0.400	0.062	0.648	0.013	3.487	0.066	3.204	0.457	6.394	0.082	5.911	0.287	5.067	0.804	6.583	3.183	5.980	0.192
Mn	0.006	0.004	0.002	0.002	0.002	0.002	0.008	0.001	0.063	0.009	0.050	0.008	0.056	0.008	0.086	0.018	0.077	0.018	0.096	3.001	0.077	0.014
Mg	0.348	0.032	0.242	0.035	0.255	0.026	0.357	0.011	1.249	0.037	1.003	0.121	2.751	0.074	3.470	0.370	4.526	1.033	2.241	3.090	3.404	0.198
Ca	0.000	0.001	0.000	0.001	0.002	0.003	0.000	0.000	0.009	0.012	0.033	0.028	0.005	0.004	0.031	0.035	0.018	0.009	0.018	3.009	0.044	0.038
Na	0.043	0.011	0.069	0.016	0.013	0.010	0.043	0.007	0.018	0.009	0.014	0.011	0.005	0.008	0.006	0.006	0.005	0.009	0.017	3.022	0.008	0.010
K	1.887	0.026	1.868	0.031	1.919	0.019	1.851	0.014	1.798	0.094	1.494	0.208	0.003	0.004	0.011	0.007	0.006	0.008	0.127	3.005	0.014	0.018
Zn	0.000	0.000	0.002	0.003	0.000	0.000	0.000	0.000	0.000	0.000	0.000	0.000	0.010	0.006	0.013	0.003	0.022	0.010	0.000	3.000	0.014	0.007
F	0.000	0.000	0.014	0.018	0.006	0.005	0.000	0.000	0.000	0.000	0.000	0.000	0.008	0.019	0.029	0.035	0.028	0.048	0.000	3.000	0.010	0.017
Cl	0.000	0.000	0.000	0.000	0.000	0.000	0.000	0.000	0.000	0.000	0.000	0.000	0.000	0.000	0.000	0.000	0.000	0.000	0.000	3.000	0.000	0.000
Totale	14.066	0.021	14.109	0.042	14.020	0.033	14.050	0.023	15.529	0.069	15.127	0.308	19.986	0.038	19.995	0.085	20.006	0.038	19.799	3.088	19.984	0.073
O=F,Cl	0.000	0.000	-0.014	0.018	-0.006	0.005	0.000	0.000	0.000	0.000	0.000	0.000	-0.008	0.019	-0.029	0.035	-0.028	0.048	0.000	3.000	-0.010	0.017
Totale	14.066	0.021	14.095	0.047	14.014	0.037	14.050	0.023	15.529	0.069	15.127	0.308	19.978	0.034	19.966	0.110	19.978	0.029	19.799	3.088	19.974	0.075
Al IV	1.431	0.039	1.317	0.048	1.543	0.058	1.403	0.031	2.491	0.050	2.309	0.245	2.741	0.043	2.480	0.160	2.317	0.084	2.202	3.069	2.406	0.146
Al VI	3.132	0.024	3.411	0.079	3.421	0.072	3.090	0.010	0.564	0.045	1.092	0.349	2.742	0.062	2.426	0.161	2.254	0.235	2.686	3.164	2.423	0.109
Sito O	4.135	0.014	4.155	0.040	4.080	0.025	4.156	0.002	5.705	0.059	5.586	0.269	11.955	0.034	11.905	0.144	11.927	0.044	11.637	3.124	11.894	0.115
Sito A	1.931	0.030	1.938	0.023	1.935	0.014	1.893	0.021	1.825	0.082	1.541	0.184	0.013	0.010	0.048	0.039	0.029	0.025	0.162	3.036	0.066	0.055

	Episyenite		*Host rock*		*Alpine-type*		Episyenite				
		S.d.		*S.d.*					*S.d.*	**n**	
	Grt	N = 9	**Grt**	N = 4	**Titanite**	**Ilmenite**	**D-Hm-1**	**Ia – Hm**	N = 5		**A-Hm01**
SiO_2	40.14	1.98	40.75	8.49	30.19	0.00	0.06	0.03	0.03	5.00	1.81
TiO_2	0.07	0.04	0.03	0.02	35.86	52.45	5.14	2.57	1.58		1.77
Al_2O_3	19.12	0.87	19.45	1.86	3.17	0.00	0.01	0.04	0.05		1.47
Cr_2O_3	0.03	0.04	0.00	0.01	0.06	0.00	0.02	0.02	0.03		0.02
FeO	26.94	1.57	23.10	3.60	0.53	45.46	85.94	86.92	1.96		83.87
Mno	1.57	0.91	2.57	2.24	0.00	2.35	0.01	0.01	0.02		0.07
MgO	0.26	0.06	0.44	0.15	0.00	0.01	0.09	0.10	0.04		0.48
CaO	11.65	0.73	13.75	1.14	28.17	0.04	0.01	0.02	0.02		0.03
Na_2O	0.03	0.02	0.01	0.02	0.01	0.00	0.00	0.01	0.02		0.00
K_2O	0.00	0.01	0.02	0.02	0.02	0.00	0.00	0.01	0.01		0.02
Totale	99.81	0.43	100.13	3.30	98.01	100.31	91.27	89.72	0.63		89.54
Si	3.163	0.135	3.160	0.442	0.989	0.000	0.001	0.001	0.001		0.048
Ti	0.004	0.002	0.002	0.001	0.883	0.992	0.102	0.052	0.032		0.035
Al	1.790	0.091	1.800	0.254	0.122	0.000	0.000	0.001	0.001		0.046
Cr	0.002	0.002	0.000	0.000	0.001	0.000	0.000	0.000	0.001		0.000
Fe^{3+}	0.118	0.060	0.146	0.122	0.015	0.016	1.793	1.894	0.063		1.789
Fe^{2+}	1.672	0.080	1.371	0.248	0.000	0.940	0.099	0.047	0.030		0.060
Mn	0.105	0.062	0.175	0.162	0.000	0.050	0.000	0.000	0.000		0.002
Mg	0.031	0.007	0.052	0.018	0.000	0.001	0.004	0.004	0.002		0.019
Ca	0.990	0.064	1.158	0.156	0.988	0.001	0.000	0.000	0.000		0.001
Na	0.004	0.004	0.002	0.003	0.000	0.000	0.000	0.000	0.001		0.000
K	0.000	0.001	0.002	0.002	0.001	0.000	0.000	0.000	0.000		0.001
Totale	7.880	0.064	7.867	0.267	**3.000**	**2.000**	**2.000**	2.000	0.000		**2.000**

	Episyenite (from aplite)					*Episyenite*		*Host rock*	
		S.d.		*S.d.*			*S.d.*		*S.d.*
	Scolecite	N = 4	**Heulandite**	N = 9	% Oxides	**Epidote**	N = 6	**Epidote**	N = 8
Na_2O	0.16	0.13	0.06	0.03	SiO_2	38.21	0.42	37.57	0.33
MgO	0.01	0.01	0.02	0.02	TiO_2	0.10	0.06	0.19	0.16
Al_2O_3	25.19	0.46	14.41	1.53	Al_2O_3	27.58	0.93	24.56	1.57
SiO_2	46.76	1.33	54.52	0.86	Cr_2O_3	0.01	0.03	0.01	0.02
K_2O	0.02	0.02	1.56	0.18	FeO	7.23	1.30	10.31	1.70
CaO	13.54	0.20	5.99	0.18	Mno	0.06	0.08	0.25	0.12
TiO_2	0.01	0.01	0.00	0.00	MgO	0.02	0.02	0.01	0.01
Mno	0.01	0.01	0.00	0.01	CaO	23.79	0.39	23.17	0.45
FeO	0.03	0.03	0.02	0.02	Na_2O	0.01	0.02	0.01	0.01
Totale	85.725	1.582	76.591	1.809	K_2O	0.00	0.00	0.00	0.01
Si	3.060	0.025	13.822	0.265	Totale	97.02	0.46	96.09	0.64
Al	1.943	0.021	4.299	0.378	Si	5.967	0.021	5.990	0.034
Ti	0.001	0.001	0.000	0.000	Ti	0.012	0.006	0.023	0.020
Fe^{2+}	0.002	0.001	0.004	0.004	Al	5.075	0.138	4.612	0.245
Fe^{3+}	0.000	0.000	0.000	0.000	Cr	0.002	0.003	0.002	0.002
Mn	0.001	0.000	0.001	0.002	Fe^{3+}	0.939	0.167	1.351	0.216
Mg	0.001	0.001	0.007	0.007	Fe^{2+}	0.006	0.010	0.026	0.034
Ca	0.950	0.028	1.628	0.068	Mn	0.008	0.010	0.034	0.017
Na	0.020	0.016	0.028	0.012	Mg	0.005	0.004	0.002	0.003
K	0.002	0.002	0.504	0.055	Ca	3.982	0.042	3.957	0.035
Zn	0.000	0.000	0.000	0.000	Na	0.004	0.005	0.002	0.003
Cr	0.000	0.000	0.000	0.000	K	0.000	0.000	0.001	0.001
F	0.000	0.000	0.000	0.000	Totale	16.000	0.000	16.000	0.000
Totale	5.979	0.022	20.295	0.099	Fe_2O_3	7.980	1.365	11.246	1.672
Si+Al	5.003	0.015	18.122	0.118	FeO	0.046	0.073	0.194	0.249
R Si/(Si+Al)	0.612	0.004	0.763	0.019	Totale	97.816	0.404	97.212	0.524

	Episyenite	
		S.d.
% Oxides	**Cc**	N = 4
MgO	0.01	0.02
CaO	54.34	0.42
MnO	0.27	0.18
FeO	0.10	0.10
ZnO	0.00	0.00
SrO		
BaO		
PbO		
CO_2	42.89	0.32
Totale	97.61	0.74
Mg	0.000	0.000
Fe^{2+}	0.001	0.001
Mn	0.004	0.003
Ca	0.994	0.004
Zn	0.000	0.000
Ba	0.000	0.000
Sr	0.000	0.000
Pb	0.000	0.000
C	1.000	0.000
Totale	2.000	0.000

Appendix B. Analytical techniques

Spectroscopy

Spectroscopy is a general concept that indicates a set of techniques that analyse and measure an electromagnetic spectrum radiating from a source, in terms of emitted wavelenght or energy (frequency). If this spectrum results from the interaction between matter and an incident beam of electromagnetic radiation, different types of spectroscopy allow us to qualitatively and quantitatively describe the medium in terms of chemistry and molecular structure.

Any medium, compound or single element, is build up by charged particles held together by chemical bonds resulting from interactions of atomic orbitals. When these charged particles interact with the electromagnetic radiation, that by definition is a form of energy due to electromagnetic interactions, an energy transition occurs. This process involve either the alteration of the charged particle energy state toward a state of different energy, and the absorption, diffusion and dispersion of the incident beam. Transition back to the original energy state result in the emission of energy as electromagnetic radiation.

The internal energy of a particle has two main component, kinetic energy and atomic – electrostatic energy. Translation, rotation and vibration are three different types of motion of a particle; the sum of their relative kinetic energy give rise to the total kinetic part of internal energy. Binding energy between electrons and nucleus, and between different hadrons inside the nucleus arrange the atomic – electrostatic part.

Each of these componets is susceptible to a specific range of the electromagnetic spectrum, that is, only certain energies and waveleghts of the incident beam will make te particle change its equilibrium state in terms of that type of energy, making a transition to occur.

Spectroscopy of the emitted radiation allow us to characterize the energy transition and then to obtain qualitative and quantitative information about

chemistry, molecular and atomic structure.

Raman spectroscopy

Vibrational spectroscopy, to which Raman microspectroscopy belongs, use Visible and InfraRed light in order to punctually define the chemistry, structure and intermolecular interactions of a medium. The physical phenomenon at the base of these analysis is Light scattering due to light – matter interaction.

Among different types of scattering, Raman effect is an anelastic scattering that occurs with a very low frequency (1 out of 10^6). It involves energy gains or losses between incident and emitted photons, that coincide with the vibrational energy levels of the scattering particle. This effect is strictly linked to the polarizability of the molecule: the interaction photon – electronic cloud induce an electric dipole moment that behave as an oscillator. If the polarizability is constant, this oscillator, relaxing back to the equilibrium state, will emit the same frequency (i.e. energy) that exited it before. Otherwise, if the polarizability is influenced by the vibrational modes of the molecule, the emitted frequency will be different from the former one, and it can be correlated to the vibrational mode. Vibrations depends on dimension, atomic mass and valence of elements, binding forces and symmetry of the structure.

Two are the main events that we can observe with Raman spectroscopy: Stokes – Raman scattering, in which the emitted photon comes from the relaxation of an excited molecule back to an intermediate excited state (not to the former equilibrium state) and therefore it has lower frequency; Anti – Stokes scattering, during which there is the emission of a photon from the relaxation of a molecule to the original equilibrium state, with higher energy than the former one. The fundamental parameter is the Raman shift, the difference between the incident and emitted photons in terms of wave number (inverse of the wavelength, it represent the number on wave in a length unit). Raman spectra result from the plotting of the Raman shift against the Intensity of emitted light.

A Raman spectrometer is essentially composed by: a source of laser light (usually

green light at 532 nm or red light at 660 nm); a sample holder and a light detector. The spatial arrangement of these three elements have not to satisfy any geometrical requirements. Usually Raman facilities are installed on an optical microscope, allowing punctual measures. Raman spectroscopy is very effective in qualitatively identify mineral species and polymorphs, fluid or solid inclusions composition.

Scanning Electron Microscope

Scanning electron microscopy and microprobing are based on the interaction between a beam of accelerated high energy electrons and a small (usually some μm^3) volume of matter. This results in the emission of a set of particles such as Secondary, Back Scattered electrons or IR, VIS and X photons. This type of microscopy is useful to discover morphology, mean chemical composition of a sample's area or to qualitatively analyse the chemical composition of a single point.

The general architecture of an Electron Microscope is composed by a vertical cylindrical vacuum chamber at which opposite ends are placed the electron source and the sample. A difference in electric potential of 10^2 - 10^3 kV is set up between the cathode and anode of the electron source. The cathode is a filament of LaB_6 (or W, in older facilities) through which flows an electric current of 2,5 A: electrons are then emitted as a consequence of thermoionic effect. These electrons, being charged particles inside an electric field, are then accelerated by the difference of electric potential toward the anode. The latter has a central hole that defines the outcoming electronic beam. The electronic beam is corrected, adjusted and modified during is run throughout the vacuum chamber by several electromagnetic lenses. One of these lenses, the deflection coil, imprint to the beam the “scanning” movement from which this technique takes its name. The electron's run ends at sample surface. Despite the typology of sample – that it could be a thin section, a handspecimen, etc. etc. - it should be made conductive:

in order to do this it need to be “metallized” (i.e. covered by a thin film of C – graphite or Au particles).

Scanning Electron Microscopy usually uses Secondary and Backscattered electrons. Secondary electrons are low energy particles (<50 eV) that are dislocated from their original “seat” by the incident beam in the first few nm^3 of interaction. They are useful to obtain morphological images. Backscattered electrons are charged particles of the incident beam that are scattered backward after the interaction. Their energy depends on the total number of interaction, that in turn depends on the average atomic umber. Therefore, their study reveal the “bulk” chemical composition of a point.

The most energetic and powerful interaction between beam and matter causes orbital energy transition, that is, electrons gain energy and can jump from an orbital to another. The transition backward causes a more or less intense emission of X-ray characteristic of the involved chemical element (Characteristic spectrum). Thus, analysing the X-ray spectrum we can qualitatively know the chemical composition of the investigated volume. Usually SEM facilities are equipped with an Energy – Dispersive Spectrometer. These device is made of a scintillator, a crystal of Si or Ge, doped with Li, P, that translate the number of incident photons, electrons, with defined energy, proportionally to an electric signal. Collecting characteristic X-ray spectra we can define elements that are present inside a sample (starting from Be, $Z \geq 3$). EDS has high intensity of characteristic spectra but a low spectral resolution. Therefore quantitative analysis are impossible.

Electron MicroProbe and X-Ray Fluorescence

EMP is a quantitative spectroscopy technique useful for punctual composition analysis. Physical principles and facilities are essentially the same of SEM: an accelerated and focused beam of electrons runs into a vertical vacuum chamber and collides with the sample. The sample emits an x-ray characteristic spectrum function of the chemical composition. The main difference between these two

techniques lies in the way that this spectrum is analysed: EMP analysis uses WDS spectrometers. Wavelength Dispersion System spectrometers identify chemical elements by means of their characteristic x-ray wavelength that is defined through diffraction. The sample characteristic spectrum is collimated and conveyed toward an analyser crystal, of known composition, structure and spatial orientation, that optically disperse the characteristic spectrum according to the Bragg's law. Source of x-rays (sample), analyser crystal and detector must be disposed along what is called “Roland circle”, a special requirements for the occurrence of diffraction. According to the selected analyser crystal, a limited range of chemical elements can be identified, so that, EMP facilities are usually provided with more than one WDS spectrometer with different analyser crystal, allowing *simultaneous* measurements of different elements. WDS analysis have a high spectral resolution but low intensity.

The sample, as we already seen for SEM analysis, need to be covered with a thin film of conductive material such as graphite or Au.

X-Ray Fluorescence spectrometers are also called Bragg's spectrometers. The working principles are identical to that of EMPA – WDS spectrometry. There are three main differences between EMP and XRF techniques:

(i) The sample must be crushed and melted to form a vitreous material to overcome certain analytical errors;

(ii) The x-ray source is a Coolidge tube with a Rh anode; the applied electric potential difference is slightly less than that is needed for the emission of the characteristic spectrum of Rh, so that the emitted x-ray spectrum is the so called "bremsstrahlung" radiation, the continuous spectrum;

(iii) XRF analysis are bulk analysis;

The quantitative analysis for both XRF and EMP are based on the Castaign's Relation:

$$I_{std}/I_{smp} = C_{std}/C_{smp}$$

that permits to obtain the concentration of a certain element (C_{smp}) comparing the measured spectrum intensity (I_{smp}) with the known relation between standard concentration and measured intensity (C_{std}/I_{std}). Therefore, XRF and EMP analysis are defined as "*comparative*" analysis.

Correction to C_{smp} must be applied in order to avoid the contribution to the measured amount from analytical errors, sample inhomogeneities, textures, etc. XRF and EMP have different correction parameters and procedures:

(a) EMPA. Instrumental correction: (i) counter dead-time, time of inactivity between one count and another, if it is not regular, intensity will be falsified; (ii) background correction; (iii) instrumental drift accounts those events of natural wearing due to facilities usage; Sample correction "Z.A.F.": (iv) Z stands for atomic number, this correction factor considers the frequency of inelastic events that causes fluorescence relative to the atomic number Z and the energy of incident electron E_0; (v) Absorption correction accounts for absorption of incident electrons, of emitted x-ray during their path toward the sample surface and absorption due to the bulk composition (matrix effect); (vi) Fluorescence correction, the concentration of elements with low electronic potential (Critical EP - CEP) of activation could be overestimated by the induced fluorescence by the whole set of radiation with energies greater than CEP.

(b) XRF. Interelemental effects: absorption and reinforcement (induced fluorescence) are the main two "matrix effects" due to the bulk chemical composition of the sample, and they are corrected diluting the sample with low – atomic number elements or compounds (such as $Li_2B_4O_7$). Physical effects due to texture, grain size and inhomogeneities are corrected through milling and/or melting of the sample.

Isotope ratio mass spectrometry

Isotope Ratio Mass Spectrometry (IRMS) is a specialized technique used to

provide information about the provenance of geologic phases building rocks and mineral. The measurement of the ration between stable isotopes of C, N, O and H can lead to obtain important information on the genetic processes and fundamental materials that build up some phase. Isotope ratios are reported in the delta notation δ relative to selected universal standards:

$$\delta = 1000(R_{sample} / R_{standard})/R_{standard}$$

The value R_{sample} refers to the ratio between the heavier to the lighter isotope (e.g. $^{18}O/^{16}O$). Isotope mass spectrometer uses a magnetic field to separate and measure the amount of isotopes with different masses by bending ions of different charges at different radii.

Thermochronology. General concepts

Thermochronometry is a useful tool widely applied in regional, petroleum, sedimentary geology and basin analysis. Through thermocrhonological studies on specific mineral phases we can quantify the thermal evolution of a rock in respect to time. Most of the available thermochronometers are based on the radioactive decay of unstable elements, such as $^{238/235}U$, ^{232}Th and ^{40}K in certain mineral phases. Daughter elements, isotopes and by-products (such as ^{4}He and Fission Tracks) are produced at a rate defined by the parent decay constant. This means that their concentration will increase with time. As a consequence, diffusion will take place to redistribute chemical elements and punctual defects due to radioactive decay. Diffusion is a thermally-activated process, that is exponentially hindered by decreasing temperature. Therefore, there will be a specific temperature at which diffusion is completely unable to redistribute chemical elements and retention of decay products is complete. This temperature is called "closure temperature" of the system. Actually this happens over a limited range, called Partial Retention or Partial Annealing zone.

Apatites, zircons, micas and feldspars are the most frequent mineral phases on which thermochronometers are applied. Each phase has its own lattice structure with different bonding energies that strongly affect diffusion processes. Therefore

the resulting thermochronometer will be characterized by a specific closure temperature.

Partial Retention Zone (PRZ) is the effective range of temperature over which diffusion efficiency of the decay products decrease from 90% (at maximum T) to 10% (at minimum T). The *closure temperature* T_c, instead, is defined as the temperature of a rock at its thermochronometric age, assuming a monotonic cooling history. T_c is often preferred to PRZ in order to easily evaluate the effective thermal sensitivity of a thermochronometer.

Quantifying the parent/daughter elements ratio we can deduce the absolute time when that particular mineral phase started to behave as a closed system in respect to a certain radioactive system.

Thermochronology is often applied to regional geology studies in order to characterize the thermal evolution of a rock body. Burial and exhumation are the two main processes recorded by thermocrhronology. Here we have to specify the meaning of *uplift* and *exhumation* of a rock: (i) *uplift* refers to the movement of a part of the Earth's crust in respect to a given datum (such as sea level); (ii) *exhumation* refers to the vertical movement of a rock in respect to the Earth's surface. Erosion and tectonics are the principal causes of exhumation.

U-Th/He on Zircon

U-Th/He thermochronometry is based on α-decay of U and Th. U-He was discovered by Ernst Rutherford in the first decades of the 19th century, but its application and correct interpretation of resultig dates become a common practice only in the '80 of the twentieth century.

^{4}He nuclei are produced during the α-decay of ^{235}U, ^{238}U, ^{232}Th, and ^{147}Sm series. The general equation for He-ingrowth in time is:

$$^4He = 8 \cdot {}^{238}U(e^{\lambda 238t}-1) + 7 \cdot {}^{235}U(e^{\lambda 235t}-1) + {}^{232}Th(e^{\lambda 232t}-1) + {}^{147}Sm(e^{\lambda 147t}-1)$$

where

^{4}He, $^{238/235}U$, ^{232}Th, ^{147}Sm: present day amount of isotopes,

λ : decay constant;

λ^{238} = $1.551*10^{-10}$ yr^{-1};

λ^{235} = $9.849*10^{-10}$ yr^{-1};

λ^{232} = $4.948*10^{-11}$ yr^{-1};

λ^{147} = $0.654*10^{-11}$ yr^{-1};

Coefficients preceding U isotopes accounts for multiple α-ejection within each decay series. He-ingrowth equation assumes no initial content of ^{4}He or derived from an external source, secular equilibrium among daughters in the decay chain, assumption that are highly reliable for zircons.

- Analytical procedures

Samples are usually shattered down to fine sand granulometry and then analysed using a magnetic separator. Mineral separates are then observed under oprical microscope or stereoscopes in odred to select the suitable crystals for thermochronometric analysis.

Euhedral, inclusion free, intact and well preserved Zircons are preferentially selected for U-Th/He thermochronology. Selected crystals have to be measured and photographed under optical stereoscope. The next step is zircons packing: selected samples are packed together or one by one in one or more Nb tubes (a small cylinder 1mm in diameter that has been sealed at the ends using tweezers) and then they can be analysed.

He and parent elements are measured during two different moments of the analysis with two different methods: (a) Zircons is heated up and He emission are measured using a Gas-source Mass Spectrometer; (b) in a second moment, Zircons are dissolved chemically and then U, Th and Sm amounts are measured using Inductively Coupled Plasma Mass Spectrometry.

Raw age data obtained directly from the measured amount of ^{4}He must be

corrected. Helium could run for more than 20 μm from the point of decay, therefore parent nuclides placed along grain boundaries have high probability to eject α particles outside the crystal volume. This could bring to age underestimation. He-loss are related to Surface/Volume ratio and to the initial distribution of parent nuclides inside the crystal (homogeneous or zoned). Assuming a homogeneous distribution, an ideal geometry (calculated from the measured dimension of the crystal), geometrical correction factor (Ft) for each parent nuclide are then applied to raw dates.

Step-heating experiments oh He-diffusivity has demonstrated that PRZ and T_c are sensitive to the cooling rates and to the zircon grain size. For constant dimension, T_c and PRZ increases with increasing cooling rates. Smaller crystals have higher diffusivity (min. width is 60 μm).

- Description of parameters usually reported in U-Th/He dating important for resutl interpretation:

- Raw/Corrected dates: date that are obtained directly from ^{4}He measures need to be corrected in order to consider Helium loss along grain boundaries (α-ejection correction);

- Ft parameters: geometrical factors that account for the α-ejection outside crystal volume for each parent nuclide;

- Rs: ray of a sphere of equivalent volume of the zircon;

- eU: amount of radioactive nuclides expressed in terms of ^{238}U equivalents, each nuclides has specific correction factors on the decay time to be correlated with that of U. eU (morph) represent the equivalent concentration of radioactive nuclides computed from the geometric approximation. eU (Zr) stand for the equivalent concentration measured during the experiment.

- eU(morph)/eU(Zr): this ratio gives an evaluation of the geometrical approximation goodness;

- Th/U: usually date results and Th/U concentration ratio are independent, if not,

this means that there are some external source to the crystal of U and Th, falsifying the resulting date;

XRPD and Rietveld refinement

The interaction between electromagnetic waves and matter can occur in three different ways: there could be a total absorption of the incident ray, or it could be partially re-emitted as e.m. waves of different energy (Luminescence), or in the end it could be only deflected without any modification of its energy (Scattering). The complete conservation of mechanical energy occurs only in coherent scattering, where the incident ray collide elastically without any energy waste (Rayleigh effect). Each point, particles, atoms that builds up matter behaves as punctual scatter and, according to the Huygens' principle, acts as a source of spherical waves. Multiple spherical wave interfere each other causing Diffraction of the incident e.m. wave. Diffraction consists in the propagation of scattered waves along given directions defined by several laws that take into account the incident wavelength and the spacing between scattering particles. Propagation of diffracted e.m. wave occurs only in those direction along which scattered waves are in phase. This means that the difference in pathways between to interfering waves have to be an integer multiple of the wavelength. Therefore, distance between two scattering points and the wavelength have to be comparable in terms of order of magnitude. A crystal lattice, being an ordered disposition of atoms, behaves as a diffraction lattice for X-ray, because the interatomic distances are in the same order of magnitude (1 Å= 10^{-1} nm) than X-ray wavelength (10^{-2} to 10 nm).

There are many mathematical equations that describe diffraction from different point of view. The most used in crystallography are Bragg's and Laue's laws, which explains the physical phenomenon as the result of a series of wave reflection or refraction respectively.

Bragg's law are usually written in this form:

$$d_{hkl} \cdot \sin\theta = n \cdot \lambda$$

where d_{hkl} stand for the interatomic distance between the two “reflecting” atomic planes, θ is the angle between the direction of diffraction and the horizontal, and λ

is the wavelength.

Diffraction can be explained using the theoretical concept of reciprocal lattice and Ewald's sphere, for which I refer to other specialized works for further informations.

X-Ray Powder Diffraction is an analytical technique useful for qualitative (and quantitative in certain cases) studies on mineralogical composition of polyphase materials or structural investigations of “single” phase. Each mineral is characterized by specific interatomic distances between known crystallographic planes that are function of unit cell parameters (constant length *a, b, c* and relative angles *α, β, γ*). Exploiting Bragg's law, using powder diffraction we can identify the whole set of crystalline phases that builds up polyphase materials. Samples need to be fragmented down to small powder particles, named crystallites, of 1-10 μm. At this dimensions, each crystallite represent a single phase crystal lattice (a single reciprocal diffraction lattice). The disordered distribution of the crystallite of a single mineral species in the whole powdered sample guarantee that statistically all the crystallographic planes belonging to that particular phase are brought to diffraction in the same event.

Powdered sample is usually placed on a disk-like sample holder or in a capillary. Usually, diffractometers uses a Bragg-Brentano parafocal geometry in which diffraction occurs in reflection. This set up is also known as θ-2θ geometry. X-ray source and detector are placed along a constant goniometric circle, at which centre is located the sample holder. The latter rotates in respect to X-ray source at a fixed angular velocity of ω (angle θ over a time *t*), while the detector rotates by twice at twice this velocity. Rotating from 0° toward 180° (2θ) and more, the detector (a scintillator) collects all the diffraction events that occur. The resulting diagram that represent the number (intensity) of diffraction against angular distance is called diffractogram. Comparing the resulting diffractorgram with already available diffraction database we can identify the mineralogical assembly.

Rietveld refinement

Rietveld refinement is an optimization algorithm developed in 1966 by Hugo Rietveld specifically for powder diffraction data analysis and structural refinement. This refinement method is based on the minimization (usually least square minimization) of a function representing the difference between the observed and a calculated diffractograms, the latter one derived using available diffraction data. The calculated diffractogram can be modified by the operator adjusting various parameters, such as unit cell parameters, cations occupancy site or vibrational parameters. Rietveld refinement are usually employed for unit cell parameters definition, cation occupancy site analysis or quantitative mineralogical studies on polyphase material.

An ideal working flowchart for quantitative mineralogical analysis using Rietveld refinement of powder diffraction data is shown below:

1. A real diffractogram is collected analysing the sample over a wide range (more than 100°) of 2θ in order to clearly identify each phase.

2. According to the qualitative mineralogy of the sample, a theoretical diffractogram is obtained from a software, taking into account different variables: (i) analytical conditions; (ii) structural parameters of selected phases; (iii) compositional parameters such as bulk composition ans site occupancy of single phases; (iv) morphological parameters of the diffraction profile, peak asymmetry, or correction factors due to preferential orientation;

3. Through several cycle of refinement and parameter adjustment by the operator, the software try to minimize the function at each point of the diagram.

4. Then, the software define the weight percentage of each phase as a function of the scale factor, a parameter proportional to the integrated areas of phase diffraction peaks;

If a substantial amount of amorphous or unknown phase is present, quantitative analysis are still possible. In order to do so, a known quantity (in weight percent) of “standard” is added to the powdered sample in order to have a “scaling phase”

on which the refinement algorithm refers to. This method is also known as "Internal Standard analysis". Usually, after the identification of peaks belonging to unknown phases, the analytical procedure follows these steps:

1. "Standard" compounds are analysed separately in order to obtain the exact diffractogram; according to this result, a crystal structure is selected from the existing database; it will be used later in the total analysis;

2. "Standard" is added to the powdered sample and then analysed;

3. Unknown peaks are usually excluded from the Rietveld refienment of the resulting diffractogram; the refinement is performed using the previously selected structure for the standard compound;

4. When a first result is obtained, comparing measured and effectively added quantity of standard, data analysis software recalculate the obtained quantification using simple proportions.

This process have usually an error of ±1 wt% in optimal conditions.

X-ray tomography

Micro-Computed Tomography (μ-CT) is a non-invasive imaging technique useful for 3D microstructural and morphological studies. As medical computed tomography do, μ-CT create 2D section of the investigated sample that can be used then to create a 3D model of the sample and its interiors. This analytical technique is based on the Absorption of high resolution X-rays. This wave-matter interaction is described mathematically by the Beer's law, which defines the general exponential proportionality between transmittance (T) and absorbance (A) of a body:

$$T = e^{-A}; \quad T = I/I_0 \quad A = \mu \cdot x$$

$$I = I_0 \cdot e^{-\mu x}$$

where I represent the final (I) and initial (I_0) intensity of the e.m. wave; μ represent the linear absorption coefficient of the body and x is the length of the

crossed section;

X-ray source, sample and detector in a microtomographer are usually linearly arranged. The X-ray source is a Coolidge tube, with a W filament, that differs from those employed in diffractometry for higher resolution, higher divergence and a polychromatic spectrum. This source requires also smaller working power and (10 W, 40-100 kV, 10-10^2 μA).**** The sample, placed on a rotating base between source and detector, does not need any specific preparation: if it is possible it should of cylindrical shape: this will solve some geometrical problems due to x-ray scattering (edge effect). The sample rotates gradually and an image is taken at each angular step for a variable time of exposure (that depends on the X-ray emitted intensity).This images are maps of the absorption coefficient, from which we can get back to the density of the body.

Each part of different absorption coefficient will be represented in 2D images with a specific tonality of grey. Then I can subdivide each phase analysing the hystogram of grey scale, choosing appropriate tone thresholds for distinguish one phase from another.

Fluid Inclusion microthermometry

Fluid inclusion microthermometry is a widespread techniques useful to obtain important information on the fluid composition and physical condition at which minerals formed and fluids have been entrapped. The main aim of microthermometry is to identify the phase transition that occur inside a fluid inclusion heating or cooling the sample. Usually this is obtained putting a double polished thick section on a heating-freezing stage and looking at phase transition by means of an optical microscope. The commonly observed relevant phase transitions are: (i) melting of a solid phase and (ii) homogenization of gaseous and liquid phases. Microthermometric data are the temperatures at which these transitions occurs. In general, melting is a gradual process that take place over a range of temperatures: the initial temperature (“eutectic temperature”) is linked to

the type of solute (usually some kind of salt) dissolved in the fluid inclusion; the final temperature define the amount, i.e. the salinity of the solution. The homogeneization temperature yield informations on the physical conditions of the fluid and of the environment of entrapment. Fluid inclusions are isochoric environments, therefore their evolution, e.g. in heating, on a phase diagram with a composition representative of that of the inclusion, will follow firstly the equilibrium curve between the coexisting phases, and then, reached the homogeneization temerature, it will depart from this curve following the "isochore". This curve represent all the possible physical conditions that a constant-volume fluid inclusion could have been undergone. Its slope depends on the density of the entrapped fluid. Along this curve it is located the effective temperature of entrapment, but constraints on pressure are necessary to exactly define the entrapment conditions.

Bibliography

- Andreucci, B. (2013). Thermochronology of the Polish and Ukrainian Carpathians. PhD thesis. University of Padova.
- Axen, G. J., Bartley, J. M., & Selverstone, J. (1995). Structural expression of a rolling hinge in the footwall of the Brenner Line normal fault, eastern Alps. Tectonics, 14(6), 1380-1392.
- Barker, A. J. (1995). Post-entrapment modification of fluid inclusions due to overpressure: evidence from natural samples. Journal of Metamorphic Geology, 13(6), 737-750.
- Barnes, J. D., Selverstone, J., & Sharp, Z. D. (2004). Interactions between serpentinite devolatilization, metasomatism and strike-slip strain localization during deep-crustal shearing in the Eastern Alps. Journal of Metamorphic Geology, 22(4), 283-300.
- Bell, T. H., Duncan, A. C., & Simmons, J. V. (1989). Deformation partitioning, shear zone development and the role of undeformable objects. Tectonophysics, 158(1), 163-171.
- Bertrand, A. (2014). Exhuming the core of collisional orogens, the Tauern Window,(Eastern-Alps): A geochronological, modelling and structural study (Doctoral dissertation, Berlin, Freie Universität Berlin, Diss., 2013).
- Bertrand, A., Garcia, S., & Rosenberg, C. (2010, May). Brittle deformation and exhumation mechanisms in the core of the Eastern Alps, The Tauern Window. In EGU General Assembly Conference Abstracts (Vol. 12, p. 9563).
- Blanckenburg, F. V., Villa, I. M., Baur, H., Morteani, G., & Steiger, R. H. (1989). Time calibration of a PT-path from the Western Tauern Window, Eastern Alps: the problem of closure temperatures. Contributions to Mineralogy and Petrology, 101(1), 1-11.
- Bodnar RJ (2003) Reequilibration of fluid inclusions. In I. Samson, A. Anderson, & D. Marshall, eds. Fluid Inclusions: Analysis and Interpretation. Mineral. Assoc. Canada, Short Course 32, 213-230.
- Bodnar, R. J., Vityk, M.O. (1994). Interpretation of microthermometric data for H_2O-NaCl fluid inclusions. *In* Fluid inclusions in Minerals, Methods and Applications, B. De Vivo and M.L. Frezzotti, eds., pub. By Virginia Tech, Blacksburg, VA, p. 117-130.
- Borges, R. M. K., Villas, R. N. N., Fuzikawa, K., Dall'Agnol, R., & Pimenta, M. A. (2009). Phase separation, fluid mixing, and origin of the greisens and potassic episyenite associated with the Água Boa pluton, Pitinga tin province, Amazonian Craton, Brazil. Journal of South American Earth Sciences, 27(2), 161-183.
- Cathelineau, M. (1986). The hydrothermal alkali metasomatism effects on granitic rocks: quartz dissolution and related subsolidus changes. Journal of Petrology, 27(4), 945-965.
- Cathelineau, M., & Nieva, D. (1985). A chlorite solid solution

geothermometer the Los Azufres (Mexico) geothermal system. Contributions to Mineralogy and Petrology, 91(3), 235-244.
- Ceccato, A. (2012). Evoluzione pre-alpina ed alpina dei granitoidi della conca del Moosboden-Finestra dei Tauri-Alpi Aurine. Unpubl. Bachelor thesis. University of Padova.
- Cesare, B., Poletti, E., Boiron, M. C., & Cathelineau, M. (2001). Alpine metamorphism and veining in the Zentralgneis Complex of the SW Tauern Window: a model of fluid–rock interactions based on fluid inclusions. Tectonophysics, 336(1), 121-136.
- Cesare, B., Rubatto, D., Hermann, J., & Barzi, L. (2002). Evidence for Late Carboniferous subduction-type magmatism in mafic-ultramafic cumulates of the SW Tauern window (Eastern Alps). Contributions to Mineralogy and Petrology, 142(4), 449-464.
- Costi, H. T., Dall'Agnol, R., Borges, R. M. K., Minuzzi, O. R. R., & Teixeira, J. T. (2002). Tin-bearing sodic episyenites associated with the Proterozoic, A-type Agua Boa granite, Pitinga mine, Amazonian craton, Brazil. Gondwana Research, 5(2), 435-451.
- Dal Piaz, G. V., Bistacchi, A., & Massironi, M. (2003). Geological outline of the Alps. Episodes, 26(3), 175-180.
- de Vecchi, G., & Baggio, P. (1982). The Pennine zone of the Vizze region in the western Tauern window (Italian eastern Alps). Bollettino della Societa Geologica Italiana, 101(1), 89-116.
- Dewey, J. F., Holdsworth, R. E., & Strachan, R. A. (1998). Transpression and transtension zones. Geological Society, London, Special Publications, 135(1), 1-14.
- Eggleton, R. A., & Banfield, J. F. (1985). The alteration of granitic biotite to chlorite. American Mineralogist, 70(9-10), 902-910.
- Eichhorn, R., Loth, G., Höll, R., Finger, F., Schermaier, A., & Kennedy, A. (2000). Multistage Variscan magmatism in the central Tauern Window (Austria) unveiled by U/Pb SHRIMP zircon data. Contributions to Mineralogy and Petrology, 139(4), 418-435.
- Engvik, A. K., Putnis, A., Gerald, J. D. F., & Austrheim, H. (2008). Albitization of granitic rocks: the mechanism of replacement of oligoclase by albite. The Canadian Mineralogist, 46(6), 1401-1415.
- F©ügenschuh, B., Seward, D., & Mancktelow, N. (1997). Exhumation in a convergent orogen: the western Tauern window. Terra Nova, 9(5-6), 213-217.
- Fitch, T. J. (1972). Plate convergence, transcurrent faults, and internal deformation adjacent to southeast Asia and the western Pacific. Journal of Geophysical Research, 77(23), 4432-4460.
- Fossen, H., & Tikoff, B. (1998). Extended models of transpression and transtension, and application to tectonic settings. Geological Society, London, Special Publications, 135(1), 15-33.
- Fossen, H., Tikoff, B., & Teyssier, C. (1994). Strain modeling of transpressional and transtensional deformation. Norsk Geologisk

Tidsskrift, 74(3), 134-145.
- Glodny, J., Ring, U., & Kühn, A. (2008). Coeval high-pressure metamorphism, thrusting, strike-slip, and extensional shearing in the Tauern Window, Eastern Alps. Tectonics, 27(4).
- González-Casado, J. M., Caballero, J. M., Casquet, C., Galindo, C., & Tornos, F. (1996). Palaeostress and geotectonic interpretation of the Alpine Cycle onset in the Sierra del Guadarrama (eastern Iberian Central System), based on evidence from episyenites. Tectonophysics, 262(1), 213-229.
- Grant, J. A. (1986). The isocon diagram; a simple solution to Gresens' equation for metasomatic alteration. Economic Geology, 81(8), 1976-1982.
- Grant, J. A. (2005). Isocon analysis: a brief review of the method and applications. Physics and Chemistry of the Earth, Parts A/B/C, 30(17), 997-1004.
- Herrmann, W., & Berry, R. F. (2002). MINSQ–a least squares spreadsheet method for calculating mineral proportions from whole rock major element analyses. Geochemistry: Exploration, Environment, Analysis, 2(4), 361-368.
- Kennett, B. L. N., & Bunge, H. P. (2008). Geophysical continua. Cambridge University, Kap, 10-11.
- Kuhlemann, J., Frisch, W., Dunkl, I., & Szekely, B. (2001). Quantifying tectonic versus erosive denudation by the sediment budget: The Miocene core complexes of the Alps. Tectonophysics, 330(1), 1-23.
- Kurz, W., Neubauer, F., Genser, J., & Dachs, E. (1998). Alpine geodynamic evolution of passive and active continental margin sequences in the Tauern Window (eastern Alps, Austria, Italy): a review. Geologische rundschau, 87(2), 225-242.
- Lacroix, B., Vennemann, T. (2013). Empirical calibration of the oxygen isotope fractionation between chlorite and quartz. EGU General Assembly 2013, Vienna.
- Lammerer, B., & Weger, M. (1998). Footwall uplift in an orogenic wedge: the Tauern Window in the Eastern Alps of Europe. Tectonophysics, 285(3), 213-230.
- Leroy, J. (1984). Episyénitisation dans le gisement d'uranium du Bernardan (Marche): Comparaison avec des gisements similaires du Nord-Ouest du Massif Central français. Mineralium Deposita, 19(1), 26-35.
- Lister, G. S., & Williams, P. F. (1983). The partitioning of deformation in flowing rock masses. Tectonophysics, 92(1), 1-33.
- López-Moro, F. J., Moro, M. C., Timón, S. M., Cembranos, M. L., & Cózar, J. (2013). Constraints regarding gold deposition in episyenites: the Permian episyenites associated with the Villalcampo Shear Zone, central western Spain. International Journal of Earth Sciences, 102(3), 721-744.
- Luth, S. W., & Willingshofer, E. (2009). Mapping of the post-collisional cooling history of the Eastern Alps. In Orogenic Processes in the Alpine Collision Zone (pp. S207-S223). Birkhäuser Basel.

- Mancktelow, N. S. (2002). Finite-element modelling of shear zone development in viscoelastic materials and its implications for localisation of partial melting. Journal of Structural Geology, 24(6), 1045-1053.
- Mancktelow, N. S., & Pennacchioni, G. (2005). The control of precursor brittle fracture and fluid–rock interaction on the development of single and paired ductile shear zones. Journal of Structural Geology, 27(4), 645-661.
- Mancktelow, N. S., & Pennacchioni, G. (2013). Late magmatic healed fractures in granitoids and their influence on subsequent solid-state deformation. Journal of Structural Geology, 57, 81-96.
- Mancktelow, N. S., Stöckli, D. F., Grollimund, B., Müller, W., Fügenschuh, B., Viola, G., ... & Villa, I. M. (2001). The DAV and Periadriatic fault systems in the Eastern Alps south of the Tauern window. International Journal of Earth Sciences, 90(3), 593-622.
- May, E., & Vennemann, T. (2013, April). Investigations on alpine-type albite-quartz veins of the Western Swiss Alps. In EGU General Assembly Conference Abstracts (Vol. 15, p. 10930).
- McCaffrey, R. (1996). Slip partitioning at convergent plate boundaries of SE Asia. Geological Society, London, Special Publications, 106(1), 3-18.
- Melcher, F., Prochaska, W., Raith, J. G., & Saini-Eidukat, B. (1996). The metamorphosed molybdenum vein-type deposit of the Alpeinerscharte, Tyrol (Austria) and its relation to Variscan granitoids. Mineralium Deposita, 31(4), 277-289.
- Most, P., Dunkl, I., & Frisch, W. (2003, February). Fission track tomography of the Tauern Window along the TRANSALP profile. In TRANSALP Congress (Trieste, 10-12 feb. 2003), Mem. Sci. Geol. Univ. Padova (Vol. 54, pp. 225-226).
- Neubauer, F., Genser, J., Kurz, W., & Wang, X. (1999). Exhumation of the Tauern window, Eastern Alps. Physics and Chemistry of the Earth, Part A: Solid Earth and Geodesy, 24(8), 675-680.
- Neubauer, F., Genser, J. , & Handler, R. (2000). The Eastern Alps: result of a two-stage collision process. Mitt Österr Geol Ges, 92, 117-134.
- Nishimoto, S., Yoshida, H., Asahara, Y., Tsuruta, T., Ishibashi, M., & Katsuta, N. (2014). Episyenite formation in the Toki granite, central Japan. Contributions to Mineralogy and Petrology, 167(1), 1-12.
- Northrup, C. J., & Burchfiel, B. C. (1996). Orogen-parallel transport and vertical partitioning of strain during oblique collision, Efjorden, north Norway. Journal of Structural Geology, 18(10), 1231-1244.
- Passchier, C. W., & Trouw, R. A. (2005). Microtectonics (Vol. 1). Springer.
- Pennacchioni, G. (2005). Control of the geometry of precursor brittle structures on the type of ductile shear zone in the Adamello tonalites, Southern Alps (Italy). Journal of Structural Geology, 27(4), 627-644.
- Pennacchioni, G., & Mancktelow, N. S. (2007). Nucleation and initial growth of a shear zone network within compositionally and structurally heterogeneous granitoids under amphibolite facies conditions. Journal of Structural Geology, 29(11), 1757-1780.

- Pennacchioni, G., & Mancktelow, N. S. (2013). Initiation and growth of strike-slip faults within intact metagranitoid (Neves area, eastern Alps, Italy). Geological Society of America Bulletin, 125(9-10), 1468-1483.
- Pennacchioni, G., & Zucchi, E. (2013). High temperature fracturing and ductile deformation during cooling of a pluton: The Lake Edison granodiorite (Sierra Nevada batholith, California). Journal of Structural Geology, 50, 54-81.
- Petersson, J., Fallick, A. E., Broman, C., & Eliasson, T. (2014). Imprints of multiple fluid regimes on episyenites in the Bohus granite, Sweden. Lithos, 196, 99-114.
- Petersson, J., Stephens, M. B., Mattsson, H., & Möller, C. (2012). Albitization and quartz dissolution in Paleoproterozoic metagranite, central Sweden—Implications for the disposal of spent nuclear fuel in a deep geological repository. Lithos, 148, 10-26.
- Petra, V., Frank, S., Friedrich, F., & Axel, G. (2011). Magmato-sedimentary Carboniferous to Jurassic evolution of the western Tauern window, Eastern Alps (constraints from U-Pb zircon dating and geochemistry). International Journal of Earth Sciences, 100(5), 993-1027.
- Jones, R., & Tanner, P. W. (1995). Strain partitioning in transpression zones. Journal of Structural Geology, 17(6), 793-802.
- Ramsay, J. G. (1980). Shear zone geometry: a review. Journal of Structural Geology, 2(1), 83-99.
- Recio, C., Fallick, A. E., Ugidos, J. M., & Stephens, W. E. (1997). Characterization of multiple fluid-granite interaction processes in the episyenites of Avila-Béjar, Central Iberian Massif, Spain. Chemical geology, 143(3), 127-144.
- Reiners, P. W. (2005). Zircon (U-Th)/He thermochronometry. Reviews in Mineralogy and Geochemistry, 58(1), 151-179.
- Reiners, P. W., & Brandon, M. T. (2006). Using thermochronology to understand orogenic erosion. Annu. Rev. Earth Planet. Sci., 34, 419-466.
- Rosenberg, C. L. (2004). Shear zones and magma ascent: a model based on a review of the Tertiary magmatism in the Alps. Tectonics, 23(3).
- Rosenberg, C. L., & Garcia, S. (2011). Estimating displacement along the Brenner Fault and orogen-parallel extension in the Eastern Alps. International journal of earth sciences, 100(5), 1129-1145.
- Rosenberg, C. L., & Schneider, S. (2008). The western termination of the SEMP Fault (eastern Alps) and its bearing on the exhumation of the Tauern Window. Geological Society, London, Special Publications, 298(1), 197-218.
- Rosenberg, C. L., Brun, J. P., & Gapais, D. (2004). Indentation model of the Eastern Alps and the origin of the Tauern Window. Geology, 32(11), 997-1000.
- Rossi, M., Rolland, Y., Vidal, O., & Cox, S. F. (2005). Geochemical variations and element transfer during shear-zone development and related episyenites at middle crust depths: insights from the Mont Blanc granite

(French-Italian Alps). SPECIAL PUBLICATION-GEOLOGICAL SOCIETY OF LONDON, 245, 373.
- Sanderson, D. J., & Marchini, W. R. D. (1984). Transpression. Journal of Structural Geology, 6(5), 449-458.
- Schmid, S. M., Scharf, A., Handy, M. R., & Rosenberg, C. L. (2013). The Tauern Window (Eastern Alps, Austria): a new tectonic map, with cross-sections and a tectonometamorphic synthesis. Swiss Journal of Geosciences, 106(1), 1-32.
- Schneider, S., Hammerschmidt, K., & Rosenberg, C. L. (2013). Dating the longevity of ductile shear zones: Insight from< sup> 40</sup> Ar/< sup> 39</sup> Ar in situ analyses. Earth and Planetary Science Letters, 369, 43-58.
- Selverstone, J. (1985). Petrologic constraints on imbrication, metamorphism, and uplift in the SW Tauern Window, Eastern Alps. Tectonics, 4(7), 687-704.
- Selverstone, J. (1988). Evidence for east-west crustal extension in the Eastern Alps: Implications for the unroofing history of the Tauern window. Tectonics, 7(1), 87-105.
- Selverstone, J., Axen, G. J., & Bartley, J. M. (1995). Fluid inclusion constraints on the kinematics of footwall uplift beneath the Brenner Line normal fault, eastern Alps. Tectonics, 14(2), 264-278.
- Sibson, R. H. (1994). Crustal stress, faulting and fluid flow. Geological Society, London, Special Publications, 78(1), 69-84.
- Simmons, S. F., & Christenson, B. W. (1994). Origins of calcite in a boiling geothermal system. American Journal of Science, 294(3), 361-400.
- Solar, G. S., & Brown, M. (2001). Deformation partitioning during transpression in response to Early Devonian oblique convergence, northern Appalachian orogen, USA. Journal of Structural Geology, 23(6), 1043-1065.
- Steenken, A., Siegesmund, S., Heinrichs, T., & Fügenschuh, B. (2002). Cooling and exhumation of the Rieserferner Pluton (Eastern Alps, Italy/Austria). International Journal of Earth Sciences, 91(5), 799-817.
- Steffen, K., Selverstone, J., & Brearley, A. (2001). Episodic weakening and strengthening during synmetamorphic deformation in a deep crustal shear zone in the Alps. Geological Society, London, Special Publications, 186, 141-156.
- Sterner, S. M., & Bodnar, R. J. (1989). Synthetic fluid inclusions-VII. Re-equilibration of fluid inclusions in quartz during laboratory-simulated metamorphic burial and uplift. Journal of Metamorphic Geology, 7(2), 243-260.
- Teyssier, C., & Tikoff, B. (1998). Strike-slip partitioned transpression of the San Andreas fault system: a lithospheric-scale approach. Geological Society, London, Special Publications, 135(1), 143-158.
- Tikoff, B., & Fossen, H. (1999). Three-dimensional reference deformations and strain facies. Journal of Structural Geology, 21(11),

1497-1512.
- Tischendorf, G., Rieder, M., Förster, H. J., Gottesmann, B., & Guidotti, C. V. (2004). A new graphical presentation and subdivision of potassium micas. Mineralogical Magazine, 68(4), 649-667.
- Twiss, R. J., & Moores, E. M.; Structural Geology, 2007, 2nd edition.
- Vityk, M. O., & Bodnar, R. J. (1995). Textural evolution of synthetic fluid inclusions in quartz during reequilibration, with applications to tectonic reconstruction. Contributions to Mineralogy and Petrology, 121(3), 309-323.
- Wagner, T., & Cook, N. J. (2000). Late-orogenic alpine-type (apatite)-quartz fissure vein mineralization in the Rheinisches Schiefergebirge, NW Germany: mineralogy, formation conditions and lateral-secretionary origin. Mineralogical Magazine, 64(3), 539-560.
- Wilkinson, J. J. (2001). Fluid inclusions in hydrothermal ore deposits. Lithos, 55(1), 229-272.